The ATLAS muon spectrometer: commissioning and tracking

Jochem Snuverink

The ATLAS muon spectrometer: commissioning and tracking

Jochem Snuverink

THE ATLAS MUON SPECTROMETER: COMMISSIONING AND TRACKING

This work is part of the research programme of the 'Stichting voor Fundamenteel Onderzoek der Materie' (FOM), which is financially supported by the 'Nederlandse Organisatie voor Wetenschappelijk Onderzoek' (NWO).

The author was financially supported by the University of Twente and by the 'Nationaal instituut voor subatomaire fysica' (Nikhef).

ISBN-13: 978-90-365-2912-9
DOI: 10.3990/1.9789036529129

Cover Design: Anneke de Vos

THE ATLAS MUON SPECTROMETER: COMMISSIONING AND TRACKING

PROEFSCHRIFT

ter verkrijging van de graad van doctor
aan de Universiteit Twente
op gezag van de Rector Magnificus
prof. dr. H. Brinksma
volgens besluit van het College voor Promoties
in het openbaar te verdedigen
op vrijdag 16 oktober 2009 om 15.00 uur

door

Jochem Snuverink

geboren op 20 september 1979
te Enschede

This thesis has been approved by:

Promotores: prof. dr. ing. B. van Eijk
prof. dr. F.L. Linde
Co-promotor: dr. drs. ir. P.M. Kluit

Contents

Chapter 1

Introduction

1.1 Physics motivation

The Standard Model is a well established theory for elementary particle physics that describes all known elementary particles and their interactions. Except for gravity all known forces are included: the electromagnetic, weak and strong nuclear force. The Standard Model has been very successful and experimental data and theory are in agreement. The theory has 18 free parameters[1], which are all but one measured by experiments. The missing parameter is the mass of the, so-called, Higgs particle. This particle, predicted by the Standard Model, has not yet been observed experimentally. Discovering this particle would validate the theory and in particular the mass generation mechanism.

Detecting the Higgs particle is difficult, because it is predicted to have a relatively large mass and little interaction with other particles. Theoretical considerations constrain its mass to be below 640 GeV [1], while direct searches at the Large Electron-Positron Collider (LEP) experiments have set a 95% confidence-level lower bound on its mass of 114.4 GeV [2]. Indirect experimental bounds on the Higgs mass can be obtained from a global fit to precision electroweak data, which is shown in figure 1.1. The grey area reflects the excluded region by direct searches and the associated band represents the estimate of the theoretical uncertainty. The fit gives a prediction of $m_H < 154$ GeV at a 95% confidence level [3]. Combining the direct and indirect measurements increases the upper limit to 185 GeV.

For a given Higgs mass, the Standard Model model predicts the branching ratio of its decay channels. The most relevant decay channels are presented in figure 1.2. For masses below 135 GeV, the Higgs particle decays for about 85% to $b\bar{b}$, with smaller decays rates to $\tau^+\tau^-$, $c\bar{c}$, gluon pairs and $\gamma\gamma$. For masses above 130 GeV, the W^+W^- decay dominates with an important contribution from decays into two Z^0-bosons.

To produce and discover the Higgs particle, particle collisions with a very high center-

---

[1] six quark masses, three lepton masses, three gauge couplings, four CKM parameters, the vacuum expectation value and the Higgs mass. Incorporating the non-zero neutrino masses in the Standard Model gives an additional seven or nine (in case neutrinos are Dirac or Majorana particles respectively) free parameters.

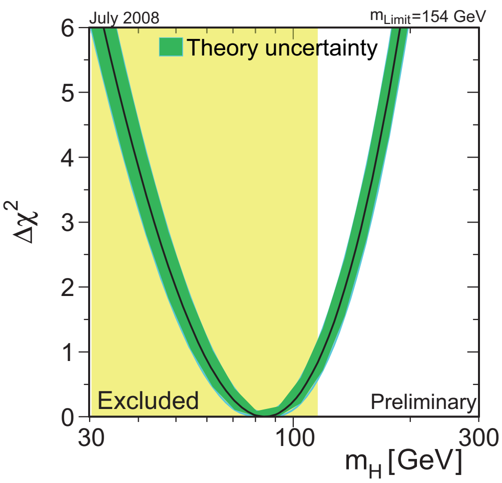

Figure 1.1: *Global fit to precision elektroweak data as a function of the Higgs mass,* m_H*. The grey area reflects the excluded region by direct searches and the associated band represents the estimate of the theoretical uncertainty. The fit gives a prediction of* $m_H < 154$ *GeV at a 95% confidence level [3].*

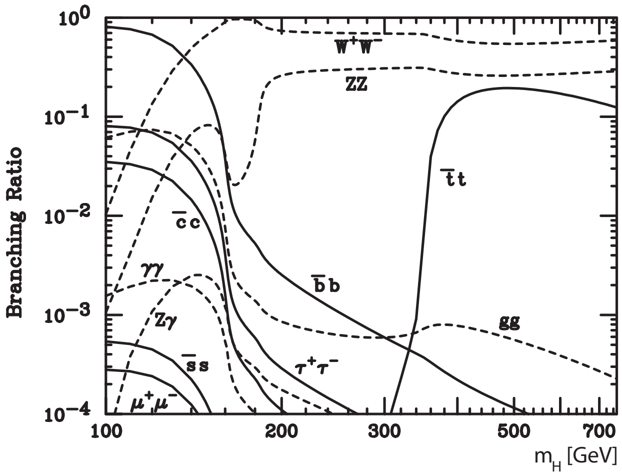

Figure 1.2: *Branching ratios for the main decays of the Standard Model Higgs boson as a function of its mass [4]. For masses below 135 GeV, the Higgs particle decays for the greater part to* $b\bar{b}$*, with smaller decays rates to* $\tau^+\tau^-$*,* $c\bar{c}$*, gluon pairs and* $\gamma\gamma$*. For masses above 130 GeV, the* W^+W^- *decay dominates with an important contribution from decays into two* Z^0*-bosons.*

of-mass energy are necessary. Since the production cross sections are small, collisions are needed in large quantities. These requirements can be achieved with a proton-proton collider. The proton-proton cross sections for several particles are shown in figure 1.3. As can be seen, the Higgs production rate increases steeply for higher center-of-mass energies.

The Large Hadron Collider (LHC) [5], which will be discussed in the next section, is a proton-proton collider and will operate at a center-of-mass energy of 14 TeV. Although one of its main goals is to detect (or to exclude the existence of) the Higgs particle, many other physics studies will be done.

The LHC will have a tremendous luminosity and interaction rate and therefore, physics processes with a small cross section can be studied, such as the, already mentioned, Higgs-boson production and beyond the Standard Model scenarios, e.g. the existence of supersymmetry (SUSY) or extra dimensions. With the unprecedented center-of-mass energy, a new energy range will be opened. Possible new heavy particles, like additional Higgs particles or the heavy charged W' and neutral Z' gauge bosons will be searched for and theories beyond the Standard Model will be tested. The most promising of such theories is supersymmetry which predicts numerous new particles within the energy range of the LHC.

Muons with a high transverse momentum are, due to their clean experimental signa-

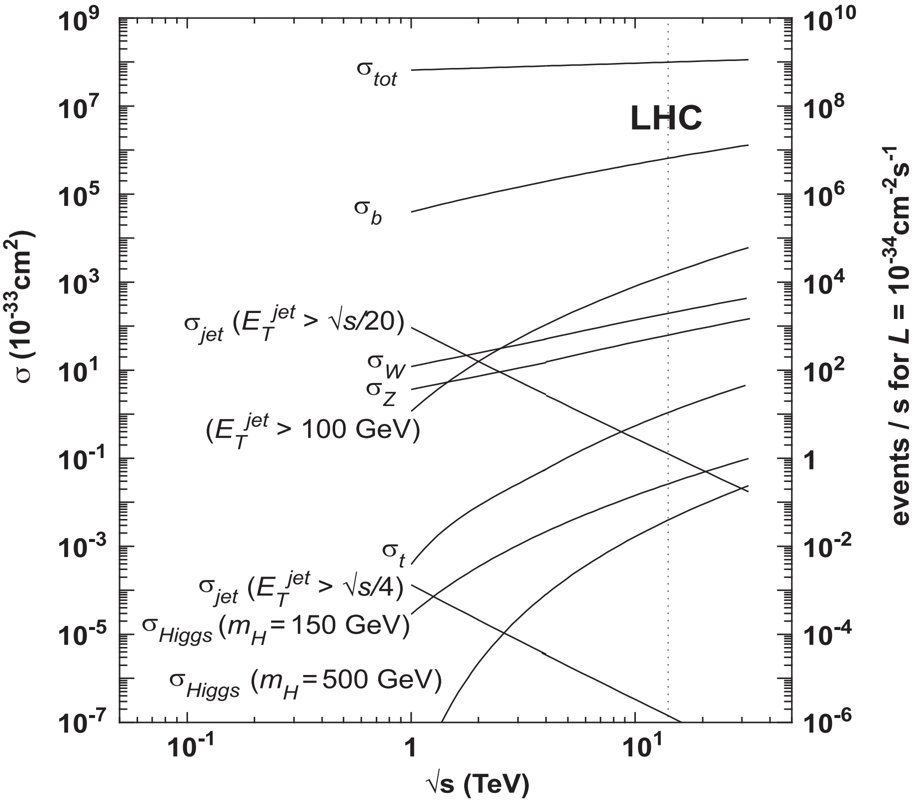

Figure 1.3: *Cross sections and event rates for various processes as a function of the proton-proton center-of-mass energy.*

ture, crucial in many of these studies. For example, for higher Higgs masses, the 'golden' Z^0Z^0 decay mode includes four muons in the final state giving a very clear experimental signature.

1.2 The Large Hadron Collider

The LHC is a proton-proton collider that is located at CERN (Geneva, Switzerland) in the same tunnel that was used for the LEP [6] accelerator. With a circumference of 26.7 km, the LHC will accelerate two counter-rotating proton beams, which will collide at a center-of-mass energy of 14 TeV at four interaction points.

Six experiments are constructed at the LHC accelerator, they are underground (typically about 100 m below ground level) in caverns excavated at the LHC's intersection points. Two of them, ATLAS [7] and CMS [8] are multi-purpose experiments, designed to explore a broad range of physics phenomena. The other four are specialised in certain fields: ALICE [9] is designed to study the quark-gluon plasma by colliding heavy ions; LHCb [10] will study properties of the b-quark, in particular CP-violation; TOTEM [11] will measure the total pp cross section and study elastic scattering and diffractive processes; LHCf [12] will investigate shower models of cosmic rays by studying particles

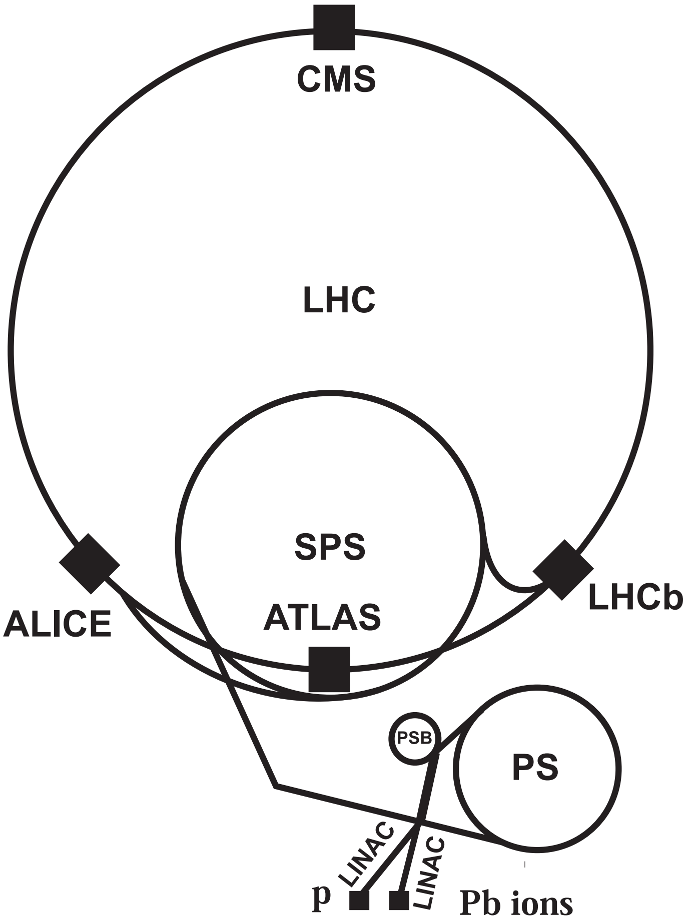

Figure 1.4: *Overview of the CERN accelerator complex (not to scale).*

emitted almost parallel to the beamline.

Prior to being injected into the main accelerator, the protons are prepared through a series of accelerators that successively increase their energy. Figure 1.4 presents a schematic overview of the accelerator complex. The protons start at a linear accelerator Linac2, which generates protons from hydrogen and accelerates them in bunches of 10^{11} protons each to an energy of 50 MeV. These bunches are then injected via the Proton Synchrotron Booster (PSB), where the energy is increased to 1.4 GeV, into the Proton Synchrotron (PS). The PS, with a circumference of 630 m, is the oldest accelerator of the CERN complex, and was already commissioned in 1959 and has been in use to provide beams for many experiments. The PS boosts the protons to an energy of 26 GeV. They are subsequently injected into the Super Proton Synchrotron (SPS), where they are accelerated to 450 GeV. In the eighties the SPS, with a circumference of 6.9 km, was used as a $p\bar{p}$ collider. The UA1 and UA2 experiments at this collider proved the existence of the weak charge carriers, the $W^{\pm}$ and the Z^0 [13], [14]. Finally, the protons are injected into the two separated beamlines of the LHC to be accelerated to their ultimate energy of 7 TeV.

The startup took place in September 2008. On the 10^{th} of September 2008 both proton beams circulated for the first time in the LHC. Beam gas events were successfully recorded in the ATLAS detector. The beam was stopped by the collimators of the accelerator in front of the ATLAS cavern, which gave enormous showers of particles inside the ATLAS detector. In the following days, the beam energy and beam collimation were gradually increased to prepare for proton-proton interactions. On the 19th of September a failure in one of the LHC-dipole magnets caused a large helium leak inside the LHC. Due to this failure, the LHC collisions are, at this moment of writing, delayed until November 2009. For initial running, the center-of-mass energy will be 7 TeV [15].

1.3 The ATLAS detector

The ATLAS (A Toroidal LHC ApparatuS) detector is a multi-purpose experiment, designed to study in detail a broad spectrum of physics processes. Figure 1.5 gives an overview of ATLAS. At design luminosity, 10^{34} $\mathrm{cm}^{-2}\mathrm{s}^{-1}$, and an estimated inelastic proton proton cross section of 100 mb, the experiment is faced with approximately 25 events per bunch crossing, which implies that about 1000 particles will be produced in the interaction point every 25 ns within the central region of the detector.

1.3.1 Detector design

The search for the Higgs particle has been taken as a benchmark for the design of the ATLAS detector. As has been discussed in section 1.1 and figure 1.2, if the Higgs mass is larger than 130 GeV, it will mainly decay into W^+W^- or two Z^0-bosons. The focus of this analysis will be on final states with leptons, and in particular muons, as these decays will give the cleanest signal. If the Higgs mass is small (below 130 GeV), several decays must be studied. While the $b\bar{b}$ decay mode has the largest branching ratio, it also has large backgrounds, e.g. from top-pair and QCD-induced $b\bar{b}$ production. Therefore, studies will also focus on decays to $\gamma\gamma$ and $\tau^+\tau^-$.

All these searches impose stringent detector criteria [7, 16]:

- Because of the very high luminosity and large particle flux, the detectors need fast, radiation-hard electronics and detector elements. A very high spatial resolution (granularity) is needed to handle the large number of particles and to reduce the influence of overlapping events;

- Large acceptance in pseudorapidity (η) with (almost) full azimuthal angle (ϕ) coverage over the full η range, so that almost no high momentum particle will remain undetected. The azimuthal angle is measured around the beam axis, and the pseudorapidity is defined as $\eta = -\ln\tan(\theta/2)$, where ($\theta$) is the polar angle measured from the beam direction. The usage of pseudorapidity is often preferred over θ as the particle rate is approximately constant as a function of pseudorapidity;

- Good muon identification and high-precision muon momentum measurements over a wide range of momenta and the ability to determine unambiguously the charge of high-p_T muons, by using the external muon spectrometer in stand-alone mode;

- Efficient tracking at high luminosity for leptons with a high transverse momentum (p_T), electron and photon identification, τ-lepton and heavy-flavour identification, and full event reconstruction capability at lower luminosity. Pixel detectors close to the interaction region are required to observe secondary vertices;

- Excellent electromagnetic calorimetry for electron and photon identification and measurements, complemented by full-coverage hadronic calorimetry for accurate jet and missing transverse energy measurements;

- Triggering on low transverse momenta particles to maintain high kinematic efficiency with sufficient background rejection to realise an acceptable trigger rate for most physics processes of interest at the LHC.

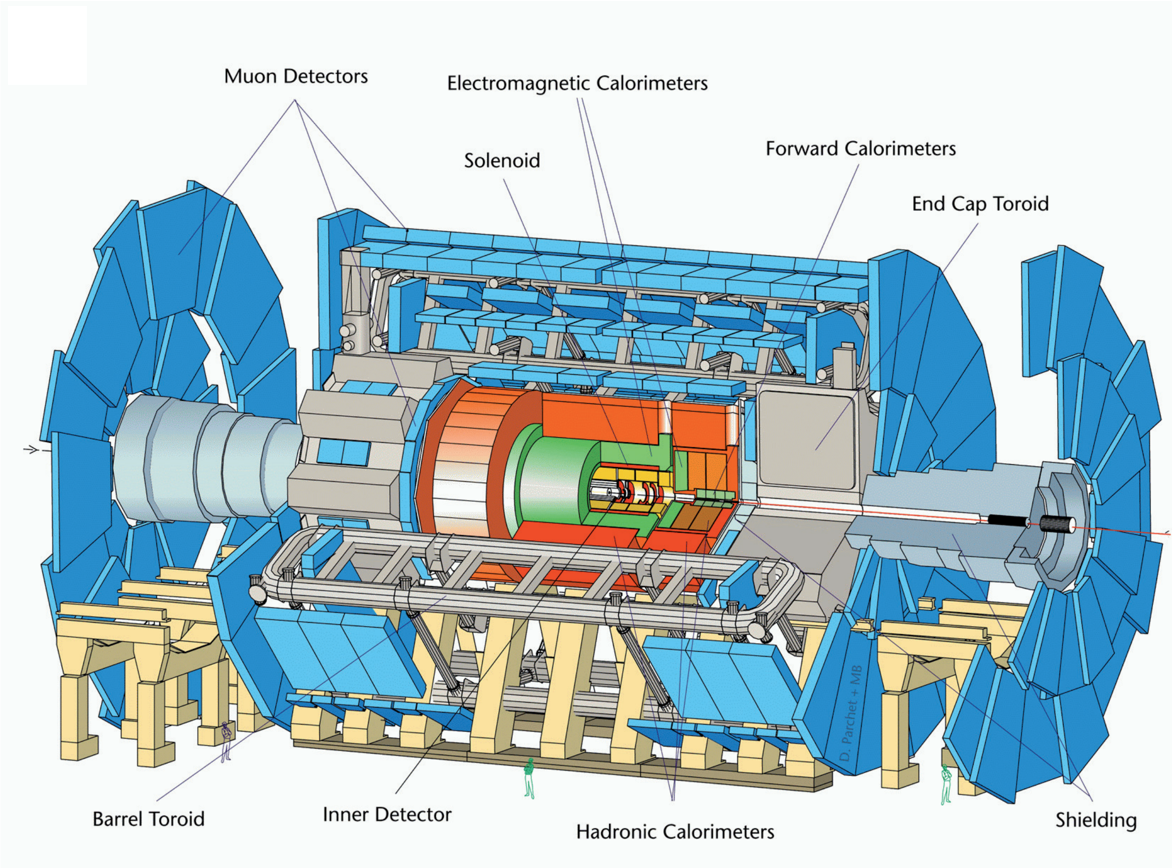

Figure 1.5: *Overview of the ATLAS detector. Some parts have been removed to show the inner structure of the detector. The various subsystems are indicated. The detector is 44 meters long and 25 meters high; it weighs approximately 7000 tonnes.*

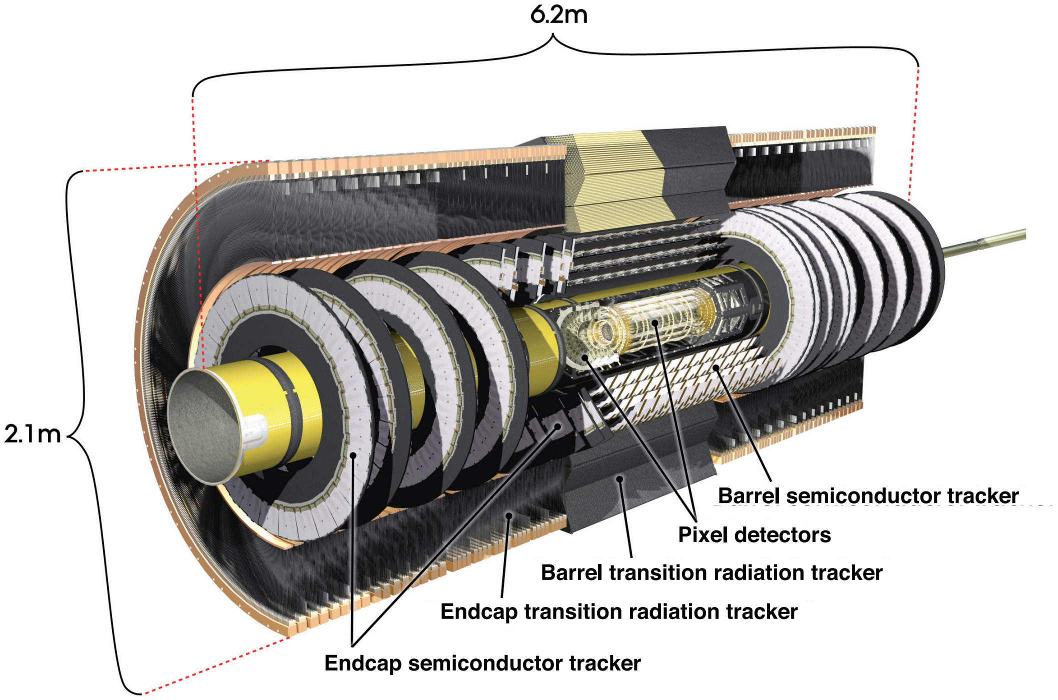

Figure 1.6: *Overview of the ATLAS inner detector. Some parts have been removed to show the inner structure of the detector. The various subsystems are indicated.*

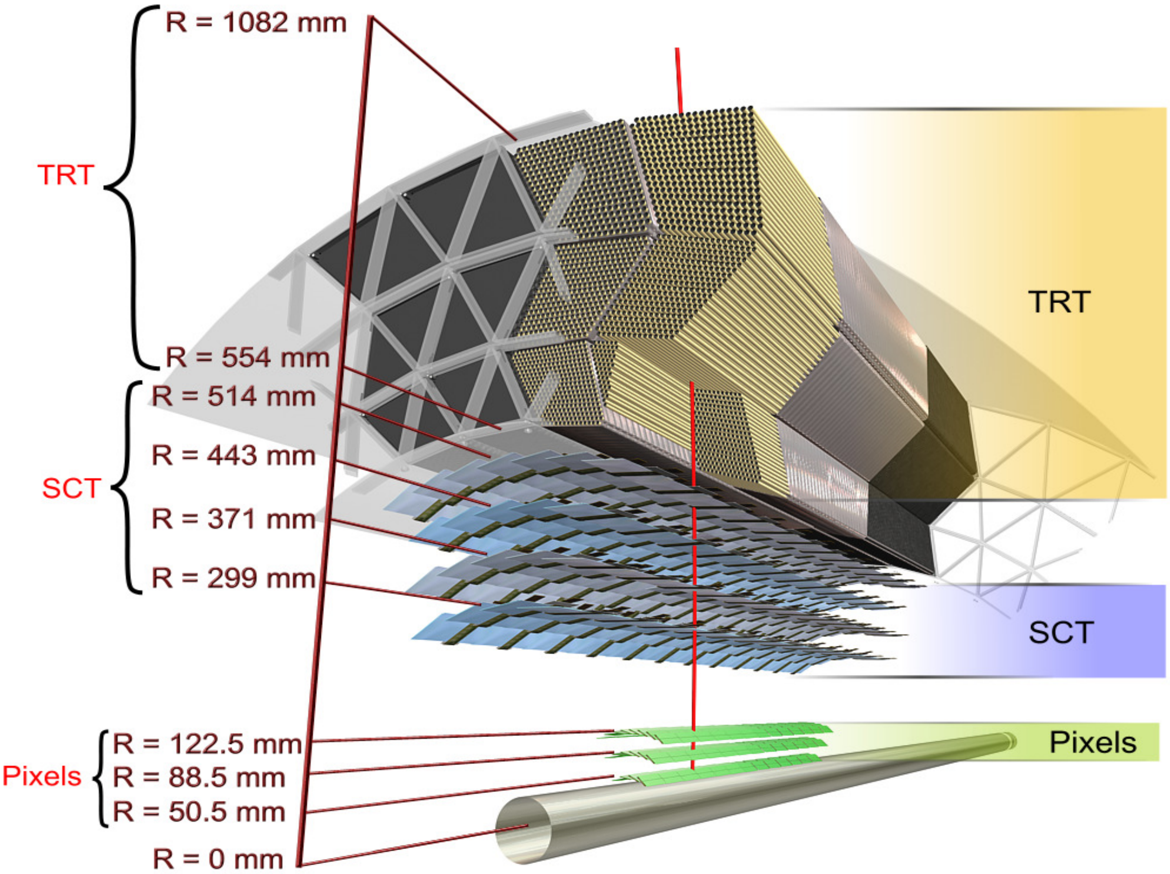

Figure 1.7: *Drawing showing the sensors and structural elements traversed by a charged particle in the barrel inner detector. The track crosses successively the beryllium beam-pipe, 3 pixel layers, 4 SCT layers and approximately 36 TRT straws.*

1.3.2 Inner detector

The ATLAS inner detector [17] is shown in figure 1.6. Its task is to track charged particles and determine their charge, momentum, direction and their vertex location. The resolution on momentum and vertex location required for the physics studies and the very large track density expected at the LHC call for high-precision measurements with fine-granularity and fast detectors. The inner detector is contained in a solenoid magnet of 2 Tesla. The magnetic field bends the charged particles thus allowing to measure the momentum by using the curvature of the tracks.

The ATLAS inner detector consists of three different subdetectors:

- Closest to the interaction point (IP), a semiconductor pixel detector, providing 3-dimensional spacepoints and secondary vertex reconstruction;
- In the middle, a silicon strip detector (SCT, 'Semiconducting Tracker'), which provides 3-dimensional spacepoints;
- Surrounding the other two, a straw tracker (TRT, 'Transition Radiation Tracker'), providing measurements in the bending plane and particle identification.

A particle from the IP traversing the complete inner detector will cross on average at least 3 pixel layers, 4 SCT strip layers and about 36 TRT tubes, see figure 1.7. The inner detector will give a typical momentum resolution of $\Delta p_T/p_T = 0.04\% \times p_T \oplus 2\%$ (p_T in GeV) and an impact parameter resolution of 15 μm in the transverse plane. The high radiation environment imposes stringent conditions on all aspects of the detectors, in particular on the radiation hardness of the front-end electronics.

The pixel detector

The pixel detector consists of three concentric layers in the barrel and three disks in each endcap. Silicon *modules* of 2×6 cm^2 with a thickness of 285 ± 15 μm are segmented into small rectangles of 50×400 μm^2, the *pixels*. There are 47,232 pixels per module and 1744 modules.

Because of its closeness to the beampipe, the pixel detector (mainly) determines the resolution of the impact parameter. Its very high granularity makes it essential for the pattern recognition.

The SCT detector

Like the pixel detector, the SCT detector uses silicon sensors, which are segmented into *strips*, giving a 1D-measurement. There are 4088 modules, with 768 strips each. The average width (strip pitch) is 80 μm, which results in an individual strip resolution of about 23 μm. A SCT module consists of two sensors with a small relative angle (stereo angle) of 40 mrad. By finding the intersection of two strips, the second coordinate can be determined with a resolution of about 800 μm. The barrel SCT consists of four concentric layers of modules and each SCT endcap has nine disks.

Due to its high granularity, the SCT is important for the momentum resolution and the initial pattern recognition. It also contributes to the resolution of the impact parameter.

The TRT detector

The TRT detector is a straw tube detector. The straws have a 4 mm diameter and are filled with a $\mathrm{Xe} : \mathrm{CO}_2 : \mathrm{O}_2 = 70 : 27 : 3$ gas mixture with 5-10 mbar over-pressure and a 31 μm gold-plated tungsten wire is positioned in the centre of each tube. When a charged particle traverses the gas, it is ionised. By applying a voltage difference over the wall of the straw and the wire, the free electrons drift towards the wire and cause further ionisation in the gas. By measuring the drift time, the minimum distance of the track to the wire can be determined with a design resolution of 130 μm.

A radiator material is positioned between the straws to produce transition-radiation photons when relativistic particles (mainly electrons due to their high γ factor) pass through. The xenon gas provides additional ionisation for these photons and this allows separation of electrons from the large $\pi^{\pm}$ background.

The length of the wires is 144 cm for barrel straws and 37 cm for endcap straws. The barrel straws are parallel to the beampipe while the endcap straws are radially perpendicular to the beampipe. In the barrel there are 52,544 straws in 73 cylindrical layers. On average a particle hits every other layer, resulting in about 36 measurements per particle. In each endcap there are 18 wheels with 319,488 straws.

The TRT is important for particle identification and defines the momentum resolution, due to its long lever arm. The large number of measurements per particle allows for track-following, which greatly enhances the performance of the pattern recognition and tracking.

The solenoid magnet

The inner detector is contained in a solenoid magnet, it has a single copper coil wound with a high-strength NbTi superconductor. The magnet is especially developed to achieve a high field of 2 Tesla, while minimising material and space. The magnet is 10 cm thick with a diameter of 2.5 m and is 5.8 m long.

Material constraint

The particles that traverse the inner detector will interact with the material from detectors, cables, support structures etc. This will degrade the performance of the inner detector. Furthermore, the calorimeters, positioned behind the inner detector, need to measure precisely the energy of all, also neutral, particles. Therefore, the amount of material in the inner detector needs to be minimised. The material is defined in terms of radiation length, which is defined as the mean distance over which a high energy electron loses all but 1/e of its energy. The thickness of the inner detector is between 0.4 and 2 radiation lengths.

1.3.3 Calorimetry

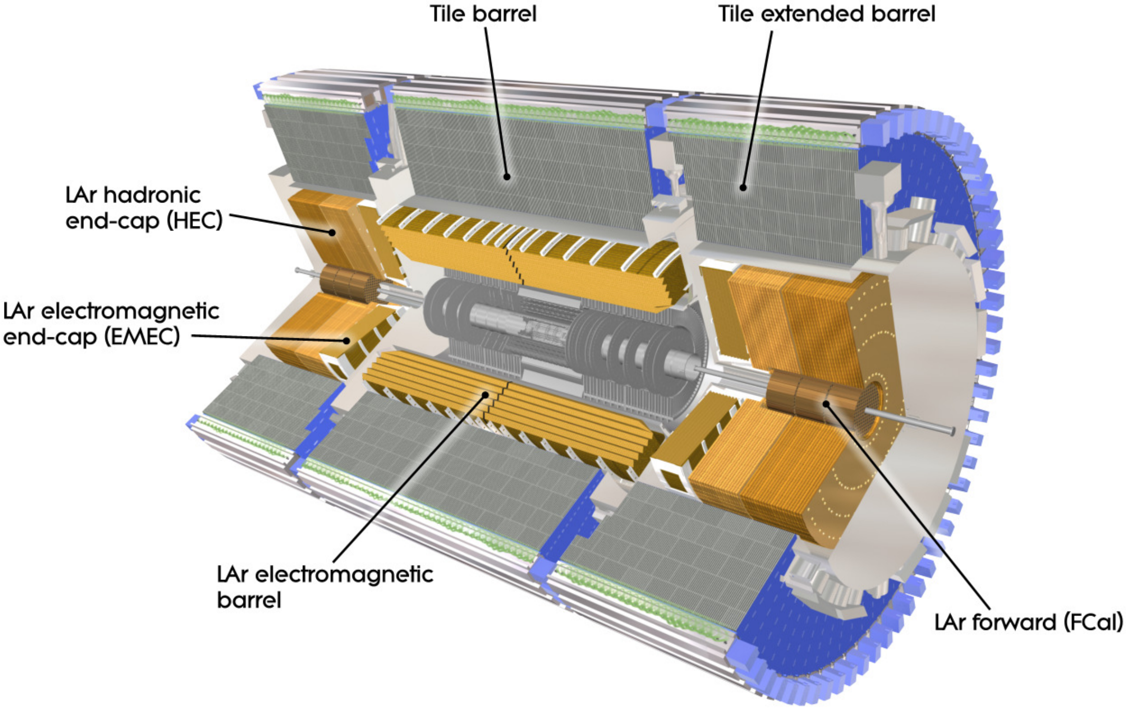

Figure 1.8: *Overview of the ATLAS calorimeter. Some parts have been removed to show the inner structure of the detector. The various subsystems are indicated.*

The ATLAS calorimeters [18] are shown in figure 1.8. Their task is to identify charged and neutral particles and jets, and measure their energy. By measuring all these energies, the missing energy in the transverse plane (E_T^{miss}) can be calculated by summing all the measured energy deposits. Missing energy can be caused by neutrinos or possibly new physics, such as supersymmetry or models with extra dimensions. The calorimeters will produce low-energy neutrons and photons, which are a large source of background noise for the muon detectors and, to a lesser extent, for the inner detector. This background is called *cavern background*.

The ATLAS calorimeter consists of three subsystems:

- The electromagnetic calorimeter;
- The hadronic calorimeter;
- A combined electromagnetic and hadronic calorimeter in the very forward regions.

The electromagnetic calorimeter

The electromagnetic calorimeter (EM) [19] measures the energy of electrons and photons. It consists of a barrel ($|\eta| < 1.5$) and two endcaps (EMEC) ($1.4 < |\eta| < 3.2$). It is a sampling calorimeter with liquid argon as the active medium and lead plates as absorber. The lead plates are accordion-shaped to provide full ϕ coverage and symmetry without azimuthal cracks. Readout electrodes are installed between the lead plates and the remaining space is filled with liquid argon. The cryostat of the liquid argon is shared with the inner detector solenoid. The barrel modules have three layers (samplings), as shown in figure 1.9. The inner layer has a high granularity in η to allow a good separation between neutral particles (photons) and charged particles, like $e^{\pm}$ and $\pi^{\pm}$.

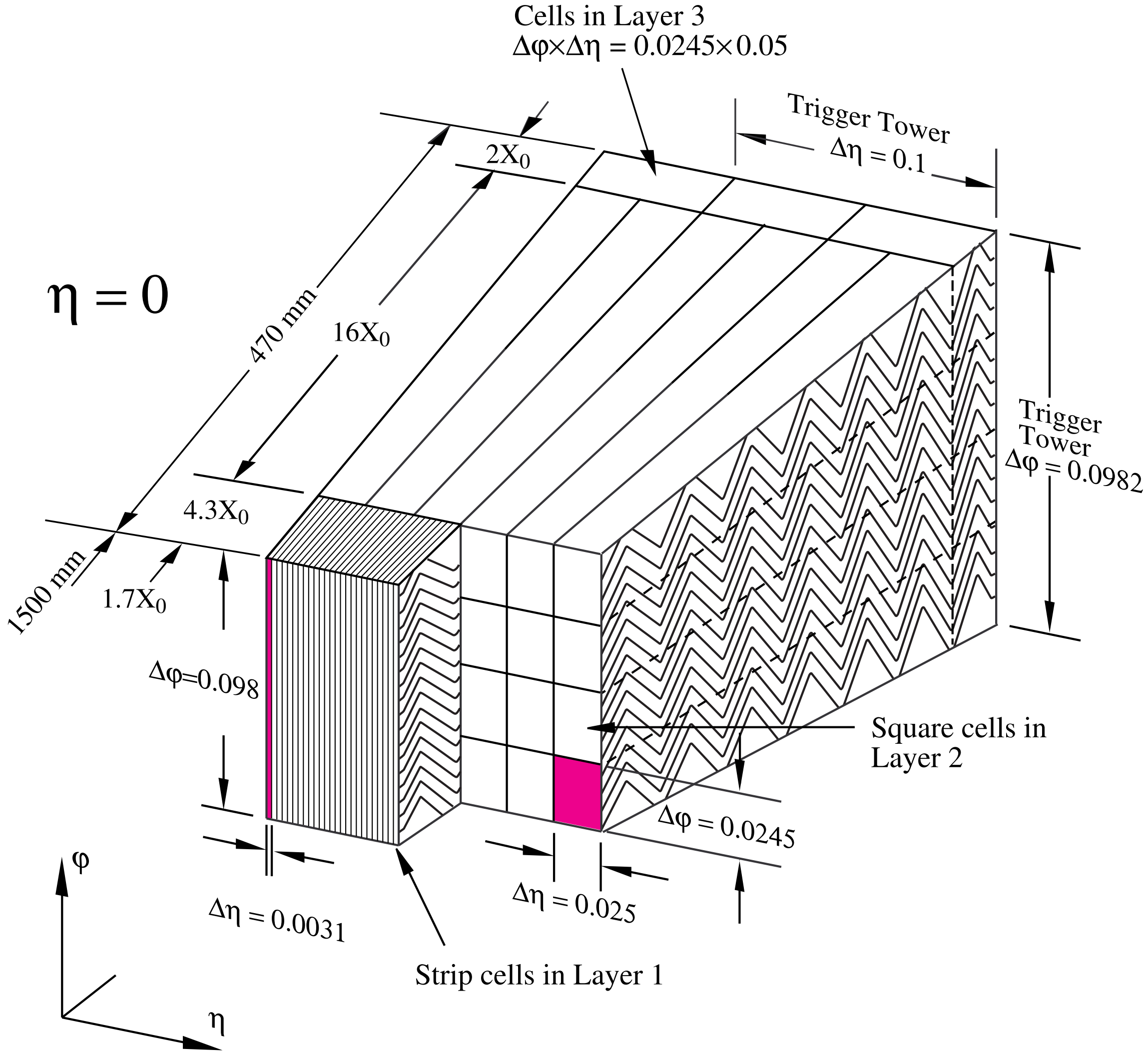

Figure 1.9: *The layout of an electromagnetic calorimeter module. The granularity in each of the three layers is shown.*

The radiation length is more than 24 radiation lengths in the barrel and more than 26 in the endcaps. Testbeam results have shown that the electromagnetic calorimeter is able to achieve an energy resolution of [20]:

$$\frac{\sigma_E}{E} = \frac{10\%}{\sqrt{E}} \oplus 0.17\% \qquad (E \text{ in GeV}). \tag{1.1}$$

The first term is the stochastic term and reflects the statistical fluctuations in the development of the shower, like the number of particles and the fraction that is lost in the absorbers. The constant term represents local non-uniformities in the calorimeter response.

High voltage tests in the ATLAS cavern show that about 2% of the total of 170,000 channels remain with shorts, and will be powered at a reduced voltage.

The hadronic calorimeter

The hadronic calorimeter has the task to identify the energy and the direction of particle jets, hadronised from quarks and gluons, and hadronically decaying τ leptons. As hadronic showers are longer, wider and have more variance in their development compared to electromagnetic showers, the hadronic calorimeter is much thicker, with an average thickness of ten interaction lengths. The interaction length is defined as the average path length of a hadron before undergoing a (nuclear) interaction.

The hadronic calorimeter is divided into a barrel part, the tile calorimeter, and an endcap, the hadronic endcap calorimeter (HEC). The tile calorimeter has a central barrel ($0 < |\eta| < 1.0$) and two extended barrels ($0.8 < |\eta| < 1.7$). Like the EM calorimeter it is a sampling calorimeter. The absorber is steel, which is also serving as the return yoke for the solenoid magnet. The active parts are scintillating tiles. The granularity of the detector is $\Delta\eta \times \Delta\phi = 0.1 \times 0.1$ (rad). Pions are reconstructed with an energy resolution of [21]:

$$\frac{\sigma_E}{E} = \frac{56\%}{\sqrt{E}} \oplus 5.5\% \qquad (E \text{ in GeV}). \tag{1.2}$$

The HEC has a coverage of $1.5 < |\eta| < 3.2$ and because of higher radiation levels, the HEC uses liquid argon as the active medium. Copper plates are used as absorber material.

The forward calorimeter

For uniformity of the calorimeter and to reduce the radiation background levels in the muon spectrometer, the forward calorimeter (FCal) is integrated into the endcap cryostat. It covers the region $3.1 < |\eta| < 4.9$. Furthermore, to reduce the amount of neutron background in the inner detector, the FCal starts 1.2 m farther away from the IP than the EM calorimeter. To achieve the same number of interaction lengths as the other calorimeters, a high-density device has been built. The FCal is split longitudinally in three parts, as is shown in figure 1.10. The absorber material for the first part is made of copper for electromagnetic measurements and the other two parts are made of tungsten for hadronic measurements. Each part has a grid of holes for the electrodes and the active material, liquid argon.

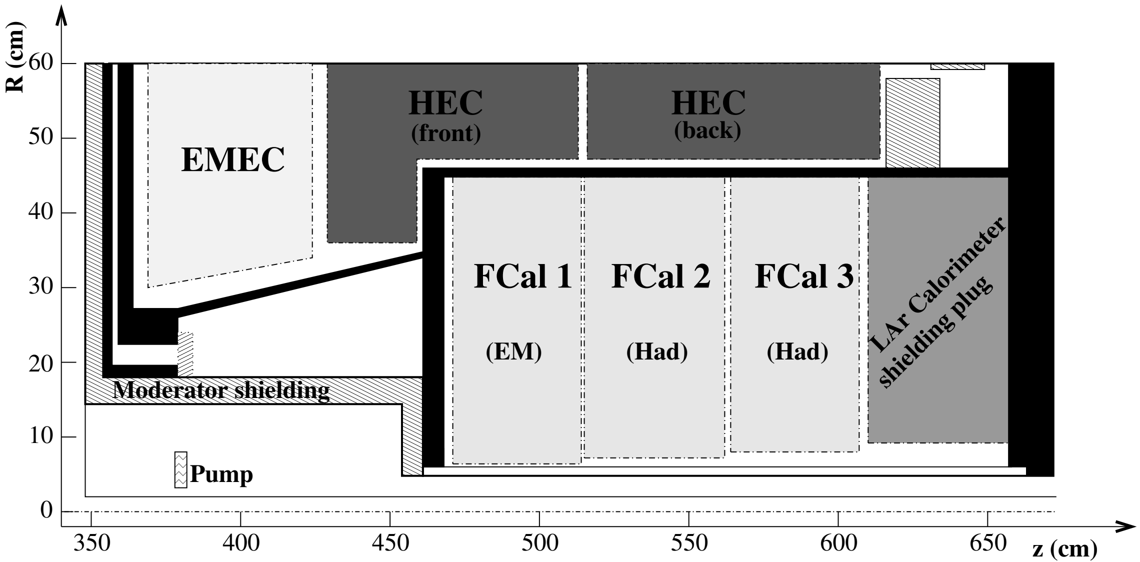

Figure 1.10: *Schematic diagram showing the three FCal modules located in the endcap cryostat. The material in front of the FCal and the shielding plug behind it are also shown. The black regions are structural parts of the cryostat. The diagram has an extended vertical scale for clarity.*

1.3.4 Muon spectrometer

The muon spectrometer is the outermost detector of ATLAS. It is designed to measure high-p_T muons with a high precision independent of the inner detector. The spectrometer also provides an independent muon trigger. Figure 1.11 shows the layout of this spectrometer. It integrates four different detector technologies and the barrel and endcap toroid magnets.

As has been explained in section 1.1, high-p_T muons provide signatures for many physics processes that will be studied by ATLAS. Therefore, the muon trigger and precision tracking are very important. By design, the nominal momentum measurement is 2-4% for 10-200 GeV muons and about 10% for 1 TeV muons. A large scale testbeam experiment, including the different technologies, has shown that this design criterium can be matched [22], [23].

Muon instrumentation

The muon spectrometer is equipped with two types of trigger detectors, the Resistive Plate Chambers (RPC) for the barrel region and the Thin Gap Chambers (TGC) in the barrel region. The Monitored Drift Tube (MDT) chambers provide the precision tracking and momentum measurement for both barrel and endcap, except close to the beampipe for the innermost layer of the endcap, where Cathode Strip Chambers (CSC) are positioned. The coverage and exact numbers of chambers and channels for the four technologies are given in table 1.1.

In the next chapter, a more detailed description of the different technologies will be

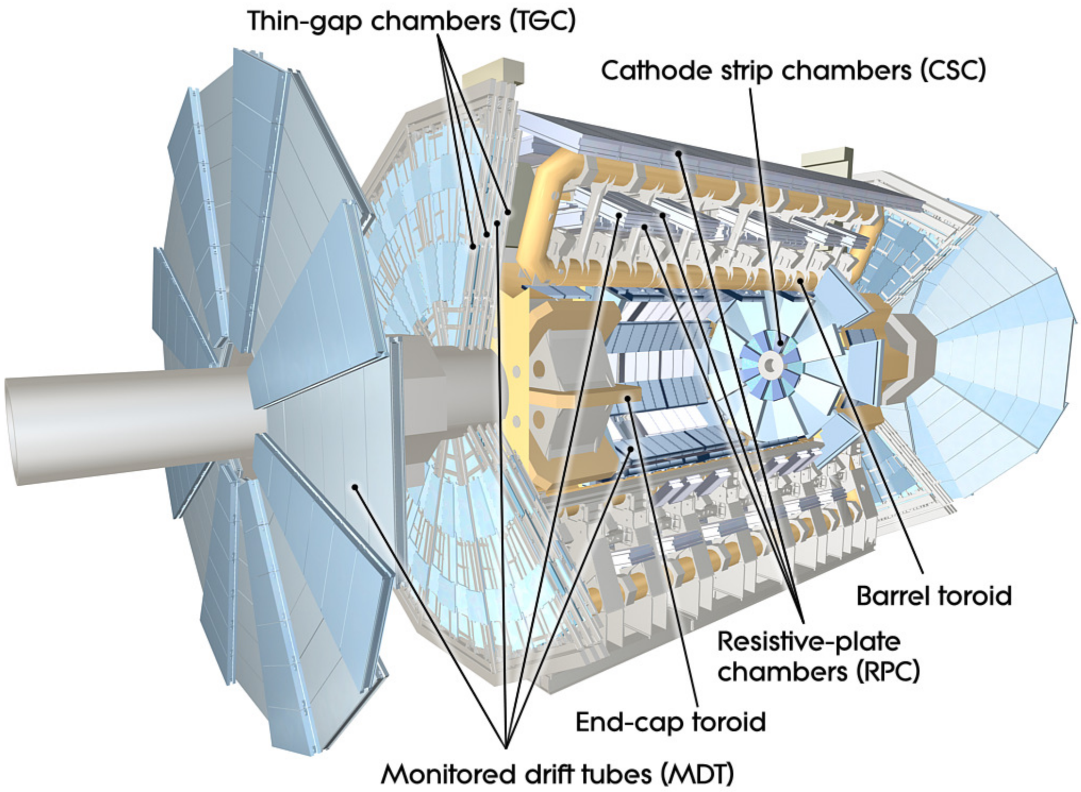

Figure 1.11: *Cut-away view of the ATLAS muon system.*

given and the expected physics performance will be discussed.

Technology	Function	Coverage	# Chambers	# Channels
MDT	tracking	$\lvert\eta\rvert < 2.7$	1150	354k
CSC	tracking	$2.0 < \lvert\eta\rvert < 2.7$	32	30.7k
RPC	trigger	$\lvert\eta\rvert < 1.05$	544	373k
TGC	trigger	$1.05 < \lvert\eta\rvert < 2.7$	3588	318k

Table 1.1: *Detector technologies of the muon spectrometer.*

Toroid magnets

The magnet system of the muon spectrometer consists of three air-core superconducting systems, one for the barrel and one for each endcap. Each of them consists of eight coils, which are positioned symmetrically around the beam axis. The barrel coils are rotated with respect to the endcap systems to provide radial overlap and optimise the bending power in the transition region.

Due to the eight coils, the magnetic field is not perfectly toroidal, but has an octagonal pattern, as is shown in figure 1.12 for the transition region. The system has an average field strength of 0.5 T. The bending power, shown in figure 1.13, ranges from 1.5 to 5.5 Tm for the barrel region at $|\eta| < 1.4$. The endcap toroid provides between 1 and 7.5 Tm for $1.6 < |\eta| < 2.7$. In the transition region, $1.4 < |\eta| < 1.6$, where the two systems overlap the bending power is smaller. While an iron core would enhance the strength and uniformity of the magnetic field, the air-core design has been chosen to reduce multiple scattering of the muons, which degrades the momentum measurement.

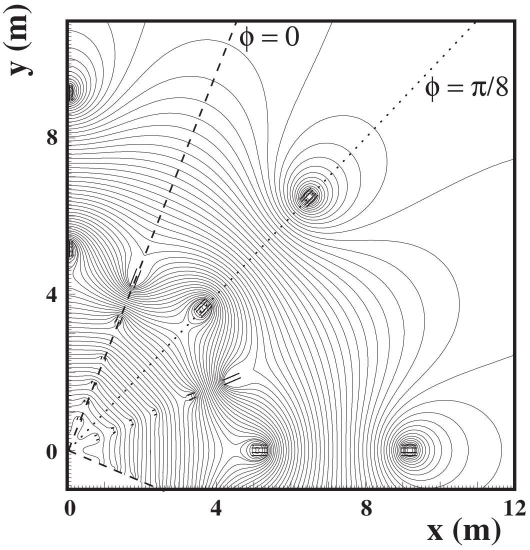

Figure 1.12: *Calculated magnetic field map in the transition region between barrel and endcap. The field lines in the transverse plane are shown. The coordinate system of the magnetic field is rotated by $\frac{\pi}{8}$ with respect to the ATLAS coordinate system.*

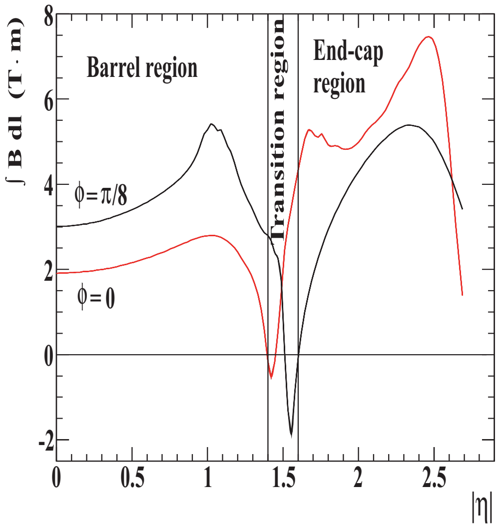

Figure 1.13: *Calculated field integral as a function of absolute η from the innermost to the outermost MDT layer in one toroid octant, for infinite-momentum muons. The curves correspond to the azimuthal angles $\phi = 0$ and $\phi = \pi/8$.*

1.3.5 Forward detectors

There are three more detectors in ATLAS not shown in figure 1.5. They are located at various distances from the interaction point and close to the beam pipe. At $z = \pm 17$ m, LUCID [24] is positioned. It is a Cerenkov detector and it detects inelastic proton-proton scattering to measure the integrated luminosity, initially with a precision of 20-30%, and later at high luminosities, a precision better than 5% is expected. A calorimeter, called ZDC [25], is positioned at a distance of ± 140 m. Its purpose is to detect forward neutrons in heavy-ion collisions. The third detector ALFA [26], located approximately ± 240 m from the IP, will measure the absolute luminosity. It consists of scintillating fibre trackers placed inside Roman pots.

1.4 Trigger system

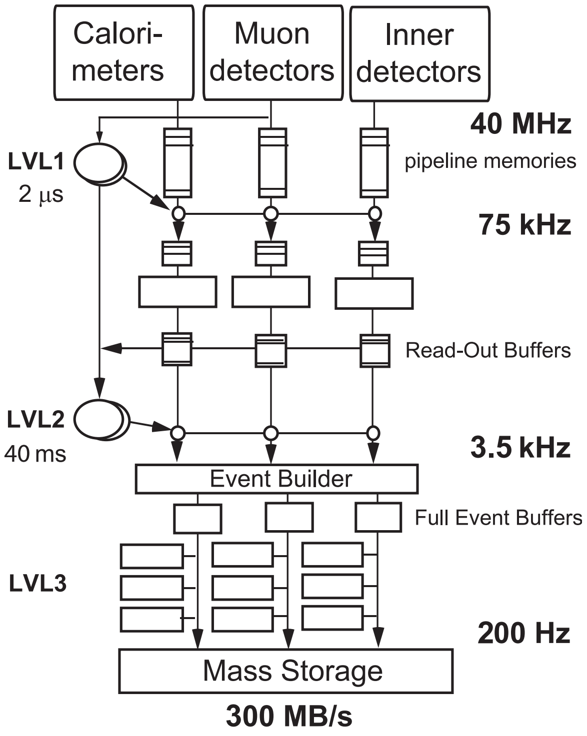

Figure 1.14: *Schematic view of the ATLAS trigger system.*

The mean data size for reading out all fired detector channels belonging to the same bunch crossing, i.e. an event, is about 1 MB. Since the bunch crossing rate goes up to 40 MHz, it is impossible to store the resulting huge amounts of data. This is not crucial, as the major part of the events will not contain interesting physics. Still, all of the interesting data needs to be stored. To achieve this, the ATLAS trigger system is developed and consists of three levels of event selection, as shown in figure 1.14. Each trigger level reduces the event rate by orders of magnitude. Each higher level has more time per event available to make a more refined decision. The final rate will be 200 Hz with an event size of about 1.5 MB, which corresponds to about 300 MB/s. Parallel processing is applied in all trigger levels to be able to handle these high rates.

1.4.1 Level-1 trigger

The level-1 trigger (L1) is a hardware based trigger that searches for high transverse momentum leptons, photons, jets and large missing and total transverse energy. It is designed to reduce the 40 MHz rate to approximately 75 kHz, with the possibility to upgrade to 100 kHz. The decision time, which is the time from the collision until the L1 trigger decision, is 2 μs. Note that already 1 μs of this time will be occupied by cable-propagation delays. The detectors used for these searches are the calorimeter and the trigger muon chambers, i.e. the RPC and the TGC chambers.

The L1 defines so-called *Regions of Interest* (ROIs). These are detector regions in η and ϕ coordinates, where interesting features have been identified. These ROIs are used by the subsequent trigger as starting point for more refined trigger algorithms.

The L1 muon trigger searches for coincidences of hits in different trigger stations within a road pointing to the IP. The width of this road is correlated with the transverse momentum. The hardware-programmable coincidence logic has six thresholds, of which three are associated with the low-p_T trigger with thresholds ranging from 6 to 9 GeV and the other three with the high-p_T trigger with thresholds from 9 to 35 GeV.

1.4.2 Level-2 trigger

The level-2 trigger (L2) is a software trigger and is seeded by the ROIs defined by the L1 trigger. The L2 uses all the detector information inside these ROIs, which accounts for about 2% of the total event data. It has dedicated trigger algorithms to make the trigger decision. The final trigger rate is about 3.5 kHz and the average processing time per event is 40 ms.

1.4.3 Event Filter

The final selection - trigger level 3 - is made by the Event Filter (EF), which reduces the event rate further to about 200 Hz. Since the average processing time per event is about 4 seconds, no dedicated algorithms have to be developed, but the standard ATLAS offline event reconstruction software can be used instead. The L2 and the EF together are called the High Level Trigger (HLT).

The decision for accepting an event is based on *trigger menus*. A trigger menu is a set of one or more event characteristics (like E_T^{miss} or a muon) with certain thresholds. The set of trigger menus can be adjusted depending on the luminosity to use the full capacity of the bandwidth.

Those events that have passed the selection criteria are tagged on basis of the results of the EF and sorted into data *streams*. The physics streams defined in ATLAS are: electrons, muons, jets, photons, E_T^{miss} and τ's, and B-physics. As ATLAS uses *inclusive* streaming, an event can be recorded in more than one stream. Table 1.2 shows the expected rates for each stream and their overlap[2]. In addition to the physics streams, there are also calibration streams that are used to calibrate the detectors, and express streams that are used for monitoring and perform data quality checks. These will only contain a subset of the data.

---

[2] Taken from https://twiki.cern.ch/twiki/bin/view/Atlas/DataStreamingStudiesOverlaps.

Stream	e	μ	Jet	γ	E_T^{miss} & τ	B-physics
e	31 ± 8	$56 \pm 6 \cdot 10^{-4}$	$53 \pm 6 \cdot 10^{-5}$	1.2 ± 0.4	1.40 ± 0.04	$1.3 \pm 1.3 \cdot 10^{-5}$
μ	-	34 ± 9	0.02 ± 0.02	$3 \pm 2 \cdot 10^{-3}$	0.2 ± 0.02	0.076 ± 0.004
Jet	-	-	38 ± 6	0.5 ± 0.5	0.7 ± 0.4	0 ± 0
γ	-	-	-	22 ± 6	0.22 ± 0.07	0 ± 0
E_T^{miss} & τ	-	-	-	-	32 ± 8	$1.5 \pm 0.6 \cdot 10^{-5}$
B-physics	-	-	-	-	-	10 ± 5

Table 1.2: *Expected rates and overlaps (Hz) for the physics data streams at a luminosity of* 10^{33} $cm^{-2}s^{-1}$.

Chapter 2

The ATLAS muon spectrometer

This chapter will describe the ATLAS muon spectrometer in more detail. The four different detectors are each covered with a particular focus on their use in tracking. The geometry, the detection mechanism, timing issues, calibration and alignment will be discussed. The first section will describe the design of the spectrometer, then the four technologies will be discussed; first the trigger chambers and then the precision chambers. In the final section, the performance of the spectrometer is covered.

2.1 Muon spectrometer design

High energy muons are a signature of interesting physics. They appear in Standard Model physics, such as measurements on Z^0 and W-bosons and searches for the Higgs-boson, especially in its W^+W^- and Z^0Z^0-decay modes. But also in searches for physics beyond the SM, e.g. for supersymmetry, heavy gauge bosons and additional Higgses, high energy muons are often used as a crucial signature.

Driven by the physics motivation as outlined in section 1.1, the ATLAS muon spectrometer has two main objectives: to provide a standalone and momentum dependent trigger and secondly to provide standalone muon reconstruction. These objectives are each fulfilled by a separate system of detectors.

For physics studies and therefore, for standalone muon reconstruction, the most important properties of the muon that should be determined are its charge and its momentum.

The muon momentum can be determined by measuring the position of the muon at three points in space. The trajectory of the muon is curved due to the magnetic field and the higher the momentum the less curvature. The curvature is measured in the track fit where the magnetic field is known in detail. However, for a good approximation and practical

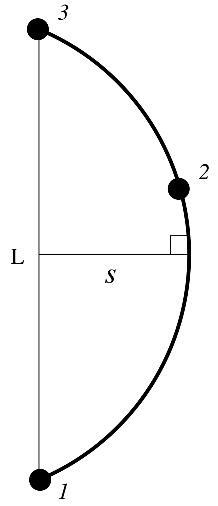

Figure 2.1: *Sagitta (s) in three-point measurement. L is the distance between the outer measurements 1 and 3.*

application the *sagitta* is used. The sagitta is defined as the maximum deviation of a circle from a straight line, see figure 2.1. Note that the sagitta is larger and can be measured with higher relative accuracy, when the distance L between the outer measurements 1 and 3 is larger. The sagitta is linked to the transverse momentum p_T of the muon:

$$p_T = \frac{L^2 B}{8s} \tag{2.1}$$

where B is the magnetic field strength. Note that the relative error on the momentum is proportional to the relative error on the sagitta.

For the endcap, the momentum measurement is slightly different as there is no magnetic field between the middle and outer stations, so the trajectory is not a curve. Instead the direction between the IP and the measurement in the inner layer is compared with the direction of the measurements in the middle and outer layer.

To be able to reconstruct the momentum with the described three-point method, the muon spectrometer is designed such that every muon with $|\eta| < 2.7$ will cross at least three detector stations with the exception of a few regions with less coverage. When a particle traverses only 2 stations, the IP is taken as the third measurement and the momentum determination is based on the difference between the angles to the IP. As there is a relatively large uncertainty on the scattering in the calorimeter, such a measurement is less precise. The muon spectrometer is designed with the requirement of a 10% precision on the transverse momentum for 1 TeV muons. Given the magnet system, the sagitta will be about 0.5 mm for 1 TeV muons. Therefore, to get a 10% error on the momentum, a 50 μm precision on the sagitta is required[1].

The design of the muon spectrometer is shown in figures 2.2 and 2.3 [27]. The barrel part of the muon spectrometer consists of three concentric layers at radii of about 5 (inner layer), 8 (middle) and 10 (outer) meters. Each layer consist of Monitored Drift Tube (MDT) chambers. The middle and outer layer are in addition equipped with Resistive Plate Chambers (RPC). The MDT chambers provide precision measurements to determine the momentum. The RPC chambers provide the barrel trigger system. In the endcap, shown in figure 2.2, a similar layout is followed. Three wheels of MDTs are mounted perpendicular to the beam axis at a longitudinal distance of 7.5, 14 and 22.5 meters, with an exception of the innermost layer, where close to the beampipe Cathode Strip Chambers (CSC) replace the MDT chambers. For the endcap, a different trigger chamber technology, the Thin Gap Chambers (TGC), has been chosen.

In table 2.1 the parameters of the four technologies in the muon spectrometer are shown. The individual technologies will be discussed in the following sections. By design, each tracking station provides an error of approximately 35 μm. The alignment system, based on tracks and an optical system, will give an additional inaccuracy of 30 μm.

---

[1] The magnetic field is known to a much higher precision of 4 mT, i.e. a relative precision of about 1%.

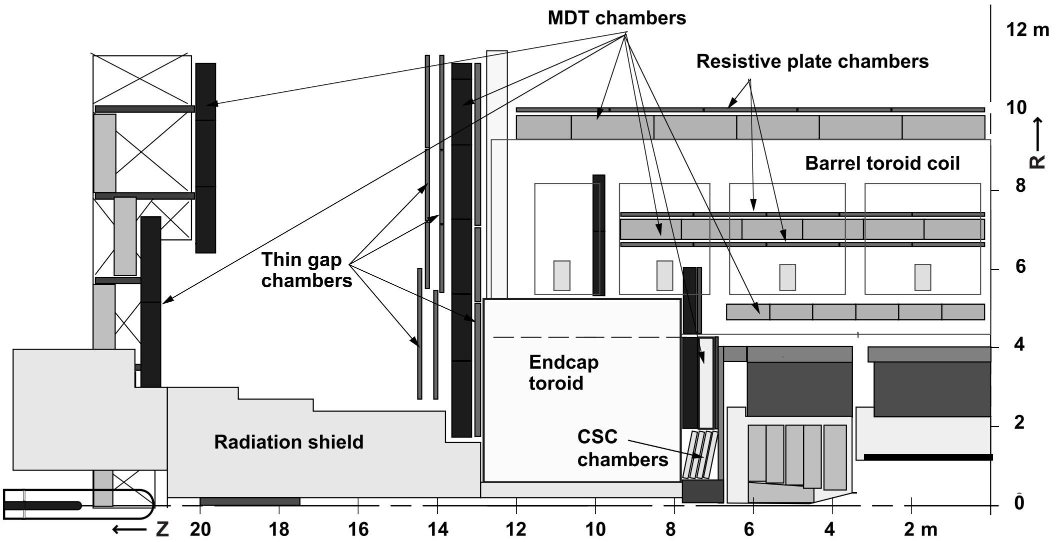

Figure 2.2: *Cross section of the muon system in a plane along the beam axis (bending plane). Infinite-momentum muons would propagate along straight trajectories and typically traverse three muon stations.*

			Chamber resolution (RMS)			**hits/muon**	
Type	**Function**	**Coverage**	z/R	ϕ	time	barrel	endcap
MDT	tracking	$\lvert\eta\rvert < 2.7$[1]	35 μm (z)	—	—	20	20
CSC	tracking	$2.0 < \lvert\eta\rvert < 2.7$[2]	40 μm (R)	5 mm	7 ns	—	4
RPC	trigger	$\lvert\eta\rvert < 1.05$	10 mm (z)	10 mm	1.5 ns	6	—
TGC	trigger	$1.05 < \lvert\eta\rvert < 2.7$[3]	2-6 mm (R)	3-7 mm	4 ns	—	9

Table 2.1: *Parameters of the four subsystems of the muon spectrometer. The quoted spatial resolution (columns 4 and 5) does not include chamber-alignment uncertainties. Column 6 lists the intrinsic time resolution of each chamber type, to which contributions from signal-propagation and electronics distributions need to be added.*

These individual errors are sufficiently small to obtain the required overall precision of 50 μm. In addition, charge identification will be possible even for the most energetic ($\sim$ 3 TeV) muons. For momenta below 200 GeV, where a momentum resolution of 2-4% is reached, other effects, such as multiple scattering and fluctuations in the energy loss in the calorimeters become important. Figure 2.4 shows the various contributions to the momentum resolution as a function of transverse momentum for the barrel ($|\eta| < 1.5$) and endcap ($|\eta| > 1.5$) region. Note that the multiple scattering contribution is computed as the quadratic difference between the resolution evaluated with and without the material included in the calculation. Three different regimes can be identified:

---

[1] innermost layer: $|\eta| < 2.0$.

[2] only innermost layer.

[3] for triggering: $1.05 < |\eta| < 2.4$.

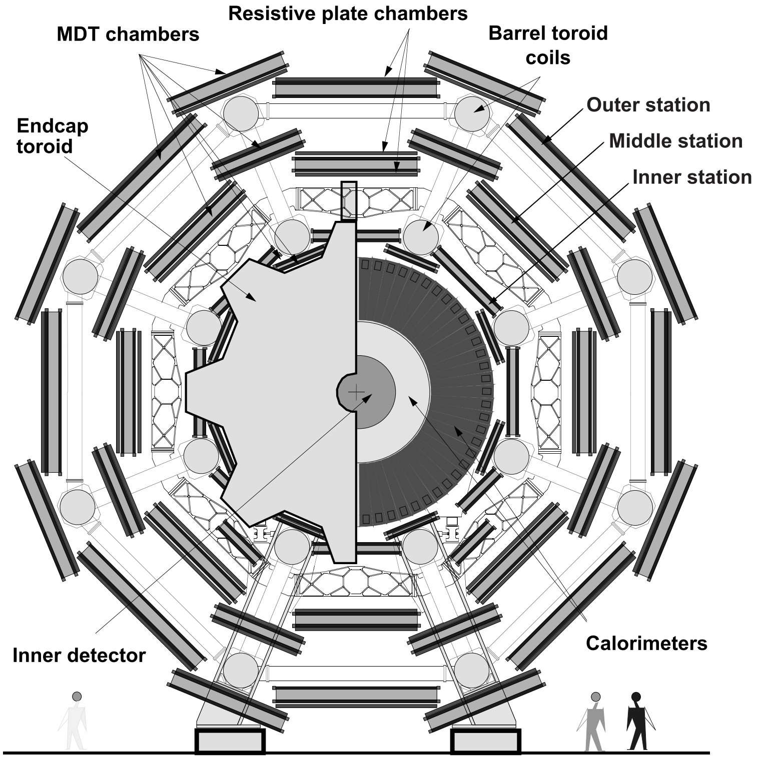

Figure 2.3: *Cross section of the barrel muon system perpendicular to the beam axis (non-bending plane), showing three concentric cylindrical layers of eight large and eight small chambers each. The outer diameter is about 20 m.*

- $p_T < 30$ GeV, for low momenta, the resolution is defined by the fluctuations of the energy loss in the calorimeter;
- $30 < p_T < 200$ GeV, for intermediate momenta, the resolution is dominated by multiple scattering;
- $p_T > 200$ GeV, for high momenta, the resolution is determined by the intrinsic MDT tube resolution and the alignment of the chambers.

The differences between the barrel and endcap are caused by the fact that for equal transverse momentum, the total momentum of a muon is larger in the endcap.

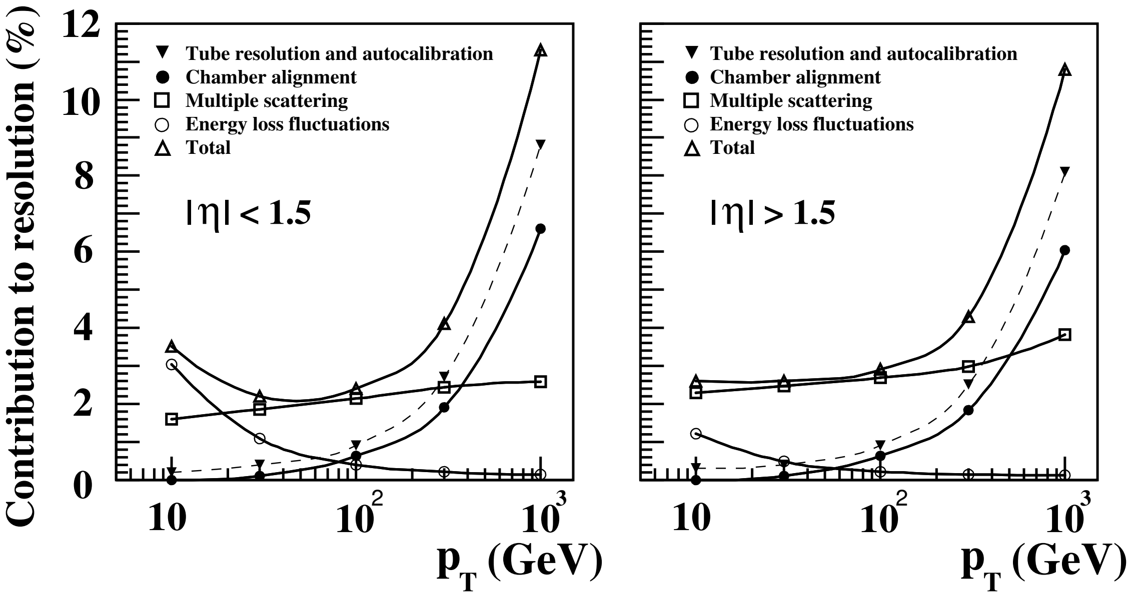

Figure 2.4: *Contributions to the transverse momentum resolution, averaged over* $|\eta|$ *< 1.5 (left plot) and averaged over* $|\eta|$ *> 1.5 (right plot) [27].*

2.1.1 Rate environment

Besides the required precision of the transverse momentum, a major impact on the spectrometer design is the particle flux. It influences various aspects of the detectors, such as the rate capability and the ageing. Also the granularity has to be chosen accordingly, since that has direct consequences for the pattern recognition efficiency and the momentum resolution tails from incorrect hit assignment.

In proton-proton collisions various types of muon sources can be distinguished. Prompt muons are produced in the decays of heavy flavor hadrons ($c, b, t \rightarrow \mu X$) and gauge bosons ($W, Z^0, \gamma^* \rightarrow \mu X$). These muons are produced close to the IP and need a minimum momentum of about 3 GeV to reach the muon spectrometer. Muons produced by light hadrons, such as pions and kaons, can produce signals in the spectrometer either by decaying in flight, showering in the calorimeter (*shower muons*), or travelling through the calorimeter, so-called *punch-through*. Figure 2.5 shows the cross sections of these various sources as a function of p_T. For $p_T > 8$ GeV, the total muon cross section is dominated by decays from heavy flavor hadrons. However note that this estimate has large uncertainties due to the uncertainty on the heavy quark production rate. In figure 2.6 the cross section is shown as a function of η. As is expected from the definition of pseudorapidity, the muon rate is indeed constant over the whole η range. The total rate is dominated by low-p_T pion and kaon decays. For design luminosity, the rate is estimated to a few Hz/cm^2 for $\eta = 0$ and several tens of Hz/cm^2 for $\eta = 2$.

Besides the primary muons, several sources produce background hits in the detectors. The main source comes from the shielding and the, mostly forward, calorimeters. When secondary particles are absorbed in the shielding and the calorimeter, thermalised

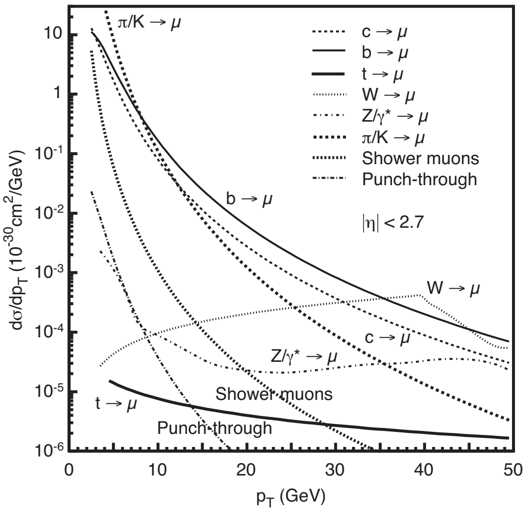

Figure 2.5: *Transverse momentum dependence of the muon cross section from various sources integrated over $|\eta| < 2.7$. The horizontal scale is the transverse momentum at production.*

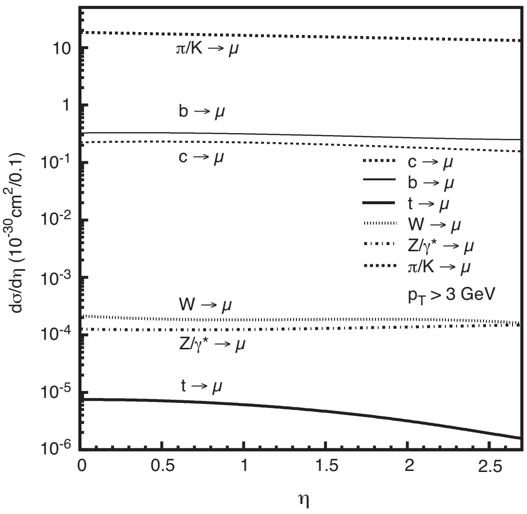

Figure 2.6: *Rapidity dependence of the muon cross section from various sources integrated over $3 < p_T < 50$ GeV.*

neutrons are produced that might escape into the spectrometer and produce Compton electrons, spallation protons and low-energy photons. This is called *cavern background.* The estimates for the cavern background rates are uncertain and vary up to a factor five [27]. Other sources such as beam halo and cosmic ray showers are less dominant.

2.2 Muon trigger

The muon trigger system provides fast information on muons traversing the detector. The main requirements for the system are:

- **Momentum dependent trigger:** The L1 trigger should be able to determine the approximate momentum range. This allows for more complex trigger menus and pre-scaling in high luminosity runs;
- **Bunch crossing identification:** For physics studies, it is crucial to determine the bunch crossing the particle originated from. This task is non-trivial, as there are particles from up to four bunch crossings in the detector at the same time;
- **Second coordinate measurement:** The MDTs measure the coordinate in the bending plane, however no precision in the non-bending plane is reached, as shown in table 2.1. The trigger chambers provide this second coordinate measurement;
- **Robustness against cavern background:** Triggers from random hits from thermalised neutrons and photons in the cavern should be minimal.

The trigger coverage is $|\eta| < 2.4$ over the full ϕ-range. A schematic layout of the trigger chambers is shown in figure 2.7.

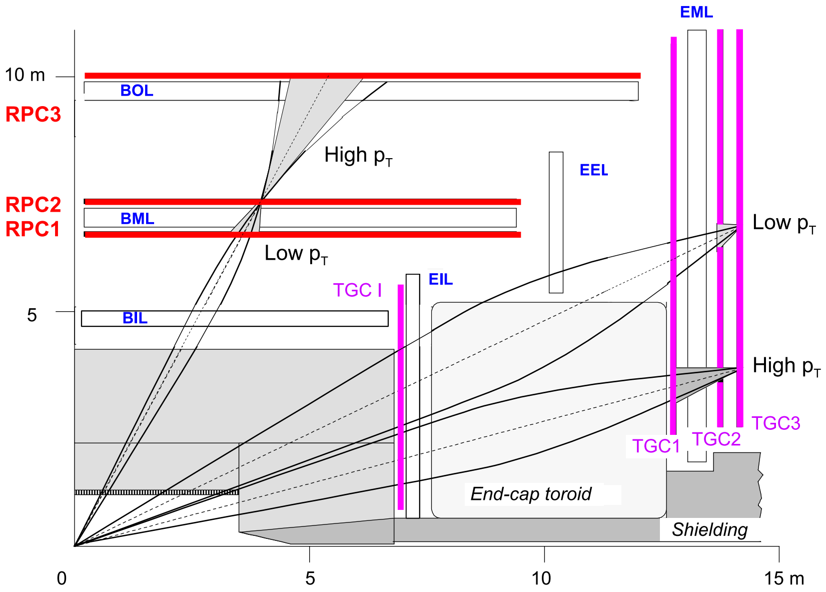

Figure 2.7: *Cross-section of the muon system in a plane along the beam axis (bending plane), showing the position of the muon trigger chambers. Also shown is which measurement planes provide the low- and high-p_T trigger.*

Compared to the barrel region, several complications arise when triggering in the endcap region:

- **Increased momenta:** For larger η, momenta increase for a given transverse momentum, e.g. for $\eta = 2.4$, the total momentum is 5.8 times larger than its transverse part, while the bending power is only twice as large as in the barrel;

- **Chamber positions:** As can be seen in figure 2.7, the trigger chambers are closer to each other in the endcap and are outside the magnetic field, thus not measuring any curvature;

- **Higher rates:** Muon rates of 20 Hz/cm^2 are up to a factor 10 higher than in the barrel;

- **Inhomogeneous magnetic field:** In the magnetic field transition region ($1.3 < |\eta| < 1.65$) there are strong inhomogeneities and most tracks will be nearly straight.

To provide an equal performance in momentum resolution and efficiency as the barrel trigger, the endcap chambers need an increased granularity at larger η. To account for these complications two different technologies have been chosen. In the barrel ($|\eta| < 1.05$), RPCs have been installed. They have a good spatial and time resolution. In the endcap ($1.05 < |\eta| < 2.4$), TGCs have been selected, which provide good time resolution and are capable to handle high rates.

2.2.1 Resistive Plate Chambers

The muon trigger in the barrel consists of RPCs. Like the MDT chambers, the RPCs are positioned in three concentric layers around the beam axis, as shown in figures 2.7 and 2.3. The two inner chambers are assembled together with the middle MDT chambers, and the outer layer is assembled on the outer MDT chambers; on top of the MDT chamber for the large sectors, and below the MDT chamber for the small sectors. No gaps in ϕ are present in this configuration.

Due to the large lever arm between inner and outer RPCs, the trigger is able to select high momentum muons with thresholds ranging from 9 to 35 GeV. The inner RPCs deliver the low momentum trigger with thresholds from 6 to 9 GeV. This is illustrated in figure 2.7.

Each RPC has independent layers for ϕ and η measurements. Therefore, a muon trajectory usually provides six RPC measurements.

Operation principle

The RPC is a gaseous detector with 2 mm gas-gaps in between two parallel resistive plates. The gas-gaps are filled with $C_2H_2F_4 : \mathrm{Iso}C_4H_{10} : SF_6 = 94.7 : 5 : 0.3$. Metallic strips are mounted onto these plates with a pitch between separate ϕ (η) strips of 23 (35) mm. The plates are operated at a voltage difference of 9.8 kV, as a result of which a charged particle crossing the gas-gap will create an avalanche of electrons drifting towards the anode. Each chamber consists of two units, placed next to each other with a small overlap. Each unit has two gas-gaps, one for ϕ and one for η. The detection efficiency of a single layer, including spacers and frames, is measured to be larger than 97% [16].

2.2.2 Thin Gap Chambers

For the endcaps a slightly different technology is chosen. TGCs are positioned in four planes around the beam axis, as depicted in figure 2.7. While the RPCs are physically connected to an MDT counterpart, there is no such connection for the TGCs. The TGC inner layer ($1.05 < |\eta| < 1.92$) is mounted on the support structure of the barrel toroid coils at $|z| \sim 7$ m and is segmented in two non-overlapping parts, an endcap and a forward part. Each chamber has a doublet of two layers of TGCs.

The three other TGC planes are mounted on so-called wheels at $|z| \sim 14$ m and will give seven measurements in total, one plane of triplet chambers (TGC1, $1.05 < |\eta| < 2.7$), and two planes of doublet chambers (TGC2-TGC3, $1.05 < |\eta| < 2.4$). The TGC1 layer provides second coordinate measurements up to an $|\eta|$ of 2.7, however since there are no coincidences in the other planes, these measurements are not used for triggering.

Operation principle

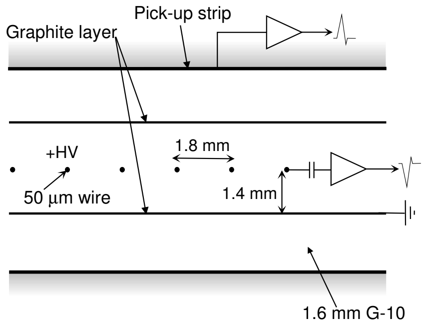

Figure 2.8: *TGC structure showing anode wires, graphite cathodes and a pick-up strip, orthogonal to the wires.*

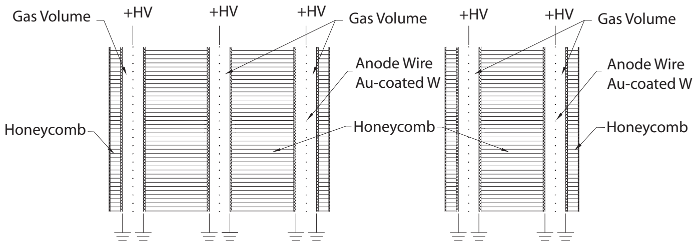

Figure 2.9: *Cross section of a TGC triplet and doublet module. The dimensions of the gas-gaps are enlarged with respect to the other elements.*

TGCs are multiwire proportional chambers. The active parts of a chamber are shown in figure 2.8. Position measurements are obtained from both the pick-up strips (ϕ) and the wires (η). The wires are operated at 2.9 kV and the used gas mixture is $CO_2 : n\text{-}C_5H_{12} = 55 : 45$.

The number of wires in one gas-gap varies between 6 and 31 as a function of η to obtain the required momentum resolution. There are two types of TGC modules as shown in figure 2.9. A doublet module has two wire layers, and a triplet module three. Both structures have two strip layers. Note that in the figure the width of the gas-gaps is enlarged compared to the other elements.

2.3 Precision measurements

Precision tracking is performed by the MDT chambers throughout all of the muon spectrometer, except for the innermost part of the endcap inner layer. In this region, due to thermalised neutrons coming from the calorimeter, the expected particle rates for high luminosity running are expected to be higher than 150 kHz/cm^2. This is considered to be the limit for the MDT chambers as the occupancy will become too high. Here, the CSC technology is chosen which provides a similar spatial resolution as the MDT chambers, but an increased high-rate capability and low neutron sensitivity.

2.3.1 Cathode Strip Chambers

The CSCs are segmented in ϕ on two wheels of eight chambers each, as shown in figure 2.10. CSCs are multi-wire proportional chambers. The (anode) wires are oriented in the radial direction and have (cathode) strips oriented perpendicular to them, in either η or ϕ. The CSC structure is shown in figure 2.11. A crossing muon will cause charges on

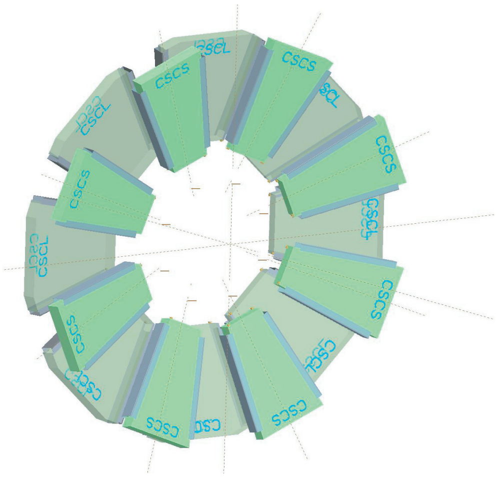

Figure 2.10: *Layout of a CSC end-cap wheel with eight small and eight large staggered chambers.*

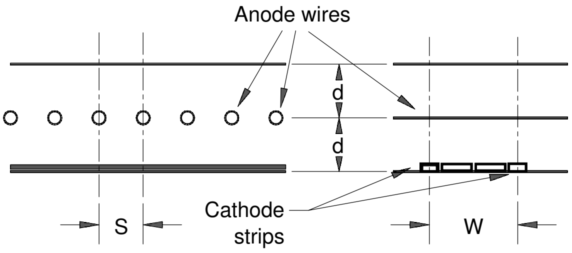

Figure 2.11: *CSC structure showing anode wires and cathode strips. The wire spacing S and the cathode-anode distance d are 2.54 mm. The cathode readout pitch W is 5.08 mm.*

several strips. Interpolation between the charges will provide the position. Each crossing muon will give four independent measurements in both η and ϕ with a resolution of 60 μm in η and 5 mm in ϕ.

This design makes the chambers effective in high particle density environments. Due to the small gas volume and the used gas mixture of Ar : $CO_2 = 80 : 20$, the sensitivity for neutrons is low and the drift times are small, resulting in a time resolution of 7 ns. Furthermore, due to the ability to combine measurements in the η and ϕ coordinate, it is possible to resolve ambiguities when more than one particle is present.

When combining the eight measurements, the total chamber resolution in η is 30 μm and 1.15 mrad.

2.3.2 Monitored Drift Tubes

By far the largest area of precision chambers in the muon spectrometer is occupied by the MDT chambers. Therefore, this technology predominantly determines the measurements of the properties of the muon and is most important for the reconstruction.

A schematic view of a barrel MDT chamber is shown in figure 2.12. Like the other muon technologies, the MDT chamber is a gaseous detector. However in an MDT chamber each detector element has its own gas volume. The cross section of the MDT tube is shown in figure 2.13a. An MDT chamber consists of two so-called multilayers, which in turn consist of three or four layers of tubes each. Due to the higher particle rate the innermost layer of chambers has four layers of tubes to improve the local pattern recognition. An MDT chamber has an internal alignment system, which will be discussed

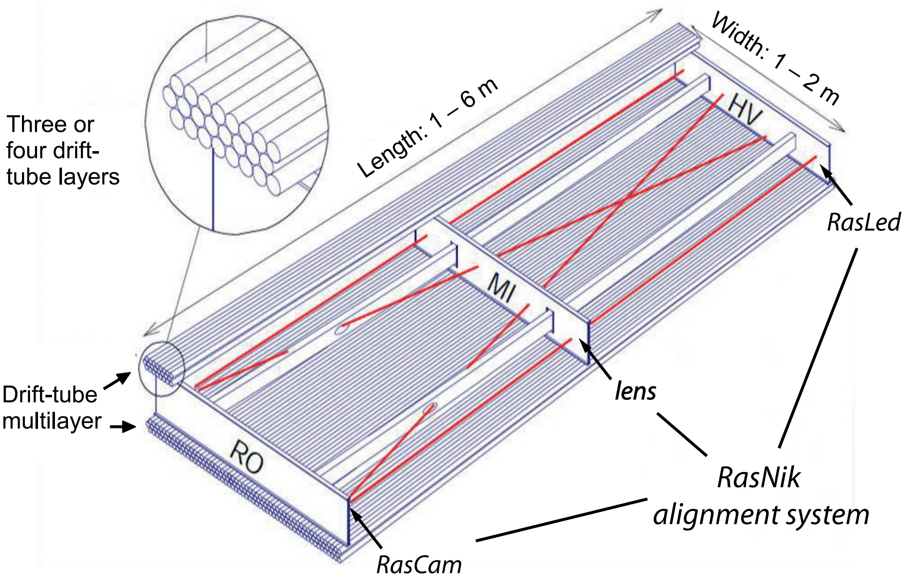

Figure 2.12: *Schematic view of a barrel MDT chamber.*

at the end of this section.

In the barrel region ($|\eta| < 1.3$), as shown in figure 2.3, the MDTs are positioned in three concentric layers around the beam axis, at an approximate radius of 5, 8 and 10 m. There is a 16-fold segmentation in ϕ, which are called *sectors*. To avoid holes in the acceptance, the chambers are partly overlapping.

The endcap ($1.3 < |\eta| < 2.4$) MDT chambers are assembled onto three wheels, positioned at z = 7.5, 14 and 22.5 m. These chambers are trapezoidal shaped. There are again small and large chambers having small overlaps to prevent any cracks in the detector coverage.

Each chamber type is identified with a three letter name. The first letter indicates if the chamber is a barrel (B) or endcap (E) chamber; the second letter if the chamber is an inner (I), middle (M) or outer (O) chamber; and the third letter if the chamber is a small (S) or large (L) chamber. E.g. BOL chambers are the large chambers positioned in the outer layer of the barrel. Additionally, there are various special chambers, which name is not compliant with this scheme, that are placed in the regions with low coverage and in the transition region to aid muon track reconstruction there.

The size of the chamber types varies to a large extent. For the small inner barrel chambers (BIS), the length of the tubes is 1.7 m and a layer consists of 30 tubes, while for the outer endcap chambers (EOL) the length of a tube is up to 6.5 m and there can be 72 tubes per multilayer.

Operation principle

The MDT tube is an aluminium gas filled ($\mathrm{Ar} : \mathrm{CO}_2 = 93 : 7$) tube with a diameter of 30 mm and a wall thickness of 0.4 mm. The anode wire is a gold-plated tungstenrhenium wire with a diameter of 50 μm. It is positioned at the center of the tube with a 20 μm accuracy by the endplugs. The tube operates at a pressure of 3 bar and a voltage of 3080 V. The tube wall functions as the cathode. This working point and gas mixture is chosen for its good ageing properties and a relatively low gas gain (2×10^4) which reduces ageing.

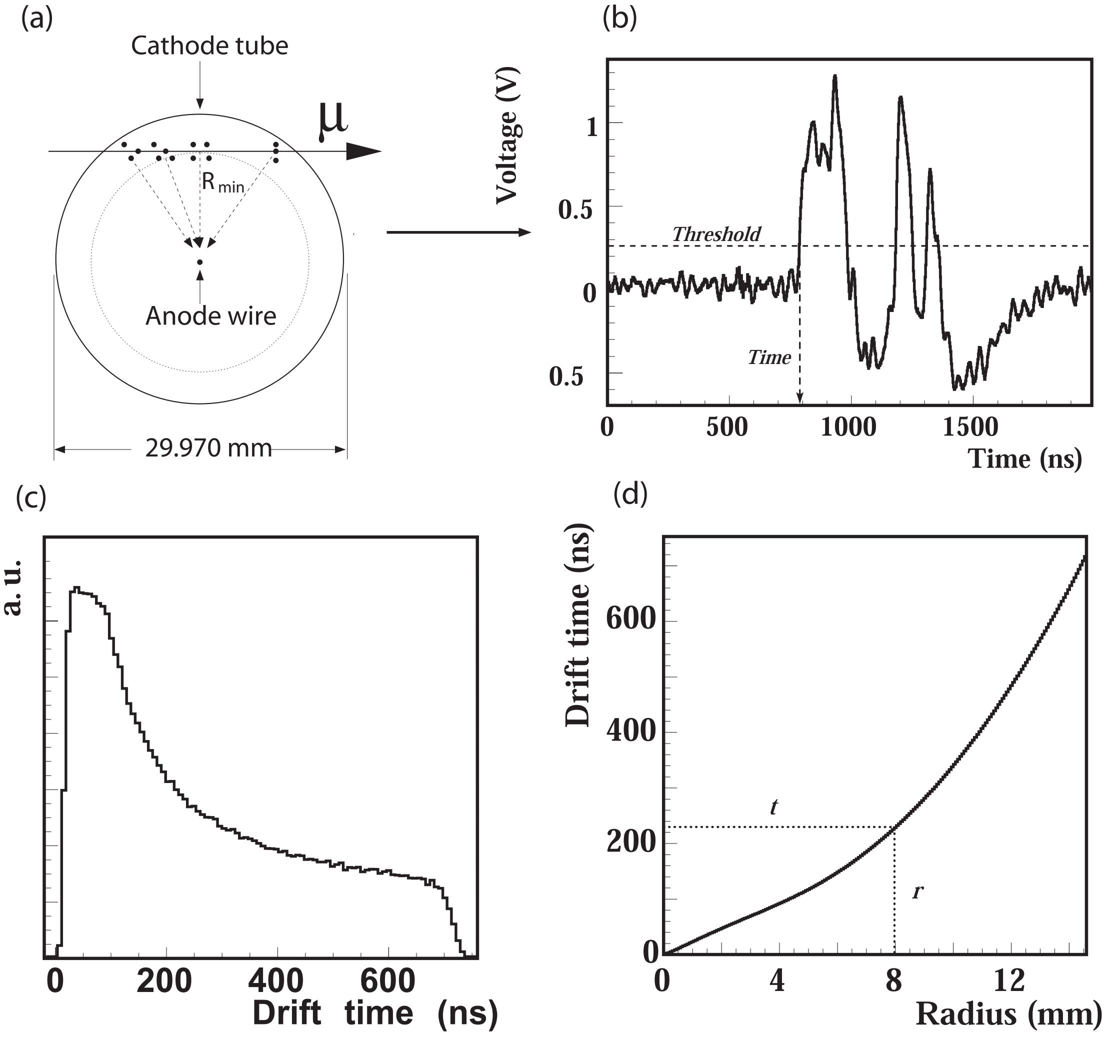

Figure 2.13: *Schematic overview of the operational principle of an MDT tube. (a) Schematic overview of the creation of charged clusters by a muon. (b) Measured signal pulse. (c) Typical drift time spectrum. (d) Typical rt-relation. Taken from [28].*

Figure 2.13, taken from [28], gives a schematic overview of the operation principle of an MDT tube. A charged particle crossing the tube will ionise several gas atoms. The created free electrons will drift towards the anode wire and create an avalanche of electrons and form clusters of electrons (a). As these clusters arrive at the wire, a small current will flow and a voltage drop is measured (b). When the predefined threshold is passed, the signal and the corresponding time is recorded. After correcting for various time offsets, a drift time spectrum (TDC spectrum) can be obtained by combining the times of a large number of crossings (c). The maximum drift time is about 700 ns. Assuming the tube is radiated homogeneously as a function of the drift radius, a relation between the recorded time and the closest distance of the particle to the wire can be obtained from this TDC spectrum (d). Note that this relation, the so-called *rt-relation*, is not linear, which can be deducted from the non-uniform shape of the TDC spectrum. The rt-relation is sensitive to several external conditions, e.g. the temperature, gas-mixture, B-field and high-voltage. To monitor these local conditions, each chamber is equipped with B-field sensors and temperature sensors. The magnetic field is measured with a precision of a few mT and a resolution of the rt-relation of 20 μm can be achieved after calibration [29].

An MDT measurement gives, instead of a precise position, a radius around the wire to which the particle has crossed perpendicular, as shown in figure 2.13. Such a measurement is called the *drift circle* and with a proper calibration a resolution of 80 μm on the radius can be achieved [30].

To prevent noise measurements by afterpulsing and to mask multiple measurements from the same particle, a dead time of 750 ns, or 30 bunch crossings, has been chosen.

MDT alignment

The MDT chambers are installed with a precision of about 5 mm and 2 mrad with respect to their nominal position. To achieve the required momentum resolution, the positions of the chambers need to be known to a precision smaller than 30 μm. ATLAS has two different strategies to determine the positions.

A system of optical alignment sensors, RASNIKs [31], is deployed to determine the positions and deformations of the MDT chambers. The RASNIK system consists of three active elements: a LED, a lens and a CCD camera. The LED projects a coded mask via the lens onto the CCD camera. The system monitors the relative displacements of the three elements. Figure 2.12 shows the *inplane* RASNIK system, which determines the deformations of the individual chambers. The intrinsic precision of the RASNIK system is about 1 μm.

In addition to the inplane system, a network of RASNIKs interconnects the MDT chambers with several optical lines, see figure 2.14. It has been shown that the required absolute position resolution of 30 μm can be achieved with this system [32]. The system also monitors relative movements of the MDT chambers with an accuracy of a few micrometers.

For the second strategy, (straight, high p_T) muon tracks will be used to align the chambers [33]. This is essential, since a few chambers are not optically linked to the RASNIK system and some positions can not be determined with the required precision. Short periods of running without toroidal magnetic field are foreseen to independently test the RASNIK system.

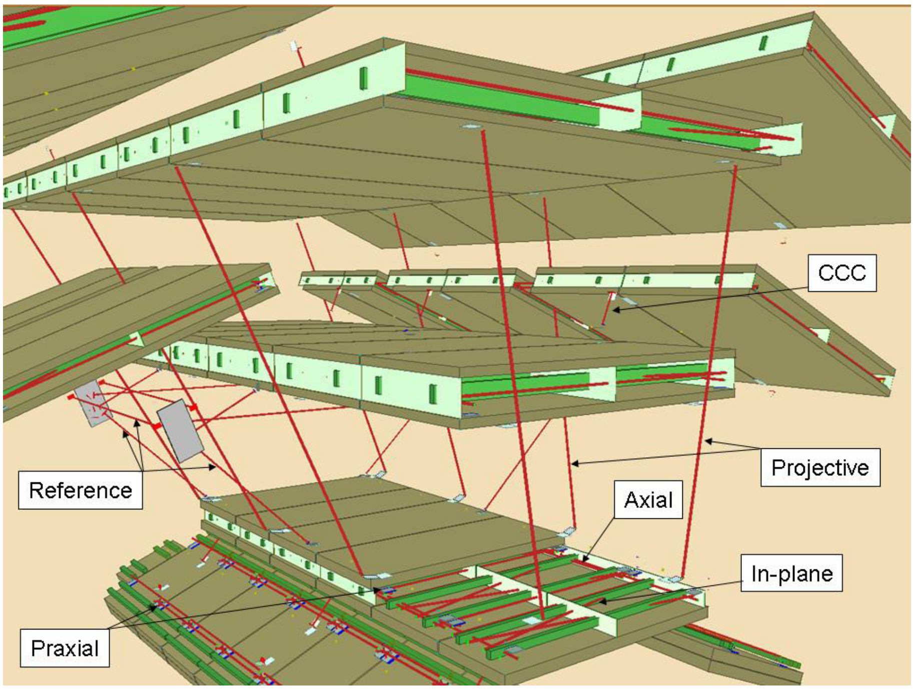

Figure 2.14: *Layout of the optical alignment lines for three adjacent barrel sectors. A network of optical alignment sensors, RASNIKs, determines the positions and deformations of the MDT chambers. The Chamber-to-Chamber Connector sensors (CCC) connect chambers in a small sector to those in an adjacent large sector.*

2.4 Muon reconstruction performance

To study the performance of the muon spectrometer, LHC collisions have been simulated using a detailed geometry description and profound knowledge of the detector responses.

As shown in section 2.2, muons with a momentum higher than 6 GeV are triggered. However, muons with a lower momentum can still be reconstructed in the muon spectrometer, where muons are identified and measured with momenta ranging from 3 GeV to 3 TeV (momenta in IP). In ATLAS, three strategies of muon reconstruction are used:

- **Standalone:** Muon track reconstruction using solely muon spectrometer data. The standalone reconstruction strategy will be covered in detail in the chapters 3 and 4;

- **Combined:** Matching the standalone muon tracks with the inner detector tracks and possibly calorimeter measurements. The inner detector track will improve the momentum resolution for muons with momenta below 100 GeV and reduce the fake rates of the standalone reconstruction;

- **Segment Tag:** Combining inner detector tracks with inner layer muon station measurements. This strategy will provide information in detector regions where standalone reconstruction is degraded, such as the region near $\eta = 0$ and the transition region. Also low energy muons not reaching the middle and outer stations, can be recovered.

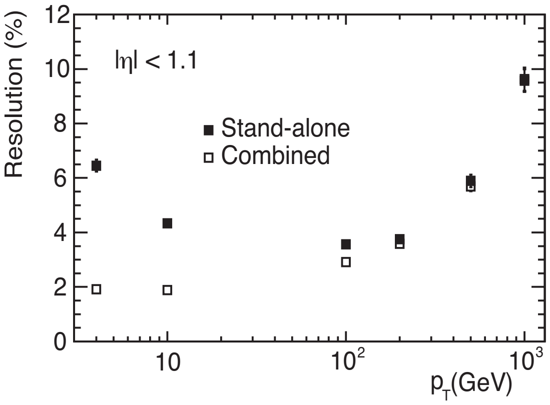

Figure 2.15: *Expected standalone and combined fractional momentum resolution as a function of* p_T *for single muons with* $|\eta| < 1.1$.

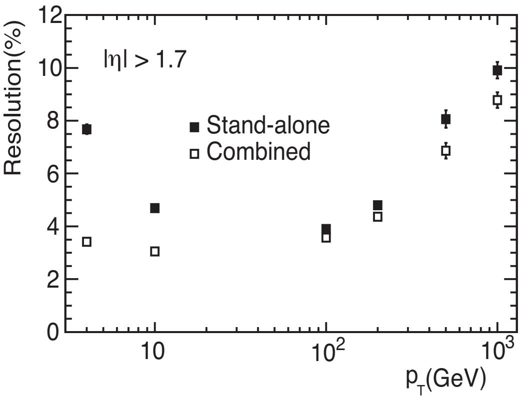

Figure 2.16: *Expected standalone and combined fractional momentum resolution as a function of* p_T *for single muons with* $|\eta| > 1.7$.

In figures 2.15 and 2.16 the expected transverse momentum resolution is shown on simulated data as a function of p_T for standalone and combined reconstruction for the barrel and the endcap. The standalone distribution has a similar shape as in figure 2.4. The optimal resolution of 3-4% is achieved for momenta around 100 GeV, while at higher momenta it is limited by the MDT tube resolution of about 80 μm. At lower momenta the resolution is dominated by energy loss fluctuations in the calorimeters. For these momenta the combined reconstruction improves the resolution as these fluctuations are not present in the inner detector measurements, which in turn are limited by multiple scattering. For higher momenta, the inner detector's lever arm is insufficient to compete with the muon spectrometer.

Figure 2.17 shows the reconstruction efficiency for muons with a p_T of 100 GeV as a function of $|\eta|$ for the three reconstruction strategies. The efficiency is defined as the fraction of muons which are reconstructed within a cone around the simulated muon of size $\Delta R = 0.2$, where ΔR is defined as:

$$\Delta R = \sqrt{\Delta\eta^2 + \Delta\phi^2} \tag{2.2}$$

In general the efficiency is very high, close to 100%, however a few regions show degradation. The reconstruction has a low efficiency near the $\eta = 0$ region, where the detector coverage is smaller due to the gap for services to the inner detector and calorimeter. The standalone reconstruction also has a lower efficiency around $\eta = 1.2$ which corresponds to the difficult transition region between barrel and endcap. The segment tag strategy almost fully recovers this loss, as the inner detector efficiency is high in the barrel and in

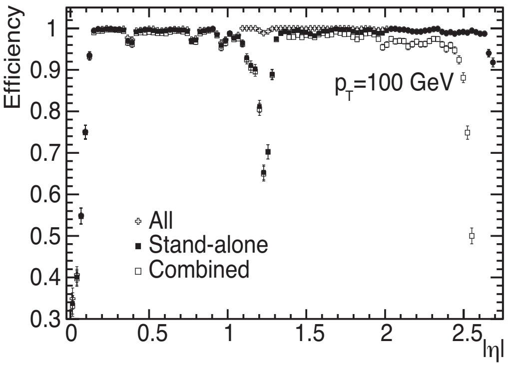

Figure 2.17: *Efficiency for reconstructing muons with $p_T = 100$ GeV as a function of $|\eta|$. The results are shown for standalone reconstruction, combined reconstruction and for the combination of these with the segment tags.*

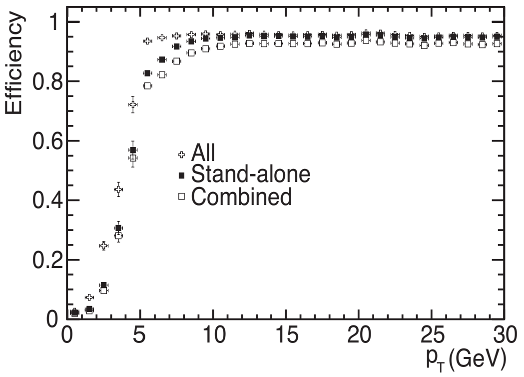

Figure 2.18: *Efficiency for reconstructing muons as a function of p_T. The results are shown for standalone reconstruction, combined reconstruction and for the combination of these with the segment tags.*

the endcap up to $|\eta| = 2.0$, after which the number of measurements decreases. Figure 2.18 shows that the segment tag strategy also contributes significantly for transverse momenta below 10 GeV.

2.5 Conclusions

This chapter describes the physics motivation for building the muon spectrometer. Its design is driven by the physics studies that will be performed at ATLAS. First of all, the spectrometer will provide a standalone muon trigger for muons with a momentum larger than 6 GeV. The important properties of a muon that need to be determined are its charge and momentum. With the chosen design a momentum resolution of 10% can be reached for momenta of 1 TeV and charge identification is possible for the most energetic muons. This corresponds to a sagitta measurement of 50 μm.

The trigger and the required precision is achieved by deploying four detector technologies, which have been described with a particular focus on their operation principles and geometry. The Monitored Drift Tube chambers have been covered in more detail as these are most important for the muon track reconstruction, which will be one of the main topics of this thesis. The alignment system has been described and a required precision of 30 μm can be reached.

The expected performance of the muon spectrometer has been studied briefly and will be covered more extensively in the forthcoming chapters.

Chapter 3

Pattern recognition

The purpose of the muon spectrometer is to find muons and reconstruct their properties, like their momentum, charge and direction, as accurate as possible. After decoding of the raw data, calibration and alignment corrections, the reconstruction is performed in three distinct steps, as shown in figure 3.1:

- **Pattern Finding:** The first step is the pattern recognition step. In this step sets of hits are sought that originated from the same particle. These sets of hits are called *patterns*. This step can be performed either locally, i.e. with hits per detector unit (chamber), or globally, i.e. with all hits at the same time. In this step also the first crude estimates of the parameters of the muon track are calculated. The typical precision on the angle is 100 mrad;
- **Segment Making:** In the second step the patterns are sorted per station. Due to the geometry of the muon spectrometer a muon typically traverses three stations (inner, middle, outer), see also chapter 2. The hits belonging to the same station are then fitted. These fitted short straight tracks are called *segments*. The typical

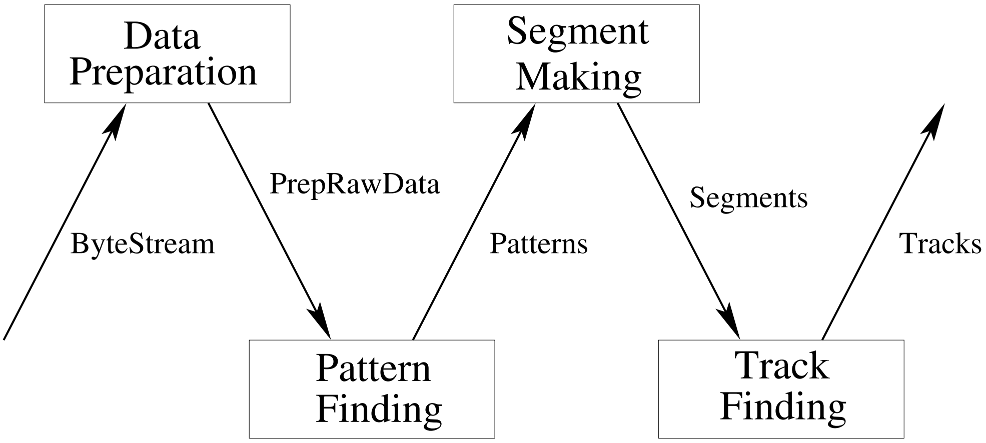

Figure 3.1: *Schematic overview of the data flow during reconstruction.*

precision on the angle is 2 mrad [28];

- **Track Finding:** The third step (re)combines the segments and adds additional ϕ measurements. These combinations, called *track candidates*, are then fitted. The *tracks* will have the best possible information on the properties of the original muon.

This chapter will describe methods, based on the Hough transform, for finding patterns (first step) in the ATLAS Detector. The other two steps will be described in chapter 4. For LHC running, the shape of the magnetic field and the fact that the tracks originate from the interaction point (IP) will be used. For the analysis of cosmic ray muons a dedicated pattern recognition method without IP constraint and magnetic field is described.

The pattern recognition is performed in two separate steps. Once for the bending plane (rz, corresponding with θ) and once for the non-bending plane (xy, corresponding with ϕ). The patterns are called *η-patterns* and *ϕ-patterns* respectively. Finally, these are combined into a 3-dimensional *combined pattern.*

3.1 Introduction to Hough transforms

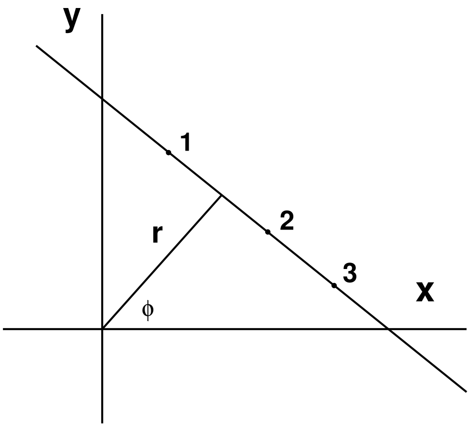

Figure 3.2: *Normal form of a 2d line.*

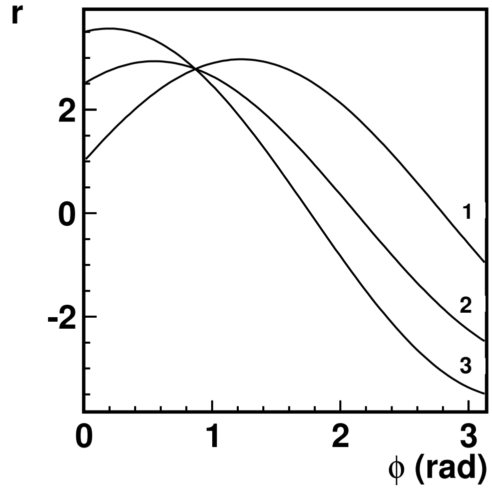

Figure 3.3: *The representation of the points 1, 2 and 3 of figure 3.2 in Hough space. The three curves intersect in the point that corresponds to the original 2d line.*

The Hough transform is a robust technique for identifying multidimensional shapes and patterns and estimating their parameters. It is widely used in digital image analysis

[34] and astronomical data analysis [35]. In 1962 Paul Hough developed this transform to analyse bubble chamber pictures at CERN, and it was later patented by IBM [36], [37].

The simplest and the original case of a Hough transform is the linear transform for finding lines in a 2d space. A 2d line can be described by its normal form:

$$x \cos \phi + y \sin \phi = r \tag{3.1}$$

This specifies a line that is perpendicular to the line drawn from the origin to (r, ϕ) in polar coordinates, as can be seen in figure 3.2.

On the other hand, for every point (x, y), equation (3.1) describes a curve in (r, ϕ) space, as can be seen in figure 3.3, where the curve is drawn for the points 1, 2 and 3. (r, ϕ) is usually called *Hough space*. The three curves intersect in the point that corresponds to the original 2d line. Thus finding this intersection point will find the line, which connects the 3 points.

Not only lines, but any trajectory could be found with a proper transformation, e.g. with $(x - x_0)^2 + (y - y_0)^2 = r^2$, 2d circles with centre (x_0, y_0) and radius r can be found. Generalising, a Hough transform is a function f_H that transforms points in $\mathbb{R}^n$ into some function space H:

$$f_H : \mathbb{R}^n \to H \tag{3.2}$$

To find patterns, the intersection points of the curves in Hough space need to be calculated. To do this analytically or numerically is rather cumbersome and hence cpu-intensive.

However, one of the main advantages of the Hough transform compared to other techniques is that the time is linear with respect to the number of points, $O(\mathrm{n})$, whereas a combinatoric approach would be of $O(\mathrm{n}^3)$. As within ATLAS, events can have up to 20,000 hits in the muon spectrometer, this property is extremely useful.

3.1.1 Binning

In practice the search for the intersection points is solved by binning the Hough space. For illustration, in figure 3.4 a set of points is transformed to Hough space. The points lying on the same line (black and grey points) give clear intersections in the Hough space, while some random points (open circles) show up as uncorrelated curves (dashed curves). Binning this Hough space will produce the *Hough histogram*, which is shown in figure 3.5. This binning has two advantages, first it is not necessary to calculate and evaluate the sometimes complicated analytical function f_H, but a numerical scan can be performed on all but one of the dimensions of H. Since in the used transforms H usually has dimension 2, this means a 1-D scan of one parameter, which should be fast. The second advantage is that instead of calculating the intersection points, only the maxima in the Hough histogram need to be found. The intersections of figure 3.4 are corresponding to the maxima of the histogram in figure 3.5.

The bin sizes correspond directly to the precision of the parameters of the patterns and therefore, have to be chosen carefully. Too large bin sizes degrade the precision

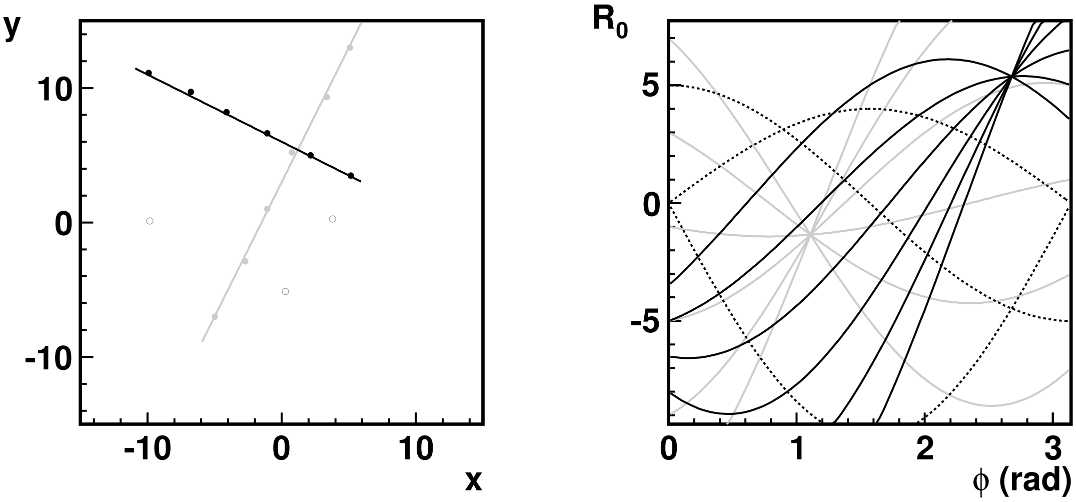

Figure 3.4: *Set of points (left) and their representation in the Hough-space (right).*

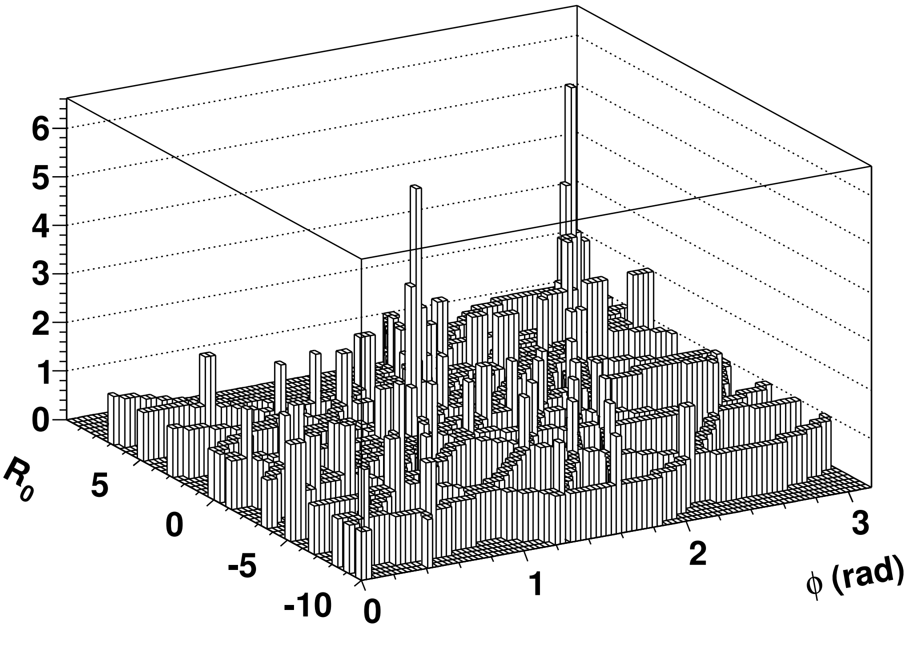

Figure 3.5: *Representation points of figure 3.4 in binned Hough space.*

and the ability of the transform to split two patterns close to each other, while too small bins will smear the peak in Hough space over several bins, which will degrade the pattern finding efficiency. Furthermore, bin sizes on both axis should ideally have the same precision, so that it is indifferent on which axis the 1-D scan is performed.

3.1.2 Sectors

In the ATLAS muon spectrometer background from different sources, such as cosmic ray muons, shower muons, punch-through, cavern background and pile-up (hits from particles originating in different bunch crossings than the triggered one) will be present, in particular when the LHC is running at high luminosity. This will make the search for the right maxima in the 2D Hough histogram hard. To increase the differentiable capability, a very crude granularity in the third, non-precision plane is introduced for many of the Hough transforms described in the rest of this chapter. This, de facto, means a couple of duplications (order 10), called *sectors*, of the Hough histogram. The sectors will follow the geometry of the muon spectrometer. The cpu time increase is limited as each hit is only contributing to one of the histograms.

3.1.3 Neighbouring bins

A pattern that has its maximum distributed over two bins, might not be found. To compensate for these kind of binning effects, besides filling only the original bins, some neighbouring bins are filled with a reduced weight as well. For cpu reasons only the bins diagonally to the original one are filled.

3.1.4 Association

After a maximum in Hough space is found, the parameters of the pattern, usually position and direction, are known, but the corresponding hits still need to be associated to the pattern. This is achieved by looping over all the hits, calculating their distance to the pattern and applying a distance cut.

In the following sections the several different Hough transforms, used in the muon reconstruction software are described in more detail.

3.2 Global Hough transforms for cosmic ray muons

Cosmic ray muons are muons originating from interactions of cosmic particles, most likely protons, in the atmosphere of the earth. Although muons only have a lifetime of 2.2 μs, due to their relativistic speed these muons often reach the surface of the earth. In high energy experiments these muons are used to commission and calibrate the detector prior to the beam-beam collisions. This is also done in ATLAS and since 2005, triggering on these cosmic ray muons, data has been taken. In principle these muons come from all directions (although mostly from above), contrary to the muons originating in LHC-collisions, which come from the interaction point. Another difference is that usually the cosmic ray data is recorded without the magnetic field, so that the trajectories of these cosmic ray muons are straight.

For cosmic ray data analysis, robustness of the algorithms is crucial as in the commissioning phase not all chambers are read-out, and misalignment and miscalibration is present.

3.2.1 r-ϕ transform

The r-ϕ transform is very similar to the basic Hough transform as given in equation (3.1) (and is repeated here as a reminder):

$$x \cos\phi + y \sin\phi = r_0 \tag{3.3}$$

Here, ϕ is the angle with respect to the x-axis and r_0 is the perigee, the signed distance to the IP, often called d_0 in 3d-helix representation. Since the cosmic ray muons cross the whole detector, continuous straight lines (no half-lines) are sought. For ATLAS, $\phi \in [0, 180]$ (°) and $r \in [-15000, 15000]$ (mm). The Hough space (r, ϕ) is divided in bins of 150 mm × 1°. To fill the Hough histogram, the set of hits (x_i, y_i) are transformed to Hough space for each ϕ bin according to:

$$r_{0,i}(x_i, y_i, \phi) = x_i \cos\phi + y_i \sin\phi \tag{3.4}$$

Note that it is equally valid to do the scan over r_0, and this would have resulted in the same Hough histogram and the same peaks up to small fluctuations. But since the muons are uniformly distributed over ϕ and not specifically over r_0, this method is more robust.

The distance D to the maximum $(r_{0,max}, \phi_{max})$ is calculated for every hit (x_i, y_i) with:

$$D = -r_{0,max} + x_i \sin\phi_{max} - y_i \cos\phi_{max} \tag{3.5}$$

The applied criterion for a hit to be associated is:

$$D < 500 \text{ mm} \tag{3.6}$$

3.2.2 Rz-θ transform

The Rz-θ transform for cosmic ray muons is similar to the basic Hough transform, but instead of the polar coordinate system, the cylindrical coordinate system is used. In the Rz frame R is strictly positive, and usually defined as:

$$R = \sqrt{x^2 + y^2} \tag{3.7}$$

A straight track through the muon detector looks like a hyperbola in the Rz frame and can be split into two separate straight lines, as can be seen in figure 3.6.

To overcome this splitting a sign to R is introduced. To sign R several assumptions for the value of the angle ϕ of the track, ϕ_{sec} are tested. This results in duplications of Rz space and can be seen as a third dimension in Hough space. Now instead of R as defined in (3.7), the new signed $R_{sec,i}$ is introduced:

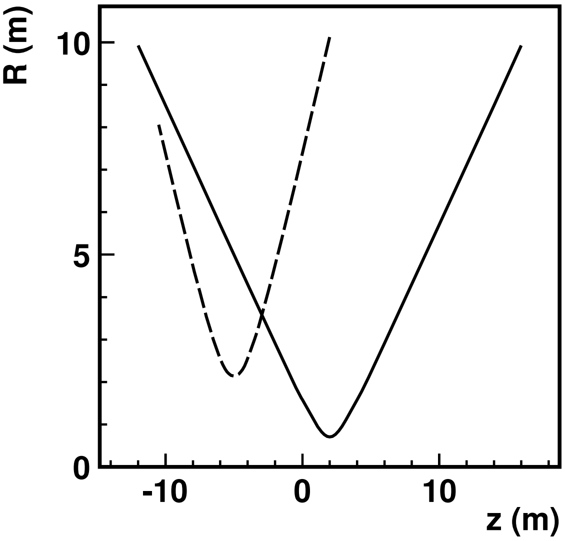

Figure 3.6: *Example of two three-dimensional lines ($x = 1 + t$; $y = 2 + t$; $z = 5 + 2t$ (solid) and $x = 1.5 - t$; $y = 1.5 + t$; $z = -5 - t$ (dashed)) in the cylinder coordinates Rz. A 3d-line can approximately be described by two straight lines in Rz.*

$$R_{sec,i} = x_i \cos\phi_{sec} + y_i \sin\phi_{sec} \tag{3.8}$$

with ϕ_{sec} defined as the assumed ϕ angle of the muon. The range of ϕ_{sec} is [180,360] (°), which corresponds to the fact that the muons enter the ATLAS cavern from above. $R_{sec,i}$ can be seen as the inproduct of the position (x_i, y_i) and the assumed direction of the muon $(\cos\phi_{sec}, \sin\phi_{sec})$. This gives for the transform (compare (3.4)), sign of $R_{sec,i}$ chosen arbitrarily:

$$Rz_{0,i}(x_i, y_i, z_i, \phi_{sec}, \theta) = -R_{sec,i} \cos\theta + z_i \sin\theta \tag{3.9}$$

For ATLAS, $Rz_0 \in [-27750, 27750]$ (mm) and $\theta \in [0, 180]$ (°). The Hough space (Rz_0,θ,ϕ_{sec}) is divided in bins of 150 mm × 2° × 15°. The 2D-scan is performed over θ and ϕ_{sec}. So for each sector a different Hough transform is performed. Equations (3.5) and (3.6) are again used for hit association.

3.3 Global Hough transforms for curved tracks

For beam-beam collisions, the muons will originate from the interaction point. However since the magnets will be on, the muons will be curved by the magnetic field. The magnets in the ATLAS muon spectrometer are designed such that the particles will only be bent in the Rz plane and not in the $r\phi$ plane. Thus the curvature or, better defined, the radius of the trajectory will be an additional degree of freedom for the η-patterns.

The radius ρ depends on the momentum p of the muon in the following way:

$$\rho \sim \frac{p}{qB} \tag{3.10}$$

where B is the magnetic field strength orthogonally to the Rz plane and q is the electric charge. As can be seen the radius is proportional to the momentum of the particle, thus the larger the momentum, the straighter the track.

3.3.1 r-ϕ transform

Since particle trajectories are not curved in the r-ϕ plane, and since the trajectories are coming from the IP, there is only one degree of freedom (ϕ). This gives some room to accommodate second order effects, like scattering and bending in r-ϕ by the inner detector magnets. To account for these effects, the basic Hough transform is used as described in section 3.1 with a short r axis, $r \in [-600, 600]$ (mm) and $\phi \in [0, 360]$ (°). The Hough space (r, ϕ) is binned in bins of 75 mm × 0.25°. For cpu reasons a scan over the short r axis is performed, where ϕ is calculated according to the formula similar to (3.4):

$$\phi_i(x_i, y_i, r_0) = \tan^{-1}\left(\frac{y_i}{x_i}\right) + \tan^{-1}\left(\frac{r_0}{\sqrt{x_i^2 + y_i^2 - r_0^2}}\right) \tag{3.11}$$

Note that the square root is always defined for the relatively small r_0 used in the transform. The Hough space is further divided into 12 θ sectors, thus covering 15° each.

3.3.2 Curved R-θ transform

So far, straight lines have sufficed, but for the R-θ plane a more complex track model is needed, shown schematically in figure 3.7. Up to the entrance of the spectrometer, trajectories are straight, while after that they are bent in the direction of the magnetic field according to (3.10). This bending is described as a parabola. For the outer endcap, the trajectory is again a straight line after the middle endcap chambers, as there is no magnetic field there. The magnetic field strength is assumed to be uniform.

The Hough space of this trackmodel is (θ_0, ρ), where θ_0 is the polar angle θ at the IP and the signed radius ρ, which is a measure for the energy of the particle. A positive ρ corresponds by convention with a positively charged particle.

Due to a linearisation in the angle θ, the track model is split in a barrel and an endcap part. So the trackmodel consists of four parts, a cylinder, a barrel, an inner endcap and an outer endcap part.

For the cylinder part, $R < R_{cyl} = 4$ m, $z < z_{cyl} = 6$ m, there holds:

$$R = z \tan\theta_0 \tag{3.12}$$

for each ρ. For the barrel part, $\frac{R}{z} > 11.43$ m (R) / 14 m (z):

$$z = \frac{R\cos\theta_0 + (R - R_{cyl})^2/\rho}{\sin\theta_0} \tag{3.13}$$

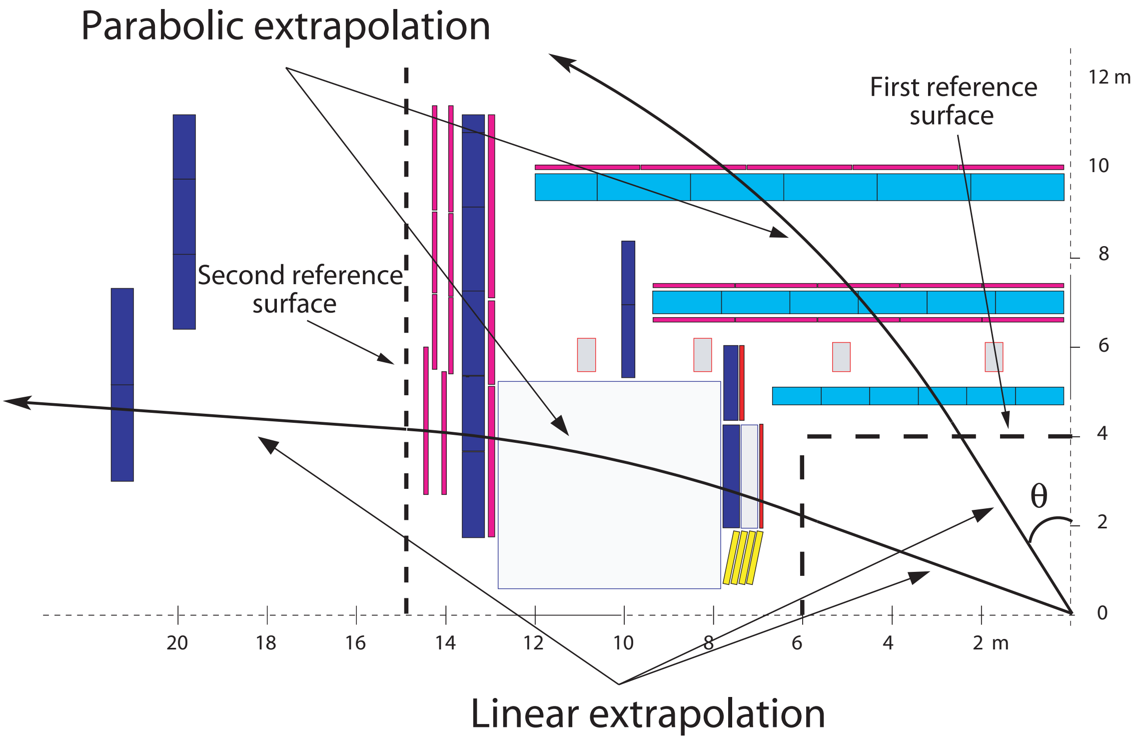

Figure 3.7: *Track extrapolation in the barrel and endcap regions. Up to the entrance of the spectrometer ($z = 6$ m, $r = 4$ m), trajectories are straight. In the barrel and the inner endcap part, $z < 15$ m, trajectories are curved. In the outer endcap part, $z > 15$ m, trajectories are straight.*

For the inner endcap part, $z_{cyl} < z < z_{end} = 15$ (m):

$$R = \frac{z \sin\theta_0 + (|z| - z_{cyl})^2/\rho}{\cos\theta_0} \tag{3.14}$$

And for the outer endcap part, $z > z_{end}$:

$$R = \frac{z \sin\theta_0 + \big((|z| - z_{cyl})^2 + 2(|z| - z_{end})(z_{end} - z_{cyl})\big)/\rho}{\cos\theta_0} \tag{3.15}$$

For each hit, θ_0 is calculated for several values of ρ. Out of the trackmodel equations (3.12)-(3.15), θ_0 can be calculated quickly for a given hit i (R_i, z_i) and ρ by the following equation:

$$\theta_{0,i} = \theta_i + \sin^{-1}(\frac{D_{mag,i}}{\rho}) \tag{3.16}$$

where $\theta_i = \tan^{-1}(R_i/z_i)$ and $D_{mag,i}$ is proportional to the distance a particle will experience the magnetic field to reach the position of hit i. The value of $D_{mag,i}$ is:

$$D_{mag,i} = \begin{cases} 0 & \text{, for cylinder hits} \\ (R_i - R_{cyl})^2/\sqrt{(R_i^2 + z_i^2)} & \text{, for barrel hits} \\ (|z_i| - z_{cyl})^2/\sqrt{(R_i^2 + z_i^2)} & \text{, for inner endcap hits} \\ (|z_i| - z_{cyl})^2 + 2\,(|z_i| - z_{end}) \quad (z_{end} - z_{cyl})/\sqrt{(R_i^2 + z_i^2)} & \\ & \text{, for outer endcap hits} \end{cases} \tag{3.17}$$

For large $D_{mag,i}/\rho$ ratios, unwanted peaks appear in the Hough histogram for the endcap region. To suppress this effect, the maximum allowed ratio is set to 0.5, which corresponds to a bend of 45°.

Binning

Since the trackmodel is not linear, a scan is performed over predefined non-linear values of the radius ρ, for which the resulting θ_0 is uniform. ρ is split in 160 bins with the, both positive and negative, values of ρ between 2,800 and 800,000 mm. A radius of 2,800 mm corresponds to a momentum of 2 GeV and a bend of up to 45°. In the Hough histogram the maximum positive and negative values of ρ are next to each other as the corresponding tracks resemble each other, both are nearly straight. $\theta_0 \in [0, 180]$ (°) is binned in bins of 0.5°. The transform is further split up in 16 ϕ sectors, covering 22.5° each.

Association

The distance D between the found maximum $(\theta_{0,max}, \rho_{max})$ and the hit (r_i, z_i) is simply calculated by the trackmodel equations (3.12)-(3.15) as the difference between the left- and righthandside.

Since the curved track model is an approximation of the trajectory of the muons, distance association need to be loosened for outer layer hits. A scale factor is introduced to soften the distance cut if the hit is farther away from the IP. A hit is associated if:

$$D < 500 s_i \text{ mm} \tag{3.18}$$

where s_i is the scale factor of hit h_i and is defined as:

$$s_i = \begin{cases} 1 & , |\vec{h_i}| < 5000 \text{ mm} \\ |\vec{h_i}|/5000 & , 5000 < |\vec{h_i}| < 15000 \text{ mm} \\ 3 & , |\vec{h_i}| > 15000 \text{ mm} \end{cases} \tag{3.19}$$

3.4 Background suppression

Hough transforms are in general very good in finding patterns in a high level background environment due to the fact that the background will be smeared out uniformly over the whole Hough space, while the pattern will be peaking. However in high-level background environments such as the ATLAS muon spectrometer this might not be enough and by applying weights to the filling of the histograms, background hits can be suppressed, while the peak of the pattern is unchanged. This is achieved in several ways and usually involves knowledge of the detector. Note that all hits can be associated to a pattern, even those with a zero weight.

3.4.1 Preferences for certain patterns

Often patterns with certain properties are preferred over others. From a physics point of view, high p_T muons are preferred as they are more likely to be coming from interesting physics, than low p_T muons, that can be coming from secondary particles or background. However, curved trajectories cross more detector layers. Thus without weighting, these trajectories will have a larger probability to be elected. These considerations are especially valid for large background levels where fakes are more likely to occur. To compensate for this effect, weights are downscaled with the following factor:

$$w_{curv} = \frac{1}{1 + w_{event}\Delta\theta} \tag{3.20}$$

where $\Delta\theta = \theta_0 - \theta$ is defined as in (3.16) and w_{event} as:

$$w_{event} = 20\sqrt{\frac{n_{hits}}{7000}} \tag{3.21}$$

where n_{hits} is the number of hits filled in the Hough transform. So straight patterns are preferred and the larger the event, the larger the preference.

For cosmic ray muons a similar weighting is applied, preferring patterns coming from the cavern entrance.

3.4.2 Downweighting noise

CSC

In the ATLAS software framework for the CSCs, there exists a standalone pattern recognition and segmentmaker, which is briefly described in section 2.3.1. Since these CSC-segments are reliable and very efficient, only CSC hits from these segments are taken into the pattern recognition. These hits get a weight factor of 2 (compared to normal hits which have a weight factor of 1).

Trigger chambers

For the trigger hits, see chapter 2.2, hit confirmation is asked, i.e. hits get a non-zero weight if there is another hit in a neighbouring strip, in either the same or a different layer (out of 8 for RPCs and 6 for TGCs). Besides this, in every trigger chamber there should be confirmed hits in at least 4 layers for RPCs (2 for TGCs) in order to get a non-zero weight. This will suppress random uncorrelated hits.

The weight that is applied is:

$$w = \frac{1}{0.75\sqrt{n_{layer}} + 0.25 n_{layer}} \tag{3.22}$$

where n_{layer} is the number of hits in the layer. This weight formula will downweight additional hits in a layer, but the sum weight will be more than that of an individual hit.

MDT

Since the MDT is a 'slow' detector, see chapter 2.3.2, this detector suffers most from background, in particular cavern background and to a lesser extent pile-up. First, all noise hits[1] and those that are out of time are discarded (not used for association). Secondly, hit confirmation is asked: two tubes close by should be hit as well. Non-confirmed hits get a zero weight. For chambers with confirmed hits a crude and fast segment search is performed on all non-isolated hits.

Furthermore, to downweight cavern background hits, trigger confirmation is asked, as background MDT hits have in general no coincidental trigger hits in the right time frame. Confirmed MDT hits obtain the following weight:

$$w = \frac{n_{rej} p}{1 + n_{rej} p} \tag{3.23}$$

where $n_{rej}p$ is the estimated background rejection factor. p is defined as:

$$p = \frac{1}{1.1 - w_{layer}} \tag{3.24}$$

where w_{layer} is defined as in (3.22). n_{rej} is dependent on the amount of confirmation. For trigger confirmed hits on a crude segment, n_{rej} is 30, for confirmed trigger hits not on a segment n_{rej} is 8, for non-confirmed trigger hits on a segment n_{rej} is $1.75/(\psi + 0.05)$, where ψ is the angle difference between the angle θ of the segment and the angle θ of the hit. This favours hits on a segment pointing to the IP.

For non-trigger confirmed hits not on a segment, their weight is defined as:

$$w = w_{layer} - 0.2 \tag{3.25}$$

These formulas make sure that all weights are between 0 and 1. And the weight represents superficially the probability that the hit is due to a true muon.

3.5 Implementation

In this section some of the technical details will be discussed.

---

[1] (Wilkinson) ADC value smaller than 50. The Wilkinson ADC value provides the measurement of the leading edge charge deposited on the MDT wire.

3.5.1 Multiple patterns

Per Hough histogram only the maximum is used. In principle more maxima could be used, but this turns out to give complications as sometimes nearly identical patterns are found twice, and thereby obscuring a second smaller pattern. However since for most Hough transforms described, the Hough space is split up in sectors whose histograms do not have any hits in common, several patterns can be constructed. In every two adjacent sectors maximally one pattern can be found and the maximum number is set to five.

If, after the patterns have been constructed, there are any remaining hits that are not associated to any constructed pattern, a next iteration will be performed until no more hits are remaining. The maximum number of iterations is five.

3.5.2 Reweighting and cpu speedup

To speed up the transforms hits with a weight smaller than 0.25 are not taken into the Hough transform, as they are not very likely to change the position of the maximum. For large events, for MDT hits a more stringent cut is imposed:

$$cut_{mdt} = 1 - \frac{5}{\sqrt{n_{mdt}}} \tag{3.26}$$

where n_{mdt} is the number of MDT hits in the event not yet associated to a pattern. If this cut is larger than 0.5 (or equivalent n_{mdt} is larger than 100), then the weights of the MDT hits are downweighted according to:

$$w_{new} = \frac{1 - cut_{mdt}}{1 - (5 - \frac{4}{w})cut_{mdt}} = \frac{w}{w + (\frac{4}{5}\sqrt{n_{mdt}} - 4)(1 - w)} \tag{3.27}$$

This function is plotted in figure 3.8 for several values of n_{mdt}. This allows that in the early iterations only MDT hits with a high weight are taken into account, while in later iterations hits with smaller weights are also used, as then n_{mdt} is smaller.

3.5.3 Pattern cleaning

When the patterns have been found a χ^2 fit is performed on the ϕ-patterns to determine the track parameters and remove outliers. Furthermore, when there is more than 80% of hit overlap between patterns, these patterns are merged and cleaned of outliers in the same way.

3.6 Combining

After the ϕ- and η-patterns have been found, they are combined. This is achieved by associating hits from a ϕ-pattern to an η-pattern and vice versa, based on their distance to a pattern, where the distance to a pattern is defined in the same way as for associating hits in the Hough transform, see equations (3.6) and (3.18).

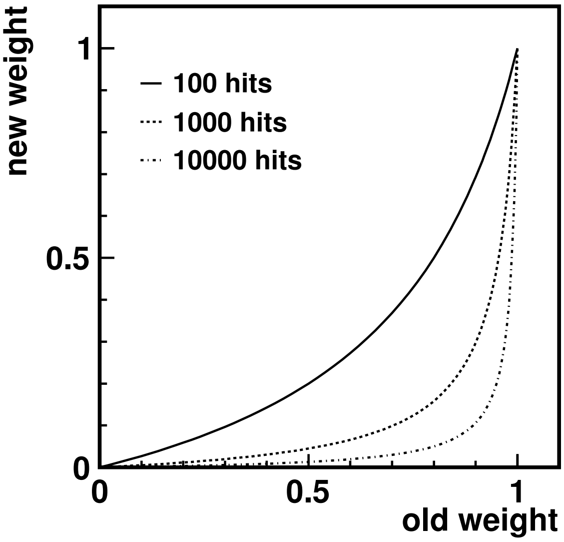

Figure 3.8: *Reweighting function for different values of MDT hits.*

A combination of an η- and ϕ-pattern is saved as a candidate when the following two conditions are fulfilled:

- at least one hit of the η-pattern is close to the ϕ-pattern (within half of its absolute length (to the IP));
- at least 25% of the hits of the ϕ-pattern are within 1.5 m of the η-pattern.

Note that these distance cuts need to be so open as the error on the position of hits in their non-precision plane can be quite large, till up to 3 m, for endcap MDT hits.

For cosmic ray muons, for every η-pattern only the best, i.e. smallest average distance, matched ϕ-pattern is saved as a candidate. Additionally for every η-pattern a ϕ-pattern is constructed of ϕ hits that are in the same gasgap as the trigger η hits of that η-pattern, for both RPC and TGC hits. If the, in this way constructed, ϕ-pattern is not a subset of another ϕ-pattern, the (η, ϕ) combination is saved as a candidate. Possible missed ϕ-patterns can be recovered in this way, notably those with only 1 or 2 hits. If no ϕ-pattern is found at all, the η-pattern is saved as a combined pattern, since segments can still be made and even full tracks might be constructed by inventing ϕ hits (see chapter 4).

For cosmic ray muons, at this stage candidates are split into two separate candidates when crossing the calorimeter[2]. As splitting point, the point closest to the IP is taken. At the combined refitting stage, tracks from both hemispheres can be recombined (see chapter 5 and 6). Candidates not crossing the calorimeter are not split and will be treated as one track throughout the reconstruction.

From every candidate a combined pattern is built with the following position and direction:

---

[2] defined as a cylinder with a radius of 4 m and a length of 12 m centered around the IP

$$pos = (x_\phi, y_\phi, z_{0,\eta} + \sqrt{x_\phi^2 + y_\phi^2}/\tan\theta_\eta) \tag{3.28}$$

$$dir = C(\cos\phi_\phi \sin\theta_\eta, \sin\phi_\phi \sin\theta_\eta, \cos\theta_\eta) \tag{3.29}$$

The index indicates if the value is taken from the η or ϕ-pattern. The position is the 3d-position closest to the IP in the R-ϕ plane. C is the radius, and is stored by convention as the magnitude of the direction. Afterwards the combined pattern is cleaned from outliers by the same two distance cuts that are also used for matching.

3.7 Conclusions

This chapter has given a general introduction to Hough transforms, the original method and its software implementations have been explained. The main advantages of Hough transforms are their robustness and their ability to deal with large volumes of information with high levels of background, which makes them suitable for usage in the ATLAS muon spectrometer.

For the ATLAS muon spectrometer several dedicated transforms for cosmic ray reconstruction and for LHC-collisions with and without a magnetic field have been developed. For the cosmics case, Hough transforms with a straight track model and without any vertex constraint have been developed. For LHC-collisions, Hough transforms with a curved track model have been developed.

Several techniques to further reduce the background levels have been used. By using multiple histograms per transform and using weighted entries when filling the Hough histograms it has been shown that background levels can be dramatically reduced. Several different weighting methods using specific detector knowledge have been implemented to optimise the performance.

Patterns are always reconstructed in two steps, once in the R-ϕ plane for the ϕ hits and once in the R-θ plane for the η hits. These patterns are later combined into one three-dimensional pattern.

In the next chapter a performance study on the produced combined patterns will be performed.

Chapter 4

Modular reconstruction

In the previous chapter, the pattern finding step of the muon reconstruction has been described in detail.

For the next steps, the segment making and the track fitting, see figure 4.1, several complications arise that at the pattern recognition stage did not have to be taken into account, especially the structure of the detector layout is an important factor:

- **Long distances:** The muon spectrometer provides a small number (2-3) high precision measurements with large distances in between. These large distances result in extrapolation errors;

- **Inhomogeneous material distribution:** The amount of material passed by the trajectory is important to estimate correctly the momentum and scattering. Non-active parts like the toroids and the support structures make up the main part of the material in the muon spectrometer, which results in a very inhomogeneous material distribution. A detailed description of all material is important;

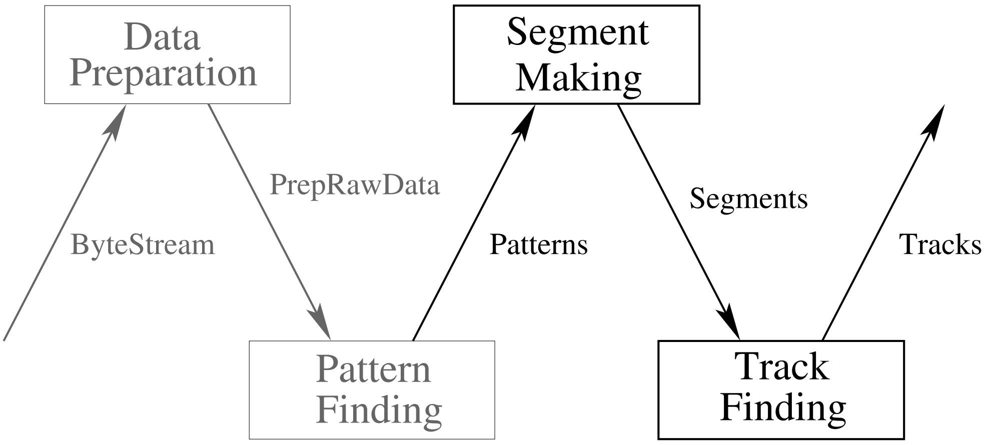

Figure 4.1: *Schematic overview of the data flow during reconstruction. In this chapter the segment making and the track finding will be covered.*

- **Inhomogeneous magnetic field:** The magnetic field of the magnets is, especially close to the coils, inhomogeneous. This increases the extrapolation errors and it is not possible to describe trajectories with an analytical trackmodel;
- **Few measurements in the non-bending plane:** There are only a few ϕ measurements in the trigger chambers, whereas due to the inhomogeneity of the magnetic field the ϕ coordinate has a large impact on the momentum.

This chapter will briefly cover the other steps, the segment making in section 4.2 and the track finding in 4.3. Furthermore, the general algorithmic structure and the (Muon) Event Data Model are described in section 4.1. Finally, some reconstruction results are presented in section 4.4.

4.1 ATHENA and the Muon Event Data Model

For large collaborations like the ATLAS experiment, common interfaces and data objects are a necessity to ensure easy maintenance and coherence of the experiment's software-platform over a long period of time. The ATLAS Event Data Model (EDM) improves commonality across the detector subsystems and subgroups, such as physics analysis groups. Furthermore, the EDM allows the use of common software between online data processing and offline reconstruction.

One example component of the ATLAS EDM is the common track class which is used for track reconstruction in the inner detectors, the muon detectors and for combined reconstruction. For the combined event reconstruction a common particle class is introduced which serves as the interface between event reconstruction and physics analysis. In this section, the ATLAS software framework, ATHENA, and the EDM parts that are used in muon reconstruction will be discussed.

4.1.1 ATHENA

The ATLAS software framework ATHENA [38] is derived from the GAUDI framework [39] developed for the LHCb experiment. It is based on the blackboard architectural model [40]. A blackboard system has 3 (major) components:

- The blackboard, a shared repository of problems, information, solutions etc. In ATHENA this is the Storegate Service, where all data objects used are stored during the event reconstruction;
- The algorithmic modules, each module reads the blackboard and provides a certain expertise (new data objects), which it writes to the blackboard. In ATHENA these modules are called *Algorithms*;
- The controller, which controls the flow of the problem-solving activity in the system. In ATHENA this is provided by the *ApplicationMgr*.

This model is very modular by nature and ATHENA follows this by making the clear distinction between data classes and algorithmic classes. Furthermore, common interfaces for both data objects and algorithms make the reconstruction process highly modular.

The Muon EDM is an extension of the generic detector-independent Tracking EDM [41], [42]. In the following sections several objects of the Muon EDM are discussed separately.

4.1.2 Muon Raw Data Object

The Muon Raw Data Object (RDO) is the class that contains all possible information measured directly by the specific detector technology, usually all the raw datawords coming from the specific channel are recorded in the RDO. For example an MDT RDO contains, on top of all the raw datawords connected to the channel, the channel id, the TDC time and the ADC value.

4.1.3 Muon PrepRawData

The Muon PrepRawData (PRD) objects [43] are the transient representation of the Muon RDO. Every detector technology has its own dedicated class, which inherits from the Tracking EDM base class *PrepRawData* [44]. The Muon PRD is constructed from the Muon RDOs for the strip detectors (CSC, RPC and TGC) by detector-specific clustering algorithms and for the drift tube detectors (MDT) by performing a crude calibration of the drift circles first.

Each technology has its own class as is shown in figure 4.2, which shows the complete PRD inheritance tree with the most important data members.

4.1.4 MuonPattern and MuonPatternCombination

Sets of PRDs that are produced by a pattern recognition algorithm, such as described in chapter 3, use *MuonPatterns* and *MuonPatternCombinations* [45]. A MuonPattern is a set of PRDs with a predicted direction and position. A MuonPatternCombination is more complex and has a set of so-called *MuonPatternChamberIntersects* [46]. These intersects are similar to MuonPatterns, except that they are designed to hold information of only 1 chamber or station. Besides the intersects, a MuonPatternCombination has a TrkParameters object that describes the trajectory.

In the reconstruction described here MuonPatternCombinations are used, since a global pattern recognition search is performed. However MuonPatterns are also used in ATHENA by algorithms that perform local pattern recognition searches.

4.1.5 Measurements on a track

For measurements that are linked to a track, a class different from the PRD is used. There are several reasons to introduce this object and thus allow the data object of the output of the initial pattern recognition to be different from the PRD:

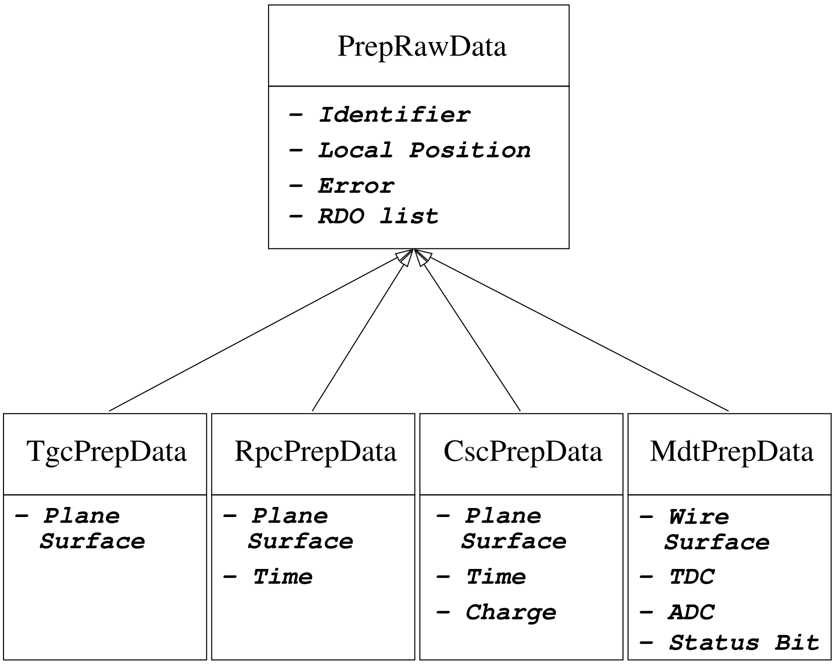

Figure 4.2: *Inheritance tree of the Muon PrepRawData.*

- By design the PRD objects are protected against modifications after they are constructed. The main reason for this is that subsequent algorithms will not create a bias by recalibrating the objects;
- Usually additional calibration is performed and it is allowed to be redone at a later stage when possibly more information is available;
- More complicated objects than clusters and drift circles could possibly be linked to a track, like a whole group of hits within a detector, or ambiguous hits that need to be resolved later.

The abstract common base class *MeasurementBase* [47] can handle these different kind of objects and holds the minimum amount of information so that it can be fitted by a track, which are up to five local parameters, an error matrix, a global position and a surface. The surface is used to transform between local and global coordinates.

In the Muon Reconstruction three types of measurements on a track are used: RIO On Track, Competing RIOs and Segments, see figure 4.3. They will be described separately.

RIO On Track

The object that resembles the PRD most and that represents the clusters and drift circles, is the 'Reconstructed Input Object on a Track' (*RIO_OnTrack* or short *ROT*) [48]. Like with the PRD object, there is a generic base class and technology-specific specialised classes.

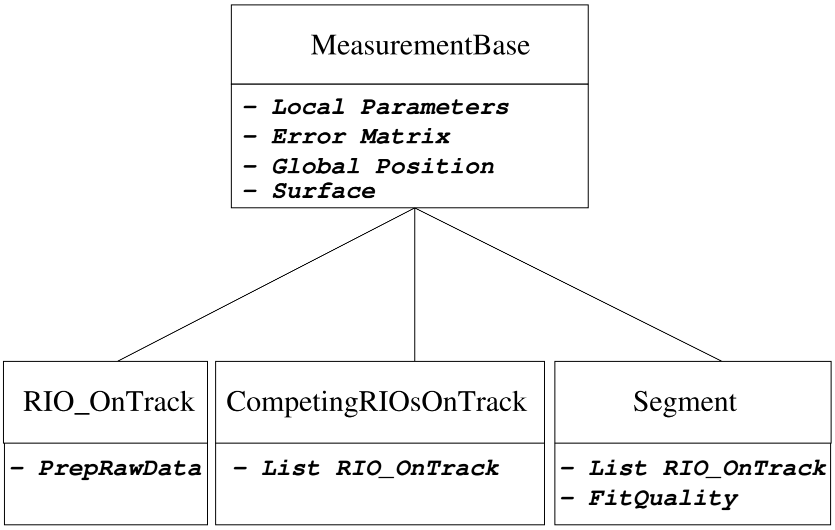

Figure 4.3: *Inheritance tree of the MeasurementBase classes.*

RIO_OnTracks hold, additionally to the MeasurementBase class, a link to the original PRD object. The class structure for the muon system is shown in figure 4.4. There is an additional distinction between drift circles (MDT) and point-like measurements (CSC, RPC, TGC). The objects are produced by special RIO_OnTrackCreator classes. Note again the splitting between on one side, algorithms and tools, and on the other side data objects.

Competing RIO On Track

A special class of ROTs are so-called *Competing ROTs*. These objects represent a group of hits, of which not necessarily all belong to the track. The individual hits have a certain probability assigned to them. In the muon spectrometer these objects are used for associating several strips in the trigger chambers to segments and tracks.

Segments

A *Segment* [49] is a set of ROTs that are locally fitted. It has again local and global parameters, an associated surface, and in addition a FitQuality object, which describes the quality of the fit. In standalone muon reconstruction segments primarily made of MDT ROTs or CSC ROTs are used. Additionally RPC and TGC ROTs and Competing ROTs are associated to the segments.

4.1.6 MuonSegmentCombination

The *MuonSegmentCombination* object [50] is the equivalent of the MuonPatternCombinations object that deals with ROTs. It is a set of MuonSegments that are grouped per station. In general the object originates from a single MuonPatternCombination. In the next sections these objects are referred as *combinations*.

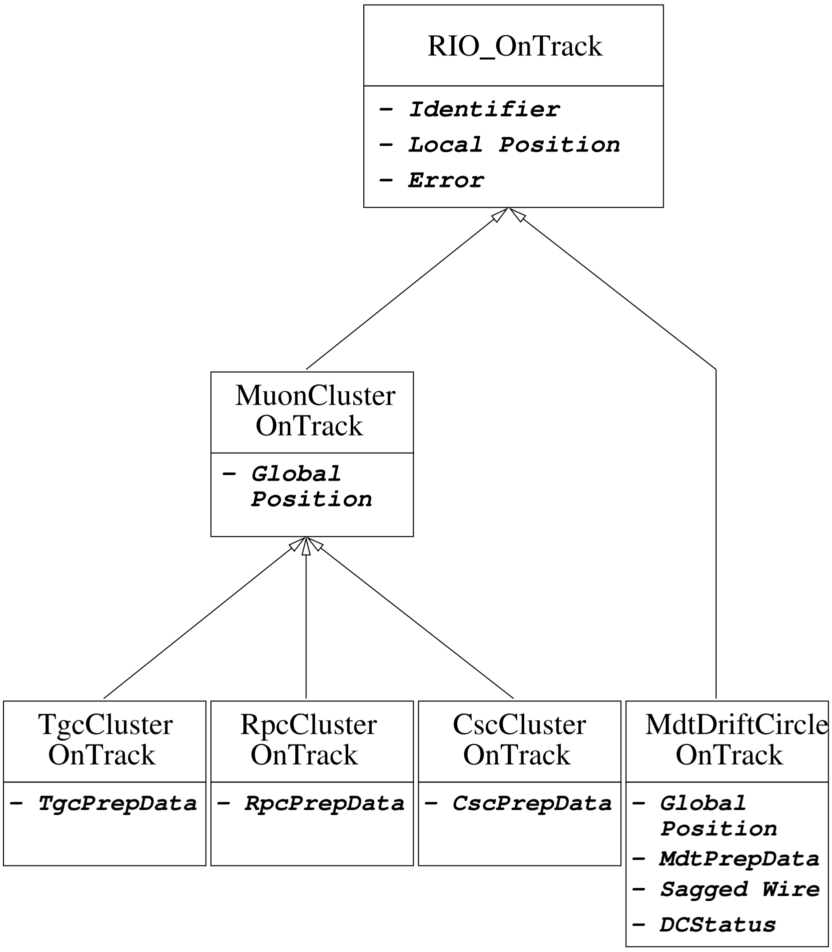

Figure 4.4: *Inheritance tree of the Muon RIO_OnTrack classes.*

4.1.7 Track

The *Track* class [51] is optimised for reconstruction purposes and not intended for usage in physics studies. It is designed to be both simple and have the possibility to contain all the information needed for and generated by the track fit. For a detailed description, see reference [41].

The information about the measurements on a track are stored in a collection of *TrackStateOnSurface* objects [52]. A TrackStateOnSurface is another flexible EDM object that has one or several of these objects:

- **A TrkParameters object** [53] that represents the track through a set of parameters such as space coordinates and the momentum at that point;
- **The MeasurementBase object(s) on that surface**, which can be one of the objects described in section 4.1.5;
- **The scattering angle**, which stores the change of direction and its error;

- **A type flag** that describes the nature of the information. It can be one of the following: measurement, scatter point, outlier, hole, perigee, brempoint or inert material.

4.2 Segment making

Now that the data model has been covered, the rest of the muon reconstruction can be described: first the segment making and then the track fitting.

After the patterns are found, the second step of figure 4.1 is performed, namely the segment making. The patterns, i.e. hits and a predicted position, provided by the pattern recognition are fitted locally per chamber.

Until now the description of the reconstruction has been general, describing the EDM and sketching the main philosophy, which is generic for every algorithm. However in the next sections, which will cover the algorithms in detail, this generality can no longer be maintained.

The algorithms that will be discussed below, are parts of MOORE (Muon Object Oriented REconstruction), which is a modular software package in ATHENA. It is a common name for several individual muon standalone reconstruction modules. Recently, almost all of the old MOORE modules [54] have been rewritten. The new algorithms will be covered here in detail.

In MOORE, the pattern recognition and the segment making are steered by a common algorithm. The following steps are distinguished:

- 2D CSC segment making;

- 4D CSC segment making;

- pattern finding;

- MDT segment making.

The first item produces segments for both η and ϕ hits in the CSC detector and the second item combines them. Note that this is very similar to the strategy of the patterns produced by item 3, which is described in chapter 3. Item 4 is the MDT segment making step, which takes the patterns as input and outputs segments.

A detailed diagram of the algorithmic flow of the segment making in MOORE is shown in figure 4.5. Note that this flow is a slight distinction from the simplified flow of figure 4.1.

For each of these steps one or more dedicated tools are written. Since each step is completely separated from the other ones, the tools could be interchanged with other tools that have identical functionality. In this chapter the current default MOORE tools are described.

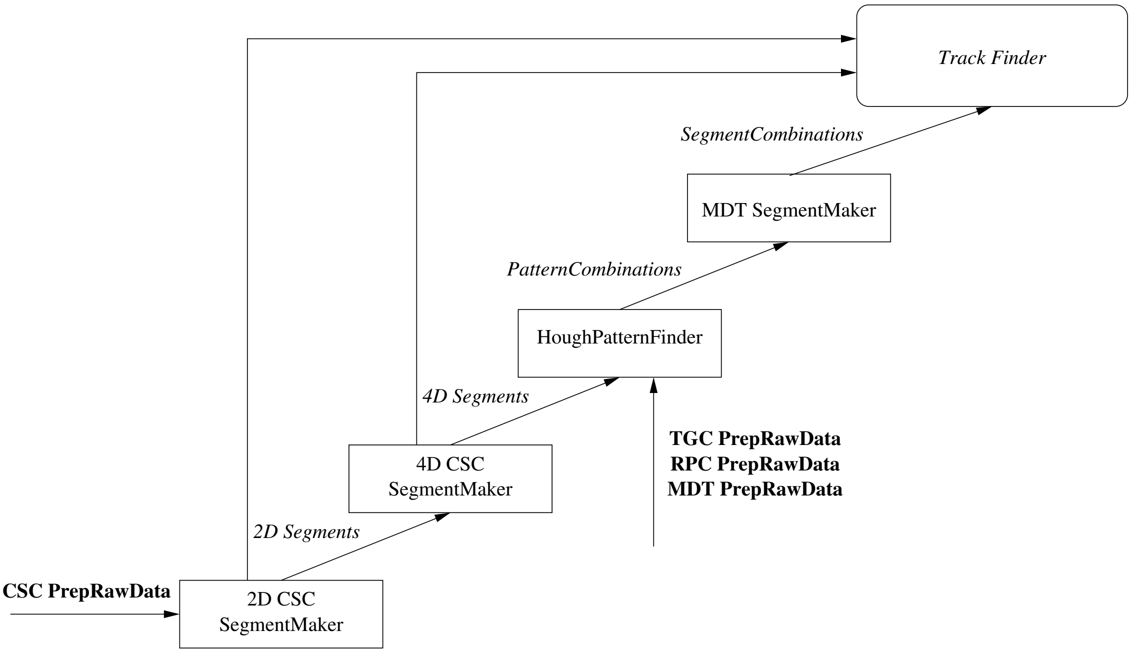

Figure 4.5: *Flow diagram of MOORE's segment making.*

4.2.1 CSC segment making

The CSC segment making [55], [56] is done in several steps. First a clusterization is performed by fitting the charge deposition on several strips. This gives a spatial resolution of 61.4 μm in η and 3.33 mm in ϕ. Note that the ϕ strips are non-pointing.

Then the ϕ and η clusters are fitted separately with a straight line fit without IP constraint. Seeding is achieved by a combinatorial approach and requiring a cluster from each layer (4 for both ϕ and η). These segments are called *2D Segments*. They have a two-dimensional local position and a one-dimensional direction. Finally all 2D Segments are combined to so-called *4D Segments*, which have a full three-dimensional position and direction.

The achieved resolution is 31.4 μm in Rz, 1.15 mrad in θ and 2.68 mm in $R\phi$, 33.0 mrad in ϕ. An efficiency of 99.8% has been reported on simulated data.

In general the 4D segments are used in the track finding, although in some cases the 2D η segments may also be used.

4.2.2 MDT segment making

The MDT segment maker used by MOORE is the DCMathSegmentMaker, which will be described below, but is covered in more detail in the thesis of reference [28]. Several other algorithms have been developed [57], [58], [54]. The DCMathSegmentMaker algorithm proved to be the best in terms of efficiency and fake rate, when the patterns from chapter 3 are given as seeds [28], [59]. The algorithm selects and fits MDT hits to find segments. Trigger hits are afterwards associated to the found segments.

The selection for hits is done as follows. From every multilayer a hit is taken and for the two drift circles the four possible tangent lines are taken as seed for fitting, see figure 4.6. Only the tangent lines within 0.2 rad of the pattern prediction and with sufficient hits within 1.5 mm of the tangent line are fitted with a χ^2 minimization of the distances to the drift circles. The minimum number of hits for a segment to be built is three.

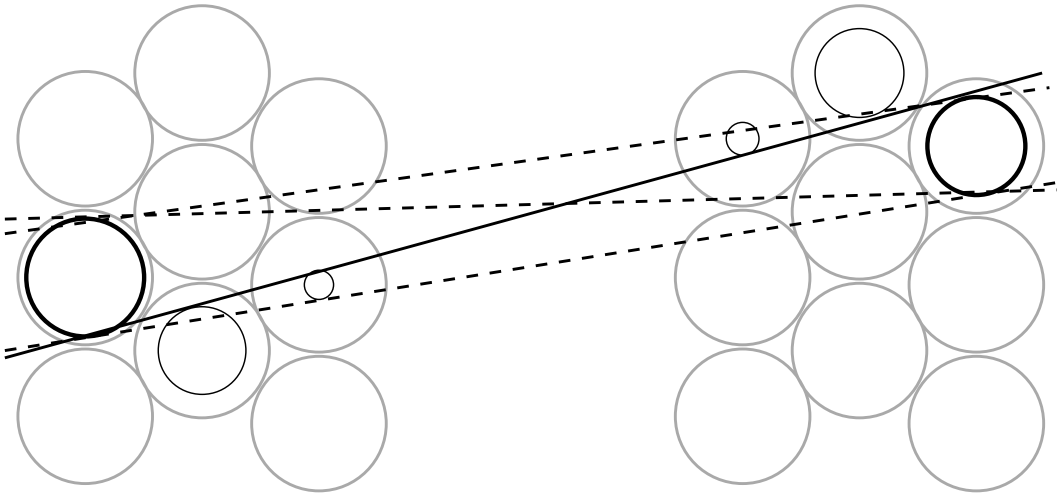

Figure 4.6: *Drift circle seeds with the four possible tangent lines. The black line is the correct seed.*

Hit dropping

It occurs that hits are associated wrongly to a segment, e.g. hits from δ-electrons (electrons knocked out of their atom by the muon). When a segment has a χ^2 per degree of freedom (dof) larger than 10, the hit with the largest χ^2 contribution is dropped and the segment is refitted, possibly associating new hits. The procedure is repeated until the χ^2 per dof drops below 10 or less than three hits remain. Wrong hit combinations are rejected by this procedure as well. Note that this procedure is not guaranteed to produce the optimal solution in all cases.

Segments covering more than one chamber

In some cases hits belonging to the same segment come from more than one station. This occurs in about 10% of the segments. Hits from neighbouring η stations are added before segment finding to fully reconstruct these segments. For neighbouring stations in ϕ, the ϕ angle of the segment is not known well enough to put the hits from these chamber in the same coordinate frame without introducing a large error.

Trigger hit association

After a segment has been found, trigger hits from the RPC or TGC stations in the vicinity of the MDT station are put on the segment. The barrel middle and outer

MDT stations share their station with an RPC chamber. Endcap MDT chambers have no physical connection to a trigger chamber. The TE4 and TF4 TGC chambers are linked to the inner endcap chambers and the other TGC chambers to the middle endcap chambers.

Segment quality and holes

To each segment a segment quality object is added, which contains information about the segment, such as the number of hits and the χ^2 of the fit. Also the number of missed hits is calculated by determining which tubes have an intersection with the segment, based on its local position and direction. Intersected tubes without a hit on the segment, and an expected radius less than 14.4 mm, are defined as missed. These missed hits are called *holes*. Holes might indicate a fake segment, but possible physical reasons for holes are dead tubes, δ-electrons that produce a drift circle with a smaller radius, or tubes masked by a noise hit or a muon from an earlier bunch crossing. Information about the dead and masked tubes is envisioned to be added in the reconstruction, but this is currently not available.

Segment selection

The set of segments found in a station might still contain ambiguities, i.e. segments sharing hits. To resolve those, the segments are sorted on quality criteria, which are in order of priority: number of hits, smallest number of holes, number of associated trigger hits. In case of ambiguities, the segment with a lower quality is discarded. In some rare cases when the quality is equal, both segments are kept and flagged as ambiguous and will be resolved in the track finding stage.

Segment performance

This section will cover some reconstruction results of the initial pattern recognition and segment making. It is meant to give an indication of the achieved segment performance. A more detailed performance study is performed in reference [28]. Results for the complete MOORE chain are discussed in section 4.4.

The reconstructed segments that have most hits in common with the hits of the simulated muon in that chamber, with a minimum of 80% of simulated hits, are flagged as *matched*, the others are flagged as *fake*. Since fake rates are very dependent on the simulation, fake rates are not discussed here, but are discussed in detail in reference [28].

The following plots show several distributions to demonstrate the reconstruction features for MOORE for $Z^0 \rightarrow \mu\mu$ events. For a detailed description of the simulation, see also section 4.4.

Figure 4.7 shows the number of stations that are traversed by the simulated muon and have hits in at least 3 tubes. This plot reflects the design of the muon spectrometer. Conform the muon spectrometer design most muons cross 3 stations. Due to stations overlaps in ϕ and η, the number of crossed stations can be much larger. The number of traversed stations is degraded around $\eta = 0$ and $\eta = \pm\ 1.2$. Another degraded region,

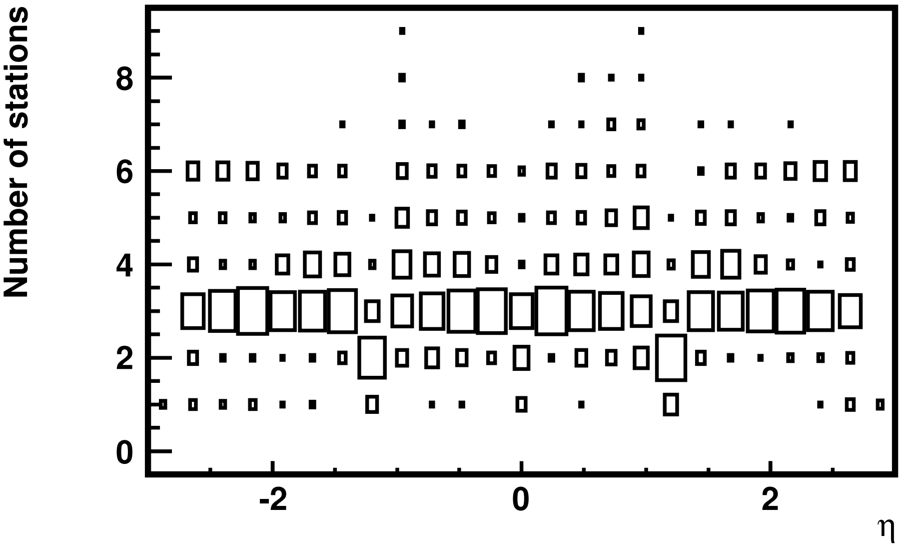

Figure 4.7: *Number of stations with at least three tubes hit by a simulated muon as function of η.*

not observed in this plot, are the feet of the detector around $\phi = \pm 22.5°$. 30% of the simulated muons traverse two or less stations.

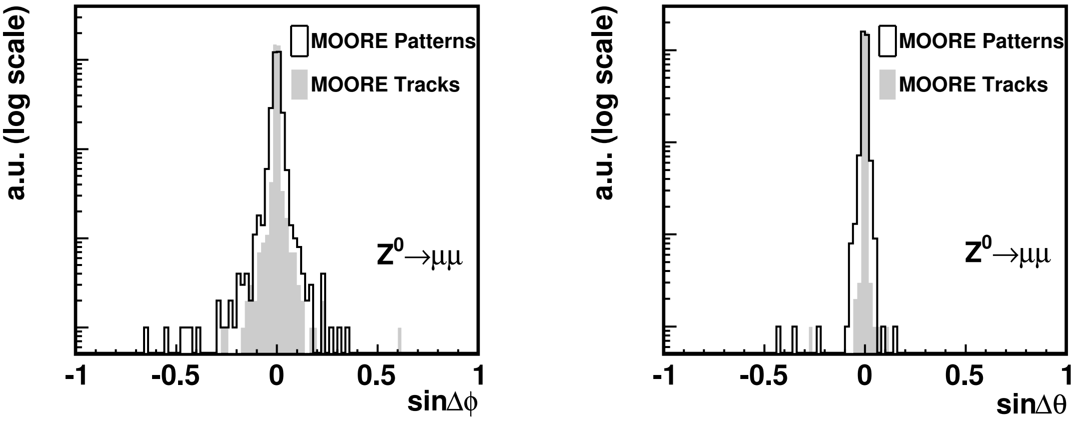

Figure 4.8: *Difference between the ϕ and θ angle of the simulated truth muon and the reconstructed ϕ and θ angle, both for matched patterns and matched tracks.*

The truth matching allows to study the precision of the reconstructed patterns. Figure 4.8 shows the $\sin \Delta\phi$ and $\sin \Delta\theta$ for matched patterns. By fitting the core of the distribution, defined as $\pm\ 2\sigma$, with a Gauss distribution, a sigma of 20 mrad in ϕ and 10 mrad in θ is obtained. As a reference on the final precision, the distributions for the matched tracks are shown as well.

In figure 4.9 the distribution of the number of matched stations in all patterns per

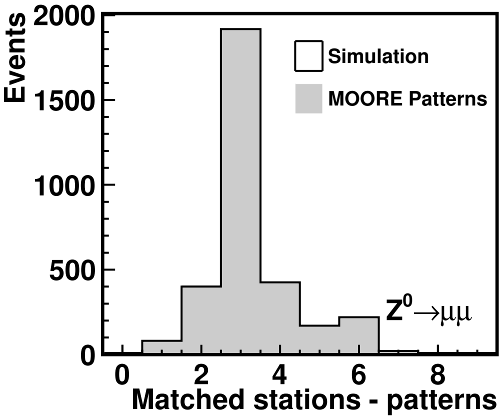

Figure 4.9: *Total number of matched stations in patterns per simulated muon for $Z^0 \to \mu\mu$ events.*

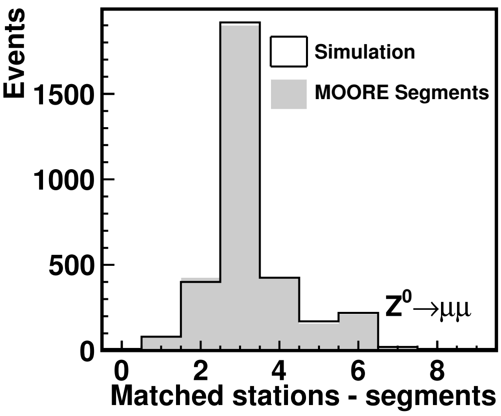

Figure 4.10: *Total number of matched stations in all segments per simulated muon for $Z^0 \to \mu\mu$ events.*

simulated muon is shown. The black line shows the number of stations crossed by the simulated muon. Note that this is the same distribution as figure 4.7. The shaded area shows the number of matched stations found on the patterns. The reconstructed pattern distribution follows the simulation with an efficiency of 99.4%.

Figure 4.10 is the same plot, this time for the number of matched stations per muon on all segments. As can be seen, a small fraction (1.0%) of the segments are lost compared to figure 4.9.

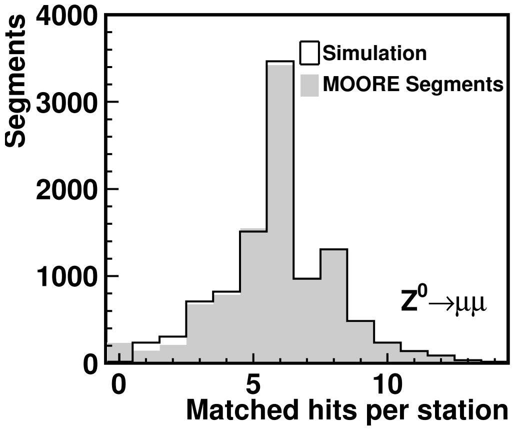

Figure 4.11: *Number of matched MDT hits per station for $Z^0 \to \mu\mu$ events.*

Figure 4.11 shows the number of matched MDT hits per station for matched segments. A hit is defined as matched if the simulated muon crosses the tube. The distribution has two maxima, one at six and one at eight hits, corresponding to segments from the middle and outer MDT chambers, which have six tube layers and from the inner MDT chambers, which have eight tube layers. Note that although the minimum

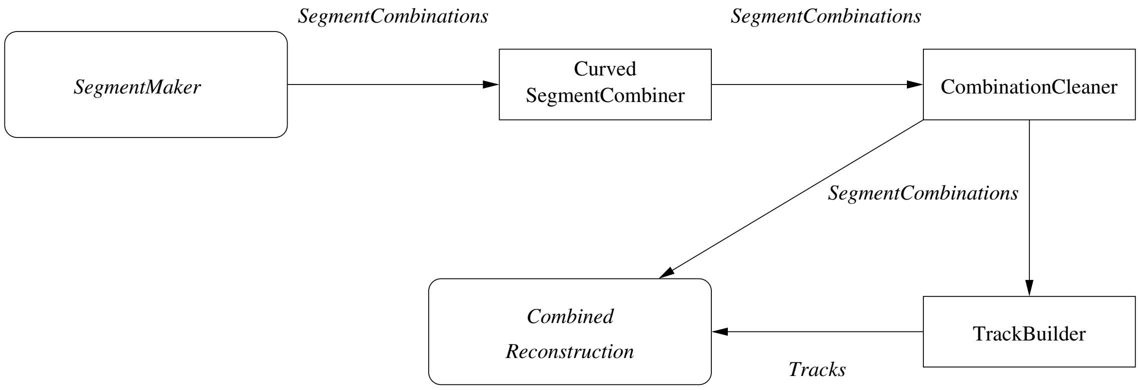

Figure 4.12: *Flow diagram of MOORE's TrackBuilder.*

number of hits in a segment is three, there can still be reconstructed segments that have only one or two matched hits due to segments covering more than one station.

4.3 Track finding and fitting

Although the initial pattern recognition is global, it is too crude to fit the produced segment combinations immediately. For example, there might be several segments per station, segments not belonging to the muon or even two muons close together in one combination. For each combination a second more refined pattern recognition needs to be performed which produces track candidates. These track candidates can then be fitted. Since the fitting procedure can only be performed with a full fit, i.e. with material description, it is cpu-intensive. Therefore, the number of combinations and track candidates has to be reduced as much as possible.

The way this problem is tackled, is inherent to the strategy used for track finding. The track finding is based solely on the produced segments. Since in the muon spectrometer all stations have a possibility for standalone reconstruction (segments), this will not give a possible loss in performance. Using the high-precision segments as seeds for the track finding results naturally in a low number of track candidates and consequently low fake rates.

A detailed diagram of the algorithmic flow of the track building in MOORE, is shown in figure 4.12. The segment making step, discussed in the previous section, outputs segments, which are in turn processed by the SegmentCombiner that produces track candidates. These candidates are cleaned from duplicates and finally fitted to tracks by the TrackBuilder. The produced muon standalone tracks can subsequently be further processed in combined reconstruction, which involves combining the muon spectrometer results (tracks and/or segments) with measurements from the calorimeter and the inner detector. A few remarks will be made about this in section 4.4.3.

The individual algorithms are explained in detail in the following sections.

4.3.1 Track finding

For the second pattern recognition stage, the MuonCurvedSegmentCombiner [60] algorithm is developed. The algorithm takes as input segment combinations and outputs a set of track candidates. The general strategy is to build from one combination all possible track candidates with at least two segments, either MDT or CSC.

First of all, there is a cut on the number of holes on a segment to suppress combinatorics on high-background events. This should be less than 80% of the number of hits. When there are confirmed trigger hits, the cut is loosened to less than 120%.

All remaining segments in the combination are ordered with the following criteria:

- **smallest number of segments in the station:** segments that are isolated are preferred as seed for combining;
- **smallest number of holes + smallest number of missed trigger layers/2:** less missed hits and layers indicate a better segment;
- **momentum:** higher momentum estimate of pattern gives a higher probability for interesting physics and a direct muon.

For CSC segments their χ^2 is also taken into account for the ordering. If there are more than 10 segments in a station, only the best 10 are used.

Starting with the highest ranked segment, lower-ranked segments are tried for *compatibility* with the segment. If a pair of compatible segments is not yet associated to any other track candidate, the pair is saved as a track candidate. If one of the segments is already part of a track candidate, then the other one is saved to this track candidate, if it belongs to the same pattern, otherwise a new track candidate is saved.

A segment is said to be *compatible* with another segment when they originated from the same pattern and a simple χ^2 fit gives an absolute *pull* lower than 5 for the position and direction of both of the segments. The pull p of a fitted variable x is defined as:

$$p = (x_{meas} - x_{fit}) / \sqrt{\sigma^2_{meas} - \sigma^2_{fit}} \tag{4.1}$$

where x_{meas} is the measured value and σ_{meas} its measured error; x_{fit} is the fitted value and σ_{fit} its fitted error.

For two segments in an overlap region (e.g. BOL/BOS) and for segments in the middle-outer endcap (e.g. EML/EOL) a straight line fit is performed. For other chambers a curved fit with IP constraint is done. Note that the same trackmodel is used as for the pattern finding discussed in chapter 3. If the curved fit fails, i.e. one of the absolute pulls is larger than 5, a straight line fit is tried. For cosmic ray muon reconstruction this is done vice versa, the straight track fit is tested first and in case of a failure the curved fit is tried. For cosmic ray muons no IP constraint is used.

To account for multiple scattering and difficult regions in the fit, error scaling is used when fitting low momentum particles, hits from extended chambers, small-large and barrel-endcap overlap regions, and segments with no ϕ hits. Note that this fit is relatively simple compared to ’full’ fits, without taking any material into account. This is done to make it fast and to allow loose association.

With this strategy the candidates are *built up* segment by segment. Note that track candidates might contain several segments from the same layer or station.

Cleaning

Due to the nature of the pattern recognition, the list of track candidates might contain duplicates or almost identical candidates. To prevent the relatively cpu-intensive track fit to be called too often, a track candidate cleaning is performed [61].

Duplicates are removed and when two track candidates share more than 50% of the segments, they are merged.

4.3.2 Track builder

When the current MOORE track builder was written, one of the main goals was to exploit the full potential of the common tracking tools that were already in use by the inner detector reconstruction [62]. There is a broad range of common tools available for fitting, extrapolating, material description, ambiguity solving, etc. To steer these common tools, a few muon spectrometer dedicated tools have been written.

In the MOORE track builder the following steps can be distinguished:

- **Resolving station overlaps:** Segments from neighbouring stations need to be merged for the track to stabilise the fit;
- **Seed selection:** As the tracks are built segments by segment, it is important to start with a well-reconstructed segment as seed;
- **Adding segments:** Segments from the same track candidate are added to the track by performing a fit;
- **Track cleaning:** When the track has been built, wrongly associated segments and outlier hits are removed;
- **Hit recovery:** Possible missed hits are put on the track by a hole search;
- **Segment recovery:** Possible missed segments are put on the track by a seeded segment search;
- **Ambiguity solving:** Individual hits can be assigned to multiple tracks, this needs to be resolved.

These steps are displayed schematically in figure 4.13. In this section these steps and the most important muon and common tracking tools are described.

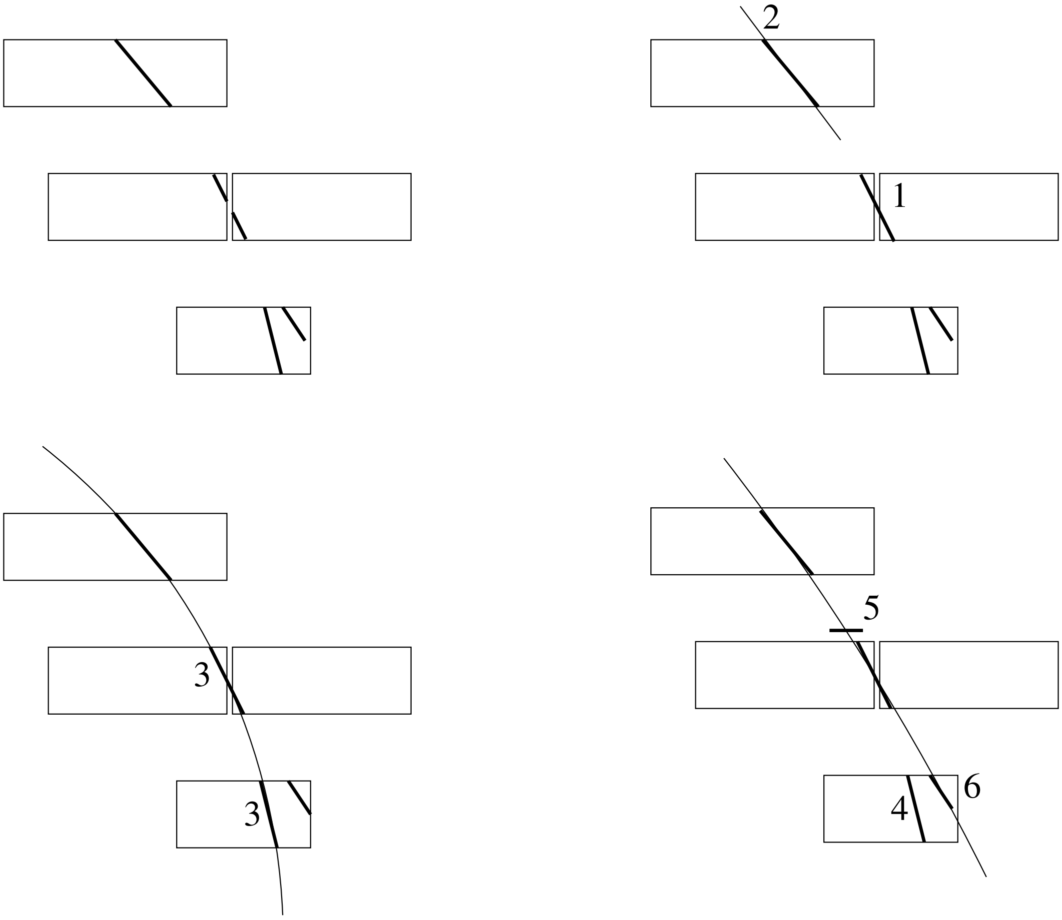

Figure 4.13: *Schematic overview of the track builder steps. From upper left to bottom right: reconstructed segments are shown; step 1: resolve segments from neighbouring stations into one segment; 2: select a segment for building the track; 3: add segments to the track; 4: clean the track from wrongly associated segments and tracks; 5: add possibly missed hits (in this case a trigger hit is added); 6: add possible missed segment to the track.*

Resolving overlaps and seed selection

As has been described in the previous section, a track candidate consists of a set of segments, of which possibly several are from the same station. The strategy is to build up the track segment by segment like is done in the Track Finding. A track is built up from the outer region of the muon spectrometer to the inner region. This is done since in general the segments from the outer chambers are more isolated and suffer less from combinatorial background.

First if there are two or more segments in an overlap region, e.g. BOS/BOL, these segments are tested by the trackfit for possible merging. Next the segment with the highest quality in the outer region that is not yet associated to any track, is taken as seed.

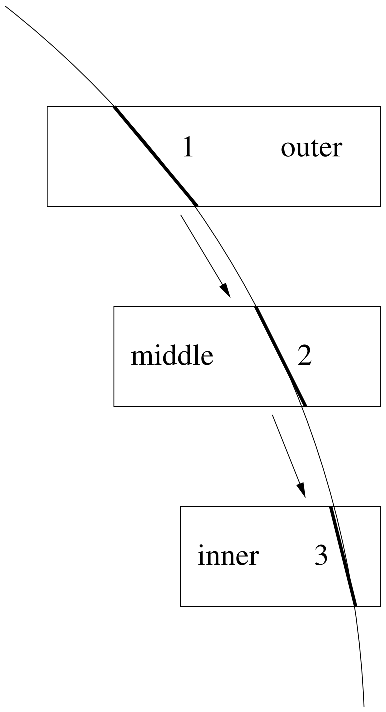

Figure 4.14: *Sequence order for adding segments to a track.*

Adding segments

Then a segment from a middle segment is tested for adding. The 2 segments are fitted by the fitter, which is described in the next section. If the fit is successful, i.e. the residuals have absolute pulls smaller than 5, the segment is added, and a next segment will be tested for adding. This is done until all segments are tested. The default sequence of adding stations is: outer, middle, inner, extended stations, see figure 4.14 for a simplified representation. When some chambers are noisy the sequence can be modified to reduce combinatorics. Several tracks can be made with this procedure out of one track candidate.

Segment fitter

The segment fitter is an algorithm that fits 2 segments or, a segment and a track, into a track. Additional ϕ hits are taken from the segments and from the original patterns. As these ϕ hits are taken directly from the pattern recognition, they might contain outliers or ambiguities. To stabilise and improve the resolution of the fit, the ϕ hits are clustered, by making Competing RIOs On Track, and cleaned with a straight line fit in the (x, y)-plane with IP constraint. For cosmic ray muons this constraint is dropped.

The cleaned ϕ hits are fitted together with the stripped segments hits by the fitter. The default fitter for MOORE is the GlobalChi2Fitter [63]. As seed for the θ direction, the θ angle of the innermost segment is taken. For the ϕ direction, the average ϕ angle of the ϕ hits is taken. Since for cosmic ray muons there is no IP constraint, the difference of the position of the innermost and outermost precision hit is taken as seed.

When the track candidate has no ϕ hits, the ϕ value of the η hits are taken as seed.

Due to the high modularity also other fitters such as the KalmanFitter [64] and the iPatFitter [65] can and have been tried. The GlobalChi2Fitter is chosen for its material handling and it is most stable in the difficult transition regions [59].

For cosmic muons, scattering errors are enlarged.

Material description

Track reconstruction requires a detector geometry with a detailed material description for precise extrapolation, as scattering and energy loss will have a considerable impact on the track fit quality. Most fitters are able to correct for these effects. The muon spectrometer has two material descriptions for tracking purposes available. For CPU-reasons the description will be a simplification of the description used for simulation.

The Muonboy reconstruction algorithm [58] has a method for the retrieval of their material database. The material has its own extrapolation and navigation methods. In chapter 5, the Muonboy algorithm will be briefly described and a comparison with MOORE will be performed on cosmic ray simulation.

The Muon Tracking Geometry (MTG) is based on the general ATLAS Tracking Geometry [66], the common ATLAS detector description. The described parts have knowledge of their surrounding parts, which is used for navigation. For extrapolation a method based on the Runge-Kutta-Nystrom integration method [67] is used.

For MOORE and the GlobalChi2Fitter, the Muonboy material is chosen as it adds possibilities for scattering in the transition region where the magnetic field is not well known. Thus making the fit more stable and less likely to diverge, while the fit with MTG material encounters problems in this region [59]. Currently, it is not possible with the Muonboy material to extrapolate from the outer layers towards the inner layers, which is needed for cosmic muon reconstruction. Therefore, the MTG material is used for the cosmic muon track reconstruction.

Track cleaning

After a track has been fitted successfully, it undergoes several stages of refurbishing. First a track is cleaned by the MuonTrackCleaner from outliers or bad measurements. This is performed in two steps. First, whole stations are tested for removal. If the average pull of the hits in a station is larger than 3.5 and not a single hit is a large contributor to this average, the station is removed. As a minimum, a track will keep at least two precision stations (MDT or CSC).

Then a more refined cleaning on the hit level is performed. The individual MDT driftcircle hits are tested for their driftradius sign[1]. Once the direction of the track is known, in principle two positions are possible for each driftcircle and in rare cases the segment maker has chosen the wrong one. The driftcircle sign is changed, when the

---

[1] The sign of a driftradius is defined as the sign of the cross product between the direction of the track and the driftradius in the local surface of the chamber.

pull contribution of the MDT hit to the track is lower in case their drift circle sign is changed.

Finally, hits that were already flagged as outliers before the cleaning procedure are tried to put on the track.

Hit recovery and holes

For more diagnostics and possible hit recovery, a search is performed for possible missed layers on the track or, in the case of MDTs, tubes. There are many possible reasons for a missed layer, e.g. a dead channel, the muon traversing some non-active part of the detector or even a real hit that was somehow missed by reconstruction. The search is performed in all chambers that already have a hit on the track. If there is a missed layer or tube, it is checked if there is a channel that fired, i.e. a PrepRawData object.

For the MDTs, if such a PRD is found it is put on the track, if it has an (absolute) pull of less than 3. If the pull is larger, it is flagged as an *outlier*. If no PRD is found, the tube is flagged as a *hole*. For the other technologies the PRD with the smallest pull less than 5 is put on the track and again if no such PRD is found, the layer is flagged as a hole.

Segment recovery

Although most of the individual segments are reconstructed correctly, they sometimes belong to a different combination, which results them not being added to the track. Each track is checked for having inner, middle and outer segments. If there is one of these layers missing, a seeded segment search is performed to recuperate possible lost segments. As seed, the parameters of the segments are taken. If a segment is found in this way, the hole search is redone.

Track with hits in only one station and tracks that have hits in two stations and more than 5 holes are discarded.

Track ambiguity solving

After the tracks have been reconstructed, it might happen that hits or even segments are shared by more than one track. These ambiguities need to be resolved. This is achieved by sorting the tracks on a quality criterion, which includes the number of hits and the χ^2. For each track starting with the highest quality track, all tracks with a lower quality that have overlapping hits with this track, have these hits removed, are refitted and their qualities are recomputed. When this refit fails, the track is discarded.

The purpose of this procedure is to assign the ambiguous hits to tracks that are most likely to be a muon. Furthermore, with this procedure some wrong tracks will be discarded.

After the hit ambiguities have been solved, the remaining tracks are pairwise tried for possible merging.

4.4 Performance

In this section the reconstruction performance of the standalone MOORE algorithm, which has been discussed in detail in this and the previous chapter, will be shown on two Monte-Carlo simulated physics samples, $Z^0 \rightarrow \mu\mu$ and $J/\psi \rightarrow \mu\mu$. These two samples have been chosen, because they simulate 'real' physics and are especially important channels for first data taking.

Plots that demonstrate the performance of the MOORE algorithms, like track efficiency, and number of segments per track will be shown. Although a track is characterised by 5 parameters, only the transverse momentum is studied. The precision on the direction parameters are in general much better than required for any physics studies while the initial position parameters in the vertex region are measured by the inner detector with much better precision.

The efficiency is defined as the fraction of simulated muons that are matched to reconstructed tracks. Matching is achieved by counting the number of shared hits with a penalty when the reconstructed momentum is too far off from the simulated one. In order to show the performance of the track reconstruction, some cuts on the simulation are made to exclude muons that can never be reconstructed, namely $|\eta| < 2.8$ and at least 1 precision hit in the muon spectrometer is required. The efficiency without any requirements on the muon spectrometer response, the so-called physics efficiency, will be quoted as well. This number is important for physics studies, for which no simulation cuts can be set.

The efficiency should always be compared to the expected fake rate. A few remarks about the expected fake rate will be made at the end of this section for a $t\bar{t}$ sample. A few words will be said as well about combined reconstruction, i.e. combining the standalone muon tracks and segments with inner detector and calorimeter measurements. More elaborate performance and comparison studies are covered in reference [68].

4.4.1 Performance on di-muon samples

Both di-muon samples are generated with PYTHIA [69] and produced with a misaligned detector description. The misalignment is corrected for in the reconstruction software. The Z^0 sample has 2000 and the J/ψ sample 3050 events. Both samples are forced to decay to two muons and have a filter, selecting only events where both muons have, at the IP, $|\eta| < 2.8$ (2.5 for J/ψ) and $p_T > 5$ GeV (4 GeV for J/ψ). Muons produced by other processes are suppressed. First, results on the $Z^0 \rightarrow \mu\mu$ sample will be shown and later some differences when reconstructing the J/ψ sample will be discussed.

Figure 4.15 shows the track efficiency for $Z^0 \rightarrow \mu\mu$ events as function of η. The gaps in the distribution correspond with reduced detector coverage in the muon spectrometer. $\eta = 0$ corresponds with the gap needed for services for the solenoid magnet, the calorimeter and the inner detector. $\eta = \pm 1.2$ corresponds with the barrel/endcap transition region where several stations are missing for initial data-taking, see also figure 4.7. The average efficiency is 95.8% and when all cuts are dropped, the physics efficiency becomes 94.9%.

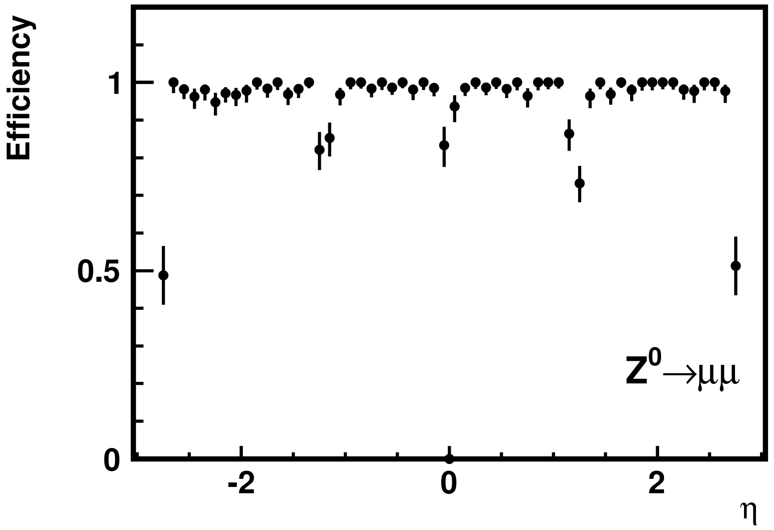

Figure 4.15: *Muon efficiency as function of η for $Z^0 \to \mu\mu$ events.*

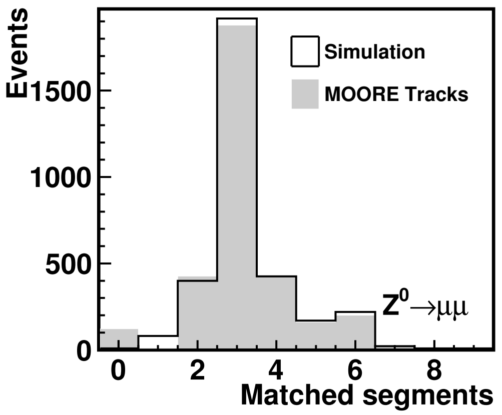

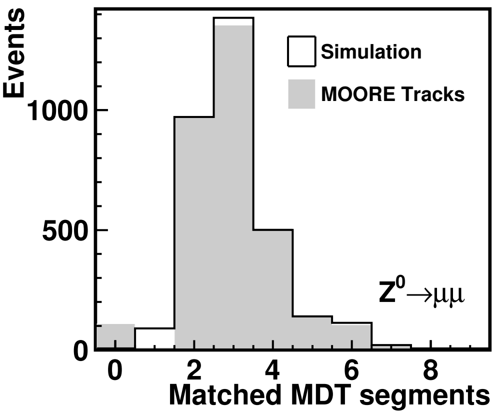

Figure 4.16: *Number of MDT and CSC segments assigned to tracks for $Z^0 \to \mu\mu$ events.*

Figure 4.17: *Number of MDT segments assigned to tracks for $Z^0 \to \mu\mu$ events.*

In figure 4.16 the distribution of the number of matched segments per reconstructed track is shown. The figure is similar to the figures 4.9 and 4.10, which show this distribution for patterns and segments.

The first bin is the inefficiency, which is largely caused by muons that only pass one chamber. By principle the track fit will not reconstruct these muons as tracks. Apart from this expected inefficiency the distribution follows the simulation close to perfectly.

Figure 4.17 shows the same plot, but now for MDT segments only. Note the different distributions of the simulation and the fraction of tracks that have a CSC segment.

The left plot of figure 4.18 shows the fractional residual of the momentum which is

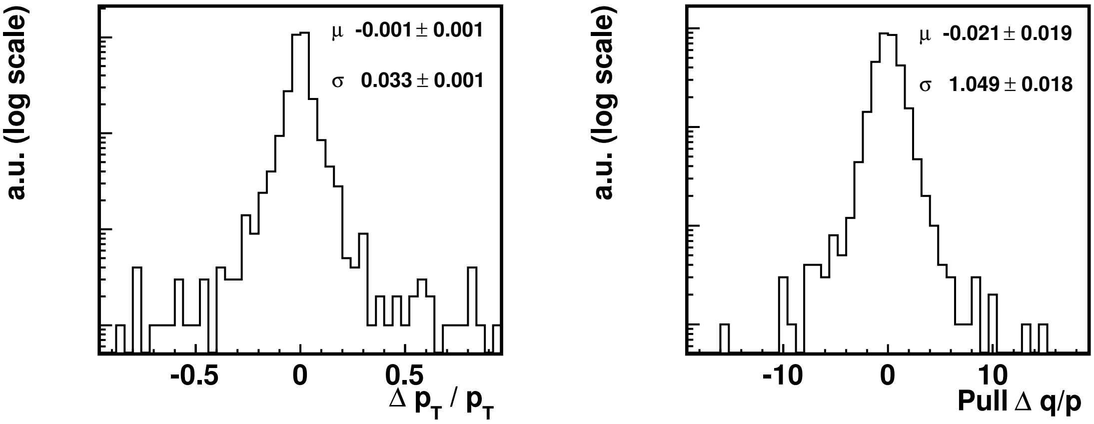

Figure 4.18: *The fractional residual of the momentum (left plot) and its pull distribution (right plot) for $Z^0 \rightarrow \mu\mu$ events.*

defined as:

$$\frac{\Delta p_T}{p_T} = \frac{p_{Tsim} - p_{Trec}}{p_{Tsim}} \tag{4.2}$$

It is a measure for how well the momentum is reconstructed. The width of the distribution, $\sigma(\frac{\Delta p_T}{p_T}) = 3\%$. The right side of figure 4.18 shows the pull of the fractional momentum resolution and shows that the errors and reconstruction are understood.

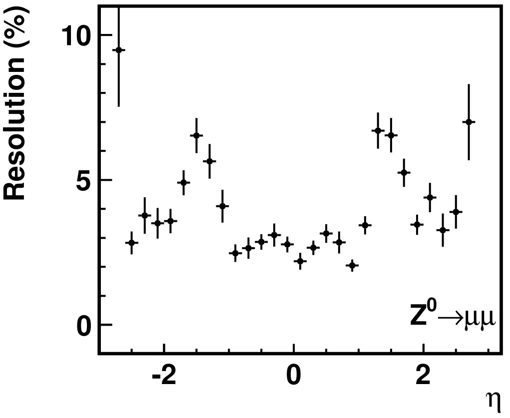

Figure 4.19: *Relative transverse momentum resolution as a function of η for $Z^0 \rightarrow \mu\mu$ events.*

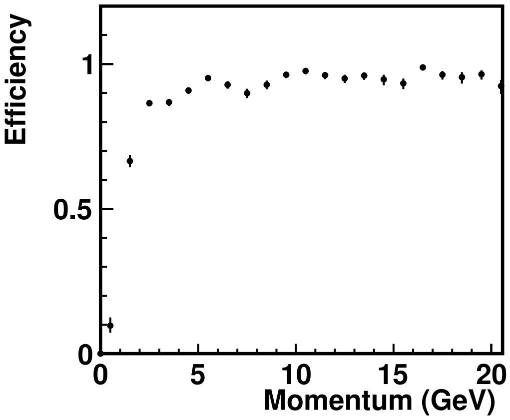

Figure 4.20: *Muon efficiency versus momentum in the muon spectrometer. Different simulated samples are used.*

The resolution of the momentum is now defined as the variance of the Gaussian fit and is shown as function of η in figure 4.19. The resolution is degraded between a pseudorapidity of 1.2 and 1.7 for a few reasons, namely, the reduced number of measurements (figure 4.7), the low magnetic field integral in the overlap region of the barrel and endcap magnets (figure 1.13) and the material in the endcap toroid (figure 2.2).

Low momentum muons

Muons originating from a Z^0-boson have on average a momentum of several tens of GeV. These muons produce straight, non-showering tracks, which are relatively easy to reconstruct. For a more difficult study, in particular important for startup, muons decaying from a J/ψ are studied. When reconstructing muons with a lower momentum of a few GeV, several complication arise:

- **Curvature:** Due to their low momentum the muons have a highly curved track. The reconstruction will sometimes miss a station and in these cases the momentum measurement will be degraded;
- **Less Segments:** When the curvature is too large, it happens that the outer stations are not reached, but instead the muon has turned back towards the calorimeter. For even lower momenta the middle stations are not traversed;
- **Scattering:** Low energy muons are more susceptible for scattering. Therefore, the trajectory will have more kinks and a good material description is needed to be able to predict the trajectory of the particle. Furthermore, low momentum muons are more likely to have scattered in the calorimeter, making them non-pointing to the IP. The pattern recognition will be inefficient for these muons.

To improve the understanding of low momentum muon reconstruction, the efficiency is plotted versus the momentum in figure 4.20. This plot has combined all events from the J/ψ, Z^0 and $t\bar{t}$ samples. For momentum higher than 4 GeV the muons are reconstructed with an efficiency of 95%, while below this momentum, the efficiency drops steeply, mainly because these muons often don't reach the middle and outer station layers.

In figure 4.21 the track efficiency is shown for the J/ψ sample as a function of η. As expected the efficiency is degraded compared to the $Z^0 \rightarrow \mu\mu$ efficiency of figure 4.15, especially in the barrel region. Since there is a cut for all muons on the transverse momentum of 4 GeV, muons in the endcap ($|\eta| > 1.5$) have a momentum of at least 9 GeV. As can be seen in figure 4.20 these muons are reconstructed more efficiently. The average efficiency is 93.2%

The number of segments matched per track for J/ψ events, figure 4.22, is also lower compared to figure 4.16. It can be noted that there are some reconstructed tracks that cross only 2 stations, while more segments could have been assigned. The main reason is that the trackbuilder sometimes selects an incorrect segment instead of the right segment. Note that compared to Z^0 sample, the simulation has on average a lower number of segments per generated muon.

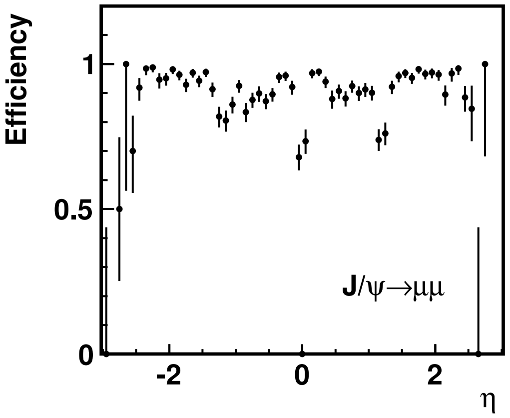

Figure 4.21: *Muon efficiency as function of η for $J/\psi \rightarrow \mu\mu$ events.*

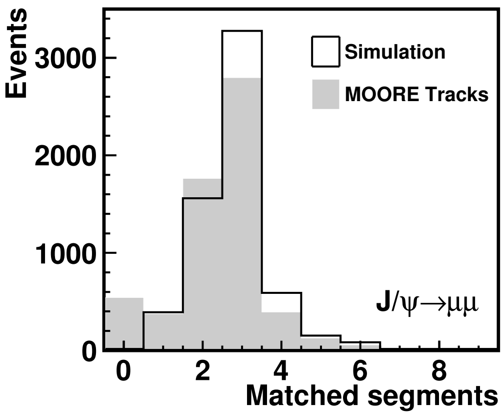

Figure 4.22: *Number of MDT and CSC segments assigned per track for $J/\psi \rightarrow \mu\mu$ events.*

4.4.2 Fake rate for $t\bar{t}$ sample

Efficiency numbers should always be compared to the expected fake rate. As for initial running, pile-up and cavern background will not be an issue, most fake tracks will be made in busy, high occupancy events. Therefore, a $t\bar{t}$ sample without background is chosen for fake rate studies.

A fake track is defined as a reconstructed track that is not the best match to any simulated muon. The fake rate is defined as the number of fake tracks divided by the number of reconstructed tracks.

The events in the $t\bar{t}$ sample require the presence of at least one lepton and is produced using MC@NLO [70], [71] in conjunction with Herwig [72]. This sample provides a variety of mechanisms for producing muons, so-called direct muons from leptonic W-boson decay and so-called indirect muons from quark decays (b, c or pion).

When requiring muon spectrometer precision hits and a p_T cut of 5 GeV, the total MOORE efficiency on this sample is 96% and the fake rate is 3%.

Figure 4.23 shows the muon momentum distribution at the entrance of the muon spectrometer for this sample. The sample is dominated by low momentum muons and provides a momentum distribution somewhat similar to what is expected for LHC-collisions, cf. the (non-triggered) muon cross sections, figure 2.5. The number of matched reconstructed tracks is also shown.

In the previous section it was explained that the reconstruction is more difficult for low momentum muons. This can also be indirectly seen in figure 4.24, where the fake rate is plotted versus the momentum of the reconstructed muons. The fake rate is higher for low momentum, while for momenta larger than 10 GeV, the fake is rate is below 0.1 per event. As low momentum tracks have larger errors on the track parameters and more possibilities for scattering, these are also more susceptible for fake tracks.

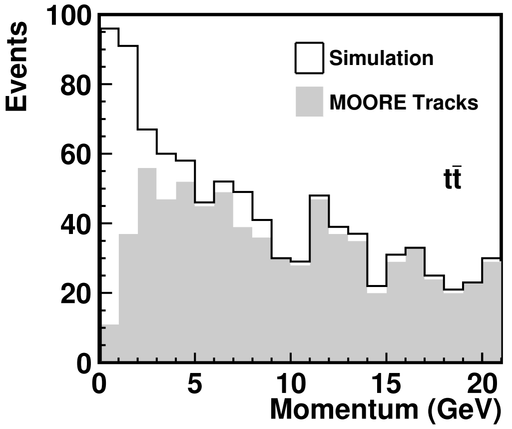

Figure 4.23: *Simulated muon momentum in the muon spectrometer for $t\bar{t}$ events.*

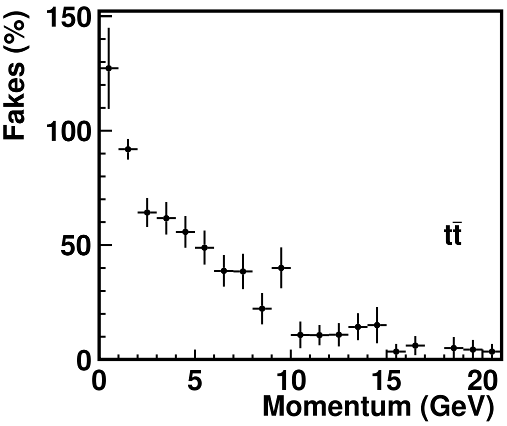

Figure 4.24: *Muon fake rate versus momentum in the muon spectrometer for $t\bar{t}$ events.*

4.4.3 Combined reconstruction

Until now this chapter has covered only *standalone* reconstruction and performance. However for physics studies, it is often necessary to know the parameters of the found muon at the vertex. Therefore, the muon spectrometer tracks are extrapolated back to the vertex through the calorimeter, taking into account scattering and energy loss. These muons are called *standalone muons.*

After backextrapolation the muon spectrometer tracks can be matched to inner detector (ID) tracks and *combined* tracks are fitted by combining the measurements of both tracks and possibly calorimeter measurements.

For very low momentum muons, that do not reach the middle and outer layers of the muon spectrometer, *tagging* algorithms are developed which propagate ID tracks to the muon spectrometer and search for nearby segments.

The advantages of studying combined tracks are:

- **Recovering holes:** While standalone reconstruction has a slightly greater $|\eta|$ coverage up till 2.7 compared to 2.5 for combined reconstruction due to ID layout, the ID recovers the holes near $\eta = 0$ and $\eta = \pm 1.2$ in the muon spectrometer. Also low efficiency regions with lower chamber coverage, like the transition region and the feet, will recover efficiency through the tagging algorithms;

- **Low momentum muons:** Low momentum muons will be reconstructed with a higher efficiency and better momentum resolution;

- **Reducing background and fake rates:** Muons produced in the calorimeter by secondary processes, e.g. from π and K decays will serve as a background for most physics analysis and will be strongly reduced when studying combined tracks. Also fake tracks from pile-up and cavern background will be reduced, as there will not be a matching ID track in general;

- **Improved momentum resolution:** For transverse momenta below 30 GeV, the inner detector provides the best measurement. Furthermore, due to energy loss fluctuations in the calorimeter, the momentum resolution in the muon spectrometer suffers from tails. These tails can be reduced by including the inner detector measurements in the fit.

Disadvantages are:

- **Detector alignment:** To achieve the optimal result for the combined reconstruction, the alignment between the inner detector and the muon spectrometer needs to be known sufficiently. However, it is expected that during first data-taking the alignment precision will not reach its final precision;

- **Calorimeter material:** The material in the calorimeter has about 100 radiation lengths. The resulting energy loss and scattering in the calorimeter give rise to complications in the fit, and therefore the extrapolation needs to be well understood.

4.5 Conclusions

This chapter has described the ATLAS software framework ATHENA and its event data model. All common tracking objects and their muon extensions that are used in the muon reconstruction algorithms, have been described in detail.

The muon reconstruction chain is split into several individual parts and due to the common objects and interfaces, algorithms can be easily interchanged. The recently developed algorithms of the revised MOORE reconstruction programme have been described in this chapter, except for the first part, the pattern recognition, which was already covered in the previous chapter. The other steps, namely the segment making, the track building and the ambiguity solving have been described in detail. Besides the offline reconstruction, MOORE is used as the main muon reconstruction programme in the Event Filter, the highest level software trigger of the ATLAS trigger system.

For the different stages, performance studies were performed on different simulated samples that are important for first data taking, covering both low energy ($p_T < 5$ GeV) and high energy muons. The individual algorithms are performing well and the total track efficiency and momentum resolution are well understood and competitive to other standalone tracking algorithms. Fake track rates have been discussed and are shown to be under control.

Chapter 5

Simulation of cosmic ray muons

Before the start of the LHC and the ATLAS experiment, an intense period of detector commissioning has been performed. Prior to having a beam in the LHC, the ATLAS cavern has been closed, which means no modifications to the detector geometry or the cabling are possible anymore during the LHC proton-proton collisions.

Thus, in the commissioning period many of the final tests can and will have to be performed to prepare optimally for the experimental data to come. In this period the detectors are once again checked and repairs are made. The final services (cables, gas systems, voltage systems, etc.) are connected and tested. Also all the subdetectors are integrated and both the data acquisition system (DAQ) and the triggers are run and tuned. Calibration and alignment constants are measured and stored into the various databases. Furthermore, the computing model [73] is seriously tested for the first time.

For many of the commissioning, the 'most realistic' (i.e. resembling the LHC circumstances) way of performing these tests is to use cosmic rays and in particular cosmic ray muons as a particle source.

To improve the understanding of the detector response and the trigger for these cosmic ray muons, a dedicated simulation programme has been written. Comparisons between simulated and raw data will help to spot and diagnose problems in the commissioning tests.

In this chapter the simulation and the analysis of the simulated cosmic muon data is described. In the next chapter raw cosmic muon data are analysed and comparisons between simulation and raw data are made.

5.1 Description of cosmic ray simulation

5.1.1 Detector simulation

The ATLAS detector simulation is done using the GEANT4 programme [74]. This programme simulates the passage of particles through matter as realistically as possible. It contains all of the known relevant physics processes in the energy range of 250 eV up to several TeV. The ATLAS detector geometry is implemented in the GEANT4 geometry model in great detail and is described by a huge set of volumes (about one million) [75]

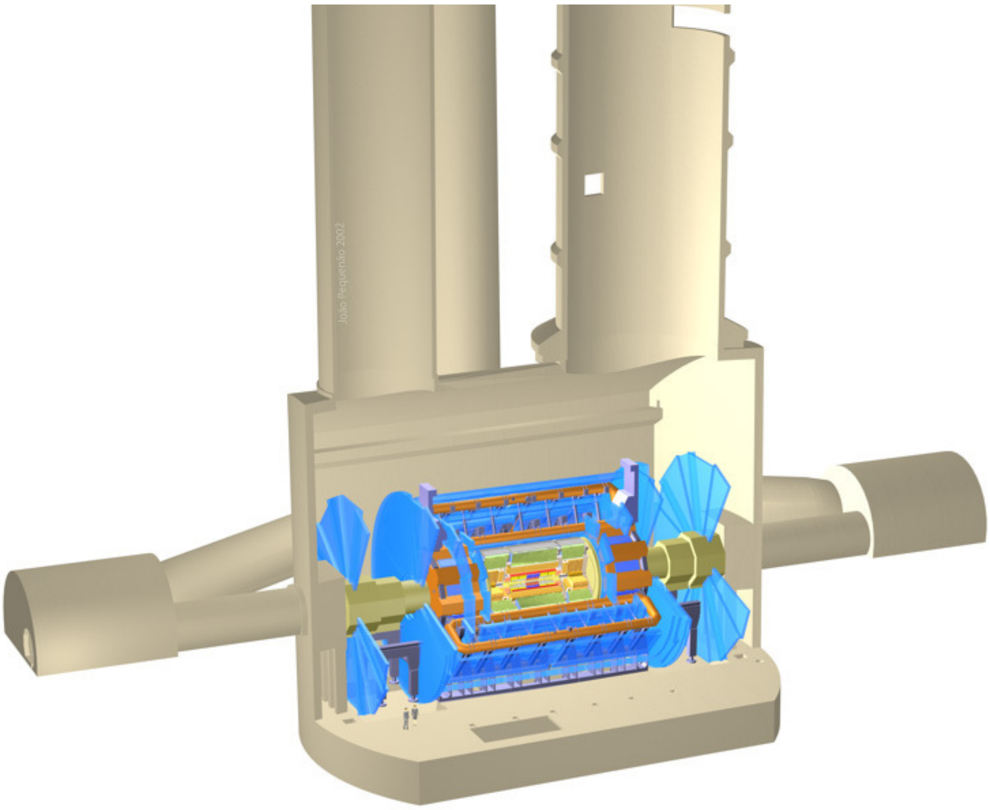

Figure 5.1: *Artistic impression of the ATLAS detector in its cavern.*

that each have an individual material composition which is used to calculate the physics processes in them. Also included in the simulation is the shape of the ATLAS cavern, the main service shafts and the rock, see figure 5.1. Data taking was often overlapping with the installation work, due to which the detectors were sometimes not yet in their nominal position or not connected to the data acquisition system. Therefore, simulations can and have been run with geometries different from the nominal one and detectors partially or completely switched off. Also the magnetic field can be switched on or off in the simulation, depending on the desired situation.

5.1.2 Cosmic ray muon simulation

Cosmic rays at the sea level consist mostly of muons (and neutrinos) as can be seen in figure 5.2. Above an atmospheric depth of about 500 g/cm^2 (equivalent to about 5 km above sea level) muons are the dominating particle source. Since the other interacting particles are absorbed by the rock above the ATLAS detector, only muons (and neutrinos) will penetrate to the 100 meters under ground cavern.

The energy spectrum of cosmic ray muons at sea level can be seen in figure 5.3, and the total rate for muons above 1 GeV is about 70 Hz/m^{2}sr [76].

In the simulation, the specific muon generation is performed at the surface of the Earth on a 600 by 600 m^2 area, centered above the ATLAS nominal interaction point.

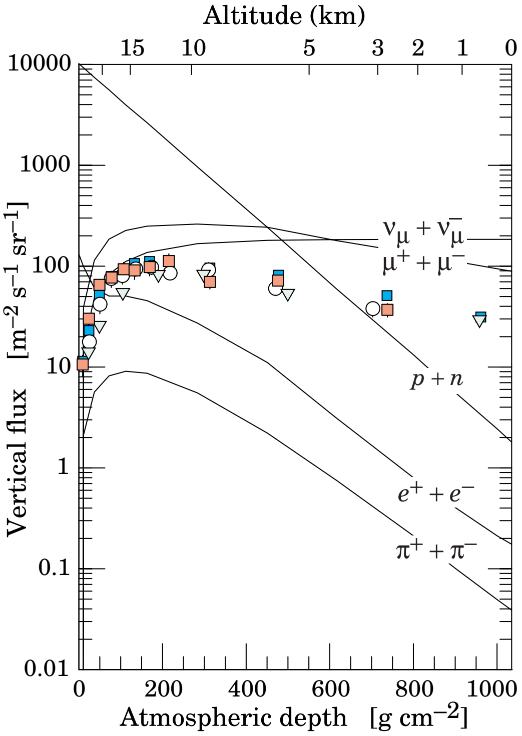

Figure 5.2: *Vertical fluxes of cosmic rays with $E > 1$ GeV [76]. The markers show the measurements for negatively charged muons.*

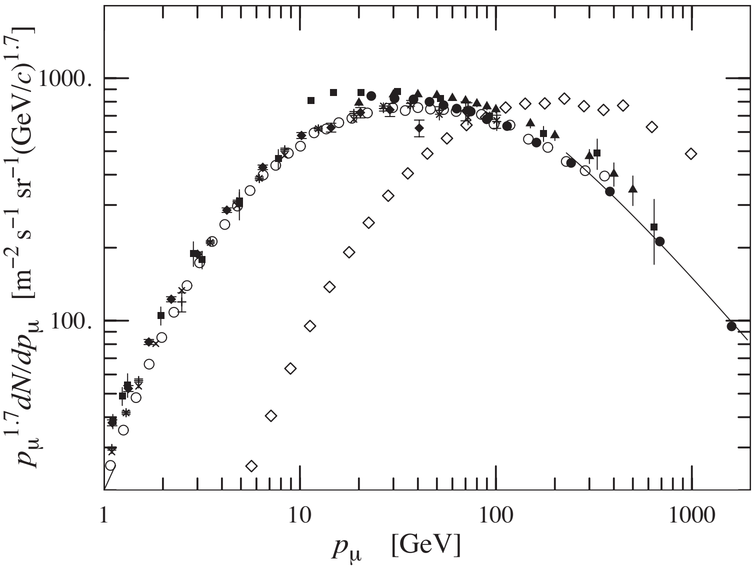

Figure 5.3: *Momentum spectrum scaled by $p_\mu^{1.7}$ of cosmic ray muons at sea level at two different values of the zenith angle θ (perpendicular to the azimuthal plane), $\theta = 0\,°$ (left arc, various experiments) and $\theta = 75\,°$ (right arc) [76].*

The energy range is set from 10 GeV to 2 TeV. Only the muons, propagated by the GEANT4 simulation, entering the ATLAS detector are stored.

5.1.3 Trigger

The GEANT4 detector simulation data are processed in ATHENA using the Muon Digitization software. The software simulates the output signal of the muon detectors into so-called *digits*. After a conversion step, Raw Data Objects (RDOs) are produced.

The RPC LVL-1 trigger rates for cosmic ray muons are estimated at about 170 Hz for the low-p_T (6 GeV) trigger and about 16 Hz for the high-p_T (20 GeV) trigger [77]. For a comparison, the expected trigger rates for the ATLAS experiment are 19.1 kHz for the low-pT trigger at low luminosity (10^{33} cm^{-2}s^{-1}) [78], [79].

There is no second level cosmic muon trigger, as the ATLAS data acquisition system is able to handle these rates comfortably.

5.2 Cosmic muon reconstruction

Reconstruction of cosmic muons differs in many ways from reconstruction of muons from proton-proton collisions, the most notable features being the cosmic muons not pointing to the IP and not in time with the LHC bunch crossings. These differences demand adaptations to reconstruction algorithms. Several choices for adaptations are driven by the purposes of analysing cosmic muon data.

There are some intrinsic properties of cosmic muons that makes reconstructing them difficult:

- **Detector design:** The muon spectrometer is designed for particles from the IP, which for the greater part will traverse at least three stations. This will not be the case for cosmic muons and the traversed number of stations will vary, depending on their direction;

- **Chambers oriented towards the IP:** Related to the first issue, the individual stations are by design oriented towards the IP, so that trajectories will cross the station perpendicular to their measurement plane. For cosmic muons this is generally not the case, and trajectories may be parallel to stations. This has consequences for e.g. segment reconstruction;

- **Time of flight corrections:** Time of flight corrections should be accounted for in a different way than for IP muons. At present, time of flight corrections are not implemented in the reconstruction. In chapter 6, this issue will be discussed in more detail;

- **Trigger time uncertainty:** For absolute timing, the ATLAS triggers are dependent on the LHC bunch crossing time. However since cosmic muons are randomly distributed, it will give a 25 ns uncertainty on the trigger time. This issue is only valid for real data and will be discussed in chapter 6.

To address these issues, several adjustments are made to the reconstruction. The pattern recognition has dedicated algorithms for cosmic muons as has been described in section 3.2. However for the other parts of the reconstruction, described in chapter 4, the differences are small. The differences are summarised below:

- **No IP constraint:** An interaction point constraint is not used anywhere in the reconstruction. There are only slight preferences for muons coming closer to the IP, as these are more interesting for studies and more likely to have a successful segment and track fit;
- **No magnetic field:** When the magnetic field is off, a straight line model is used to find track candidates and to fit the segments and tracks;
- **Splitting of tracks:** After the pattern recognition stage, the combined patterns are split into two parts. A pattern is split, if it intersects the barrel calorimeter, which is defined as a cylinder around the IP, with a radius of 4 m and a length of 12 m. The splitting is done at the point closest to the IP. The angles of the 'upper' pattern are not rotated to pretend originating from the IP, but the physical direction is kept. This is conform the conventions in the tracking EDM. Patterns that are not intersecting the cylinder are not split. Note that this is the case for most of the cosmic muons crossing an endcap.

  Further track reconstruction is performed on these separate parts. Therefore, a cosmic ray muon traversing the calorimeter is typically reconstructed as two separate muon tracks;
- **Open roads for segment reconstruction:** The direction of the pattern recognition seed is no longer used as a constraint for the reconstruction of segments;
- **Calibration:** Calibration is adjusted to account for the time of flight correction and the increased uncertainty on the trigger time;
- **CPU time:** Trigger rates are low compared to regular LHC running and cosmic muon events have on average a very low number of hits. Therefore, many reconstruction measures to reduce cpu time are dropped and more cpu-intensive algorithms can be afforded. The rare high-occupancy events ('cosmic showers') can be skipped, as these events are not interesting for calibration or alignment studies;
- **Enlarged errors:** To account for possible misalignments, uncertainties in the calibration and timing discrepancies between the different trigger towers, the errors for the MDT drift circles are enlarged to 2 mm. It is envisioned that in later stages of the commissioning this enlargement will be relaxed.

The performance after these adjustments are studied on a simulated cosmic muon sample. Since the sample contains truth information, comparisons can be made between reconstructed and truth information.

5.2.1 Pattern and segment performance

The cosmics muon sample is simulated as described in section 5.1. The detector geometry reflects the current knowledge of the positions of the detectors. For the muon spectrometer this implies that except for the CSCs and a few special MDT chambers, the full detector is simulated. In the simulation, the magnetic fields are switched off; this was the case for most of the real data sets. No-field data are in general more useful for commissioning purposes, in particular for alignment. A sample of 4600 simulated cosmic muon events have been reconstructed. A study similar to the $Z^0 \rightarrow \mu\mu$ study described in section 4.2.2, is performed on this sample.

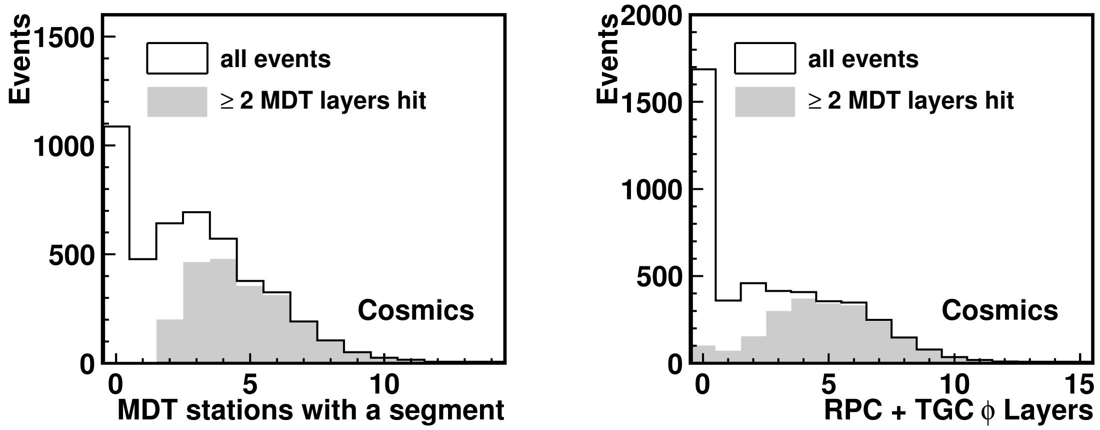

Figure 5.4: *Number of traversed stations by a reconstructed simulated cosmic muon. Left plot: number of MDT stations with a reconstructed segment per event. Right plot: RPC + TGC ϕ layers associated to a segment per event (gas-gaps have been merged). An additional cut on the truth MDT hits, explained in the text, has been applied for the shaded area.*

To get an idea of how many stations have been crossed on average by a cosmic muon, the number of stations with a *reconstructed* segment and the number of ϕ layers (both RPC and TGC) associated to these segments are shown in figure 5.4. The left plot shows the number of MDT stations with segments per event. Since a cosmic muon crosses the detector at arbitrary angles, the traversed number of stations varies greatly and could go up to more than 10 stations for some directions, while on the other hand a large fraction of events only touch the outer layer for which no segment could be reconstructed. The right plot shows the number of ϕ layers with hits; ϕ layers around the same gas-gap have been combined in this plot to reflect the traversed number of stations. The shaded area has an additional cut, referred to as *station truth cut*, on the truth MDT hits: at least three hits in at least two MDT chambers from two different layers (inner, middle, outer) are required. This cut will be applied later for the performance study and reflects the minimum required for reconstructing a track. The left plot shows that in about half of the events not enough information is available and these events will not be considered.

The efficiency for segments and tracks is defined as in chapter 4 and is summarised here: the reconstructed patterns (segments) that have most hits in common with the hits of the simulated muon (in that chamber with a minimum of 80% of simulated hits) are flagged as *matched*.

Most simulated muons are split into two tracks as described in the introduction of this section. Each track is treated as a separate simulated muon and in principle each part is counted for performance measurements after the station truth cut. Only simulated muon tracks that fulfill this requirement are considered for the performance study.

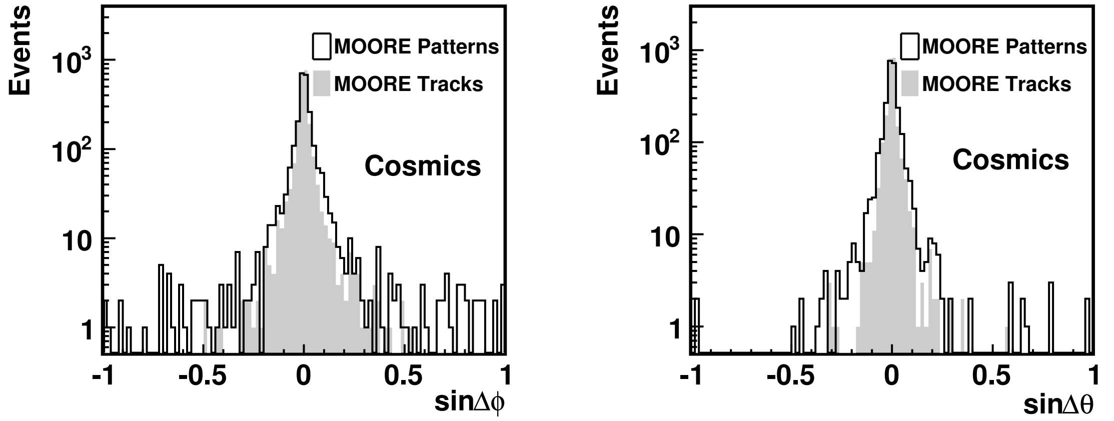

Figure 5.5: *Difference between the ϕ and θ angle of the simulated truth muon and the reconstructed ϕ and θ angle, both for matched patterns and matched tracks.*

In figure 5.5 the quality of the track parameters ϕ and θ of the matched patterns and tracks are shown. While the core of the pattern distributions is in good shape, there are some outliers. These outliers are often patterns that have hits in a small number of stations; for them the direction is difficult to determine. This is caused by muons traversing only the outer layer of the detector or patterns that are incomplete. These patterns will most likely not lead to a reconstructed track.

The same quantities are also shown for the tracks. While the θ resolution of the track has improved much with respect to the θ resolution of the pattern, the ϕ resolution of the pattern is only slightly worse than the ϕ resolution of the track. Note that compared to figure 4.8, all distributions are much broader. This is caused by the IP constraint for collision events and the increased variance on the number of measurements for cosmic muon events.

In figure 5.6 the distribution of the number of matched stations per pattern is shown. The black line shows the number of stations crossed per simulated track. The shaded area shows the number of matched stations found on the patterns. The reconstructed pattern distribution follows the simulation closely, including events with a large number of stations. The pattern efficiency is 99.6%. This is similar to the efficiency obtained from the $Z^0 \rightarrow \mu\mu$ sample.

Figure 5.7 shows the number of matched stations in the segment collection per simulated track. Note the large tail due to muons with a large incident angle. The overall

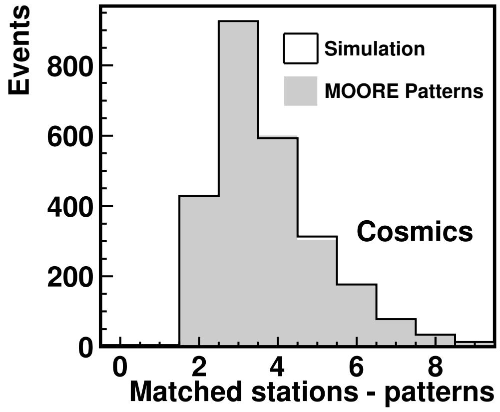

Figure 5.6: *Total number of matched stations in patterns per simulated muon for cosmic muon events.*

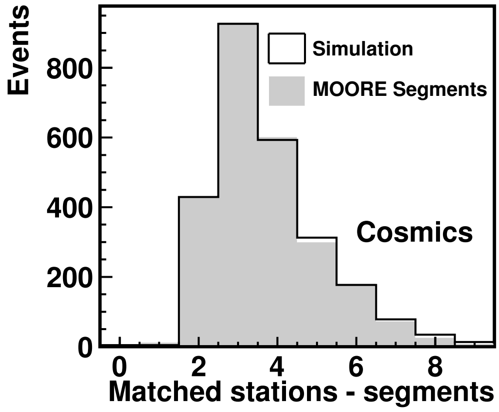

Figure 5.7: *Total number of matched stations in segments per simulated muon for cosmic muon events.*

efficiency is 98.8%.

5.2.2 Tracking performance

In this section, the properties of the reconstructed tracks will be studied, like the track parameters, the number of hits and segments, and the efficiency.

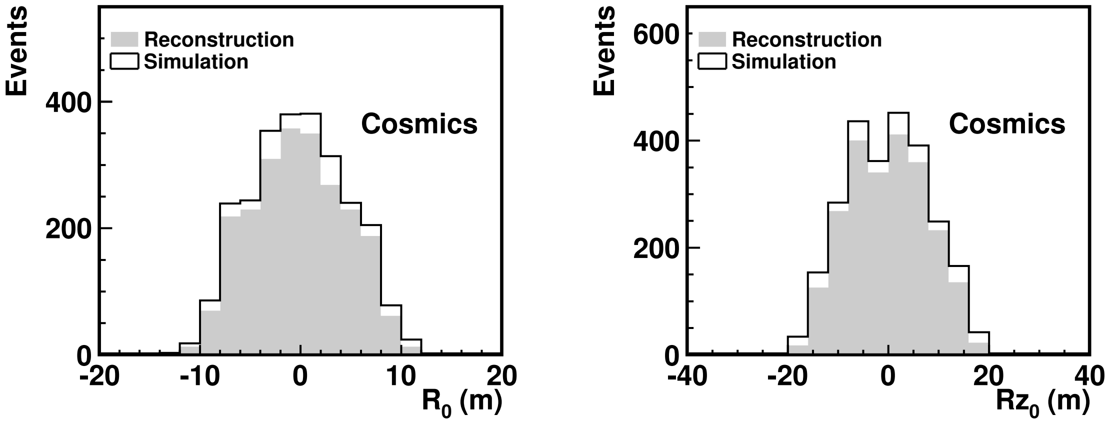

Figure 5.8: *Impact parameters of simulated and matched tracks. R_0 and Rz_0 are defined as the distance of the closest point on the track to the IP in the xy-frame and Rz-frame, respectively. The parameters of the simulation are shown in both cases.*

Figure 5.8 shows the impact parameters of the simulated muons. As expected, muons close to the IP are reconstructed with a higher efficiency, while farther away the efficiency is reduced. This can be seen more clearly in figure 5.9, where the efficiency has been plotted versus the track parameters R_0 and Rz_0. R_0 and Rz_0 are defined as the distance

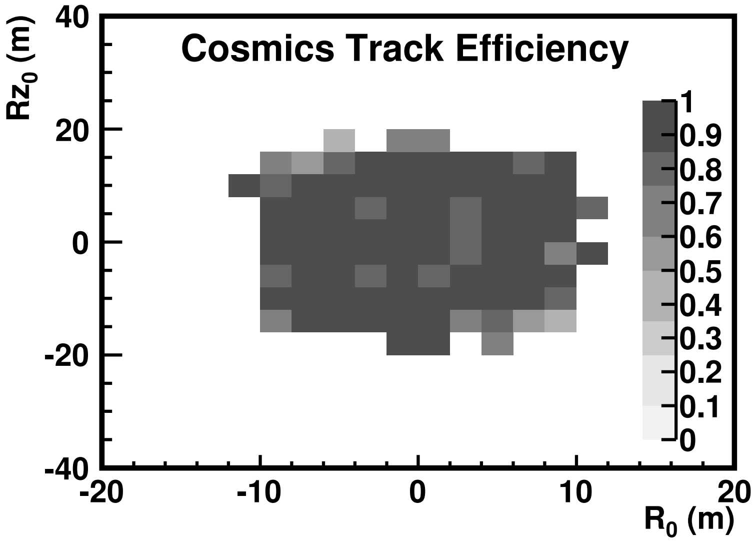

Figure 5.9: *Track efficiency versus the impact parameters R_0 and Rz_0.*

of the closest point on the track to the IP in the xy-frame and Rz-frame, respectively. For impact parameters smaller than about eight meters, the track efficiency is high. Outside of the barrel region the efficiency drops steeply.

To further study the tracking efficiency and improve the understanding of the track reconstruction, the simulated muons are divided into three samples:

I. **Inner layer barrel tracks:** Simulated muons with either three hits in all three MDT barrel layers, or at least five hits in the MDT inner barrel layer and five hits in one of the other MDT barrel layers;

II. **Outer barrel tracks:** Simulated muons with no hits in the MDT inner barrel layer and at least five hits in the middle and outer barrel layer;

III. **Endcap tracks:** Simulated muons with at least five hits in two of the three endcap layers.

Note that the categories are not mutually exclusive nor do they cover all reconstructed tracks. The choice for the categories is motivated by the different studies that can be performed on these samples.

For each category the distribution of the number of matched MDT segments and ϕ trigger layers per reconstructed track are shown in figure 5.10. The segment and track efficiency is summarised in table 5.1.

It is expected that the track reconstruction is most efficient for the first category, as these muons have a small incident angle with respect to the MDT stations and come closest to the IP, for which the detectors and tracking have been optimised. Furthermore, the muons usually cross three stations, which allows for some inefficiency in the segment efficiency, since the track fit requires two or more segments. These tracks can be used to

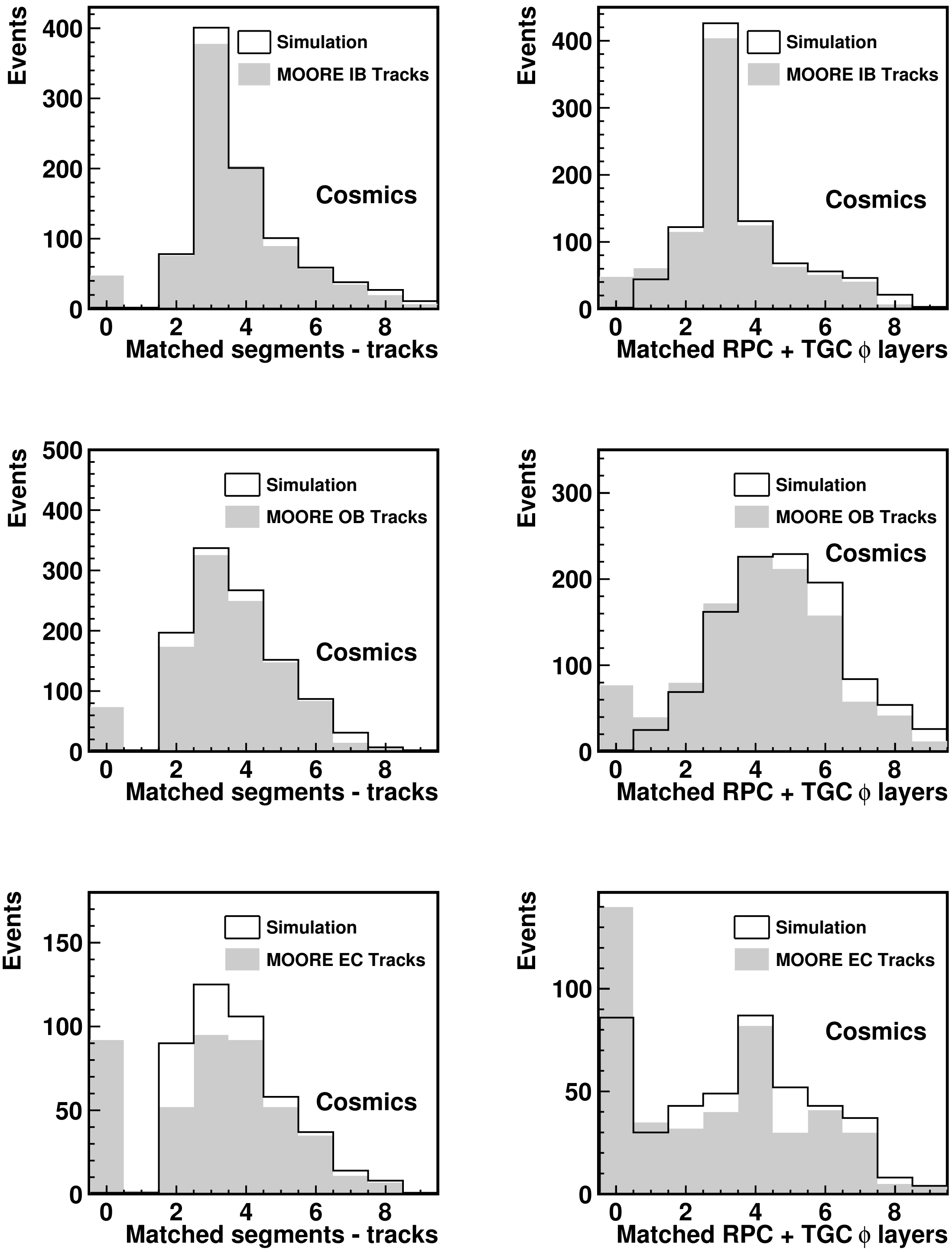

Figure 5.10: *Number of MDT segments (left plots) and RPC + TGC ϕ layers (right) assigned to reconstructed tracks for cosmic muon events crossing the inner barrel (upper), outer barrel (middle) and endcap (lower) respectively.*

	Inner Barrel (I)	Outer Barrel (II)	Endcap (III)
Segments	99.1%	98.3%	99.2%
Tracks	95%	93%	79%

Table 5.1: *MOORE segment and track efficiency for each track category.*

study the barrel alignment and combined reconstruction with the inner detector. Since most of these tracks have been split and are pointing to the IP, they resemble tracks from proton-proton collisions. Therefore, the reconstruction software for collision data can be studied on these events as well.

The second category consists of outer barrel tracks, hitting at least the middle and outer MDT layers, without hitting the inner layer. Together with the first category, these tracks can be used to study timing between different trigger towers. Using tracks that cross the endcap inner layer, the alignment between the barrel and endcap can be studied. These tracks are in general not split and the traversed number of stations per track is larger than in category I. The segment efficiency on this category is slightly lower with respect to the other two, because of the large incident angles that can be present.

The endcap tracks, category three, are expected to be rare and mostly consist of muons that have scattered in the ATLAS detector or the last meters of rock. Most of these muons will have low momentum. These tracks are useful for aligning the endcap detectors and study the TGC trigger. The tracks are often complete endcap tracks, traversing two or three MDT endcap chambers and all four TGC layers. Since the ϕ TGC coverage is slightly smaller than the MDT coverage, the number of ϕ layers is 0 in about 15% of the events. For this reason, in addition to the large percentage of tracks in the overlap region and the aforementioned less precise initial pattern parameters, the tracking efficiency is lower than in the other two categories.

5.2.3 Comparison with Muonboy

The performance of the MOORE reconstruction on cosmic muons is compared with the performance of the Muonboy programme [58], [80] at the segment and the tracking level. To be able to make a proper comparison, the main differences of the cosmic muon reconstruction of Muonboy with respect to MOORE will be briefly described.

Like MOORE, the Muonboy programme is a software package in ATHENA that provides a standalone muon reconstruction. The core is written in Fortran 90 and can in principle be run standalone. A C++ interface allows interaction with the ATHENA environment. Muonboy has two modules, one for the segment reconstruction and one for the track reconstruction.

Although the overall reconstruction strategy is similar to MOORE, there are a few notable differences. Contrary to MOORE that uses a global pattern search (see chapter 3), Muonboy uses a local pattern and segment search in all MDT chambers. Muonboy uses no dedicated cosmic muon algorithm, but instead loosens its IP constraints when

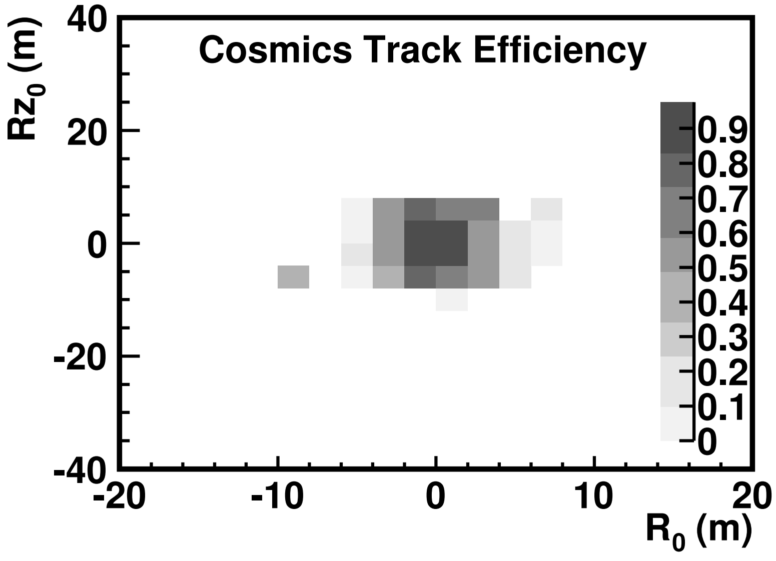

Figure 5.11: *Muonboy track efficiency versus the impact parameters R_0 and Rz_0.*

reconstructing cosmic muons. Furthermore, Muonboy does not aim to reconstruct cosmic muons that do not pass the calorimeter and additionally Muonboy splits the tracks at the closest point to the IP. Therefore, it is expected that the algorithm is only efficient for small R_0 and Rz_0, which can be observed in figure 5.11.

Outer barrel and endcap tracks (category II and III) will hardly be present in the Muonboy track container, which is confirmed in table 5.2. The segment performance on these categories however is still reasonably good. Muonboy has a cut on the segment θ angle and the normal of the MDT chamber, which lowers its efficiency for the very non-pointing segments in category II and III.

	Inner Barrel (I)	Outer Barrel (II)	Endcap (III)
Segments	98.6%	96%	87%
Tracks	68%	8%	6%

Table 5.2: *Muonboy segment and track efficiency for each track category.*

A comparison is only performed on category I. The Muonboy segment efficiency for this category is 98.6% (compared to 99.1% for MOORE), and the track efficiency is 70% (compared to 92% for MOORE). The regular performance plots for this category are shown for segments and tracks in the figures 5.12 and 5.13. As the same simulated events are analysed, these plots can be directly compared with the top plots of figure 5.10. Note that MOORE reconstructs a larger number of tracks and associates on average more MDT segments and ϕ layers to the tracks.

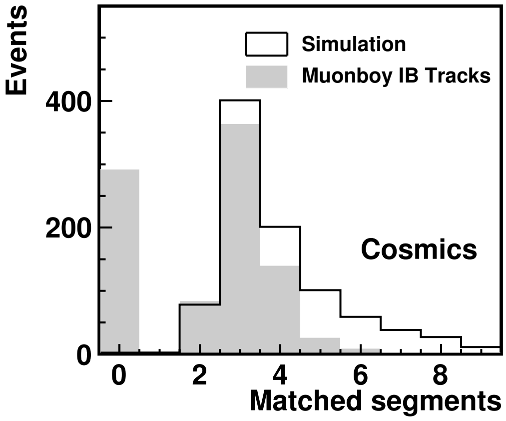

Figure 5.12: *Number of MDT segments assigned to tracks for cosmic muon events crossing the inner barrel.*

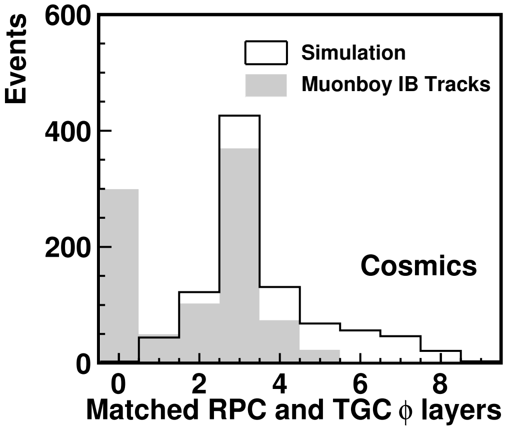

Figure 5.13: *RPC + TGC ϕ layers assigned to tracks for inner barrel cosmic muon events.*

5.3 Conclusions

This chapter has described the ATLAS simulation with a particular emphasis on the simulation of cosmic rays in the ATLAS detector. The peculiarities of the cosmic ray muons and in particular the difficulties in reconstructing them have been described. Several adaptations to the reconstruction algorithms have been made to successfully reconstruct these cosmic muons.

A performance study on simulated cosmic muon data is done which shows that all parts of the reconstruction are in good shape. Especially the pattern and segment performance is excellent with an efficiency of 99.6% and 98.8% respectively.

The MOORE performance on three different track categories, inner barrel, outer barrel and endcap tracks, have been studied. The tracking efficiencies for the three categories are 95%, 93% and 79% respectively. A comparison with a different muon reconstruction algorithm, Muonboy, has been done and it is shown that this algorithm reconstructs the inner barrel tracks with an efficiency of 70%. Compared to Muonboy, MOORE associates on average more MDT segments and ϕ measurements to the inner barrel tracks. Muonboy is not designed to reconstruct tracks for the other two categories and has significant lower performance for them.

Chapter 6

Cosmic muon reconstruction: using data from the ATLAS detector

In the previous chapter the simulation of cosmic muons has been described and the performance of the reconstruction has been discussed. This knowledge can now be used to study and commission the muon spectrometer as installed in the ATLAS cavern with real cosmic ray muon data.

When analysing data several complications arise compared to simulated data. First, not all chambers are connected to the readout system, since e.g. they are not installed or not yet operational. Furthermore, earlier commissioning tests have shown that several chambers have imperfections, such as electronics problems, gas leaks, noisy or dead channels. Also the precise positions of the individual chambers and detector elements in the ATLAS cavern are not known. All these factors need to be accounted for. To achieve an optimal resolution, each detector element has to be calibrated, the individual detectors need to be aligned and readout (trigger) times have to be synchronised.

In this chapter one particular commissioning run is chosen and its properties will be studied. The data quality and the calibration for the events in this run will be discussed, and then a performance study of the standalone tracking will be performed.

6.1 Data sets

Starting from the winter of 2005, cosmic muon data has been taken during several periods. Figure 6.1 shows one of the first cosmic muon events recorded with the ATLAS muon spectrometer, displayed with the Atlantis event display [81]. Only a few MDT chambers were read out and triggered by a scintillator [82]. In this particular event two MDT segments have been reconstructed, which are shown in the figure. No RPC chambers were read out.

The setup has been extended gradually to include all detectors of the muon spectrometer. During 2007 and 2008, data was taken during several so-called *milestone* and *production* runs, with the aim to obtain high-quality cosmic muon data and to test new features of the setup, trigger and reconstruction. In August 2008 all detectors of ATLAS

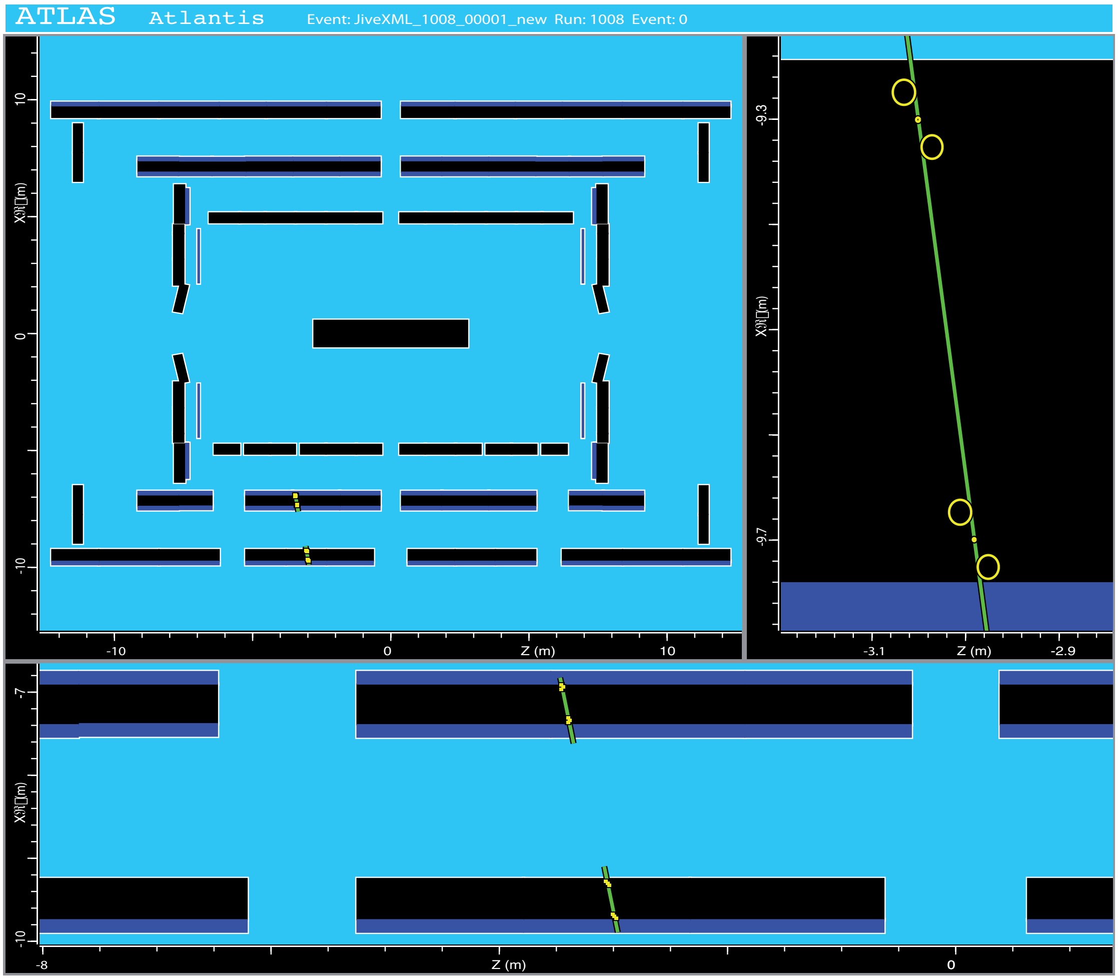

Figure 6.1: *Event display of one of the first cosmic muon events recorded in ATLAS (December 2005). Rz-view of the ATLAS muon spectrometer, three zoom levels. Two MDT segments and their driftcircles can be seen.*

were integrated into the final DAQ system. Since then cosmic muon data has been taken with hundreds of millions recorded events [83].

Milestone period 6 (M6), which was held during the first week of March 2008, has been chosen for study. During the M6 period the following detectors were (partly) readout: SCT, TRT, tile and liquid argon calorimeters, MDT, RPC, and TGC. Three detectors were used for triggering: the tile calorimeter, the RPCs, and a scintillator trigger. The scintillator trigger was a dedicated trigger for the inner detector and consisted of two scintillators placed above the MDTs of sector 5. Moreover, the MDT chambers of the complete barrel sectors 3-8 (about 40% of all barrel MDT chambers), the inner endcap wheel of side C, and the RPC chambers of sector 7 and 8 have been read out. A schematic overview of the setup is shown in figure 6.2.

Run 43719 was one of the longest runs in M6 and was the first long run with tracks in the SCT and TRT. With a trigger rate of around 100 Hz, run 43719 contains nearly two

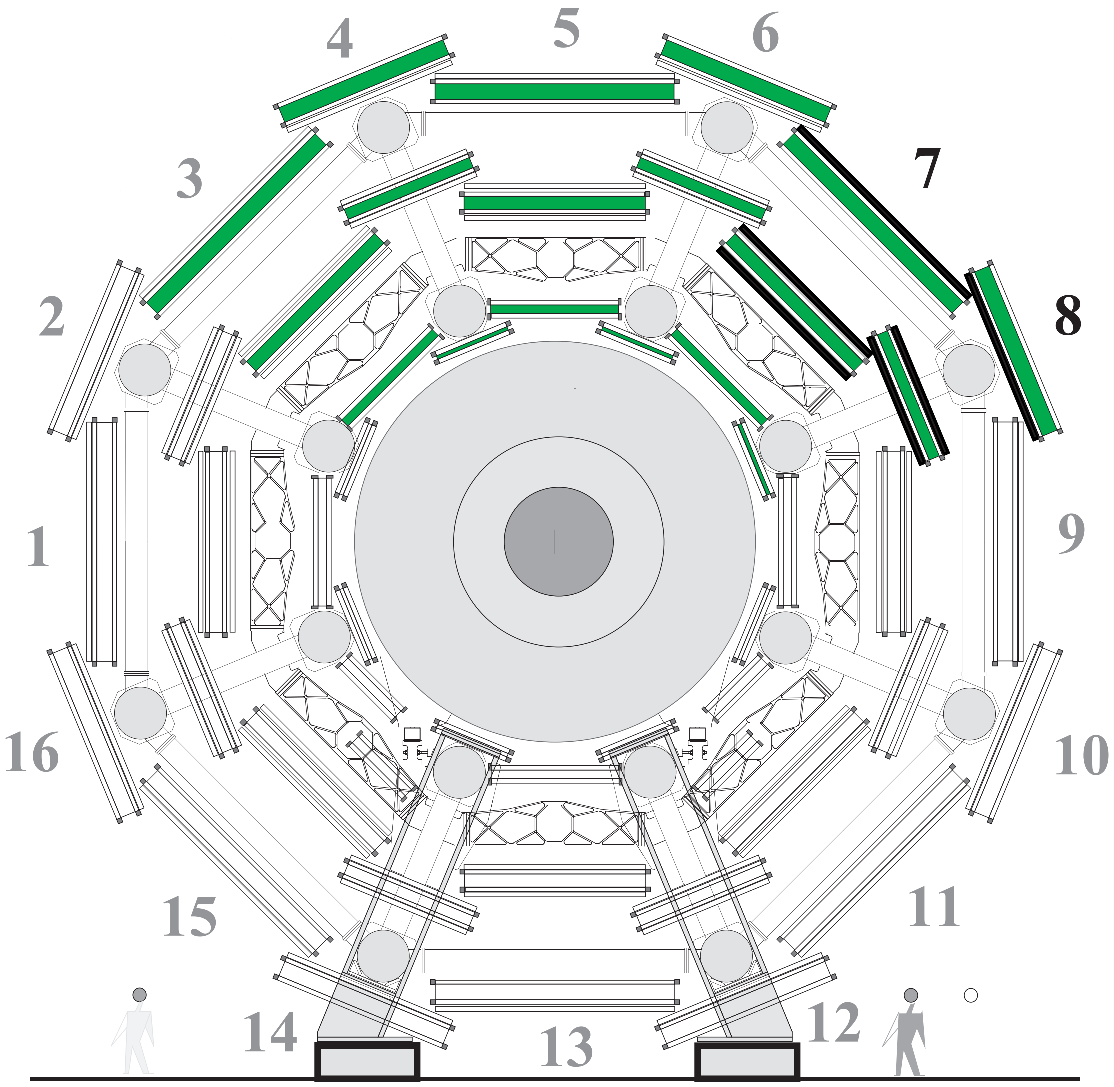

Figure 6.2: *Schematic overview of the M6 setup in the xy-frame. The read out MDT (sectors 3-8) and RPC chambers (sectors 7 and 8) are indicated (green and black). The MDT inner endcap wheel of side C is not shown.*

million events recorded in six hours [84]. About 136,000 events from the RPC trigger stream have been analysed to produce the results in the following sections.

6.2 Reconstruction for data

The reconstruction for data is performed in the same way as for the cosmic muon simulation as described in the previous chapter. However there are a few notable differences in the data sample with respect to the simulated sample that should be taken into account, when comparing the samples:

- **One hemisphere:** Since only one hemisphere is read out, the cosmic muon tracks will not be split and only one track per muon is reconstructed;
- **Additional timing uncertainties:** Additional timing uncertainties are present in the data with respect to the simulation. The dominant timing uncertainty comes from the trigger: the time window of the RPC trigger of 25 ns (LHC clock), and the desynchronisation between the different trigger towers. There are several other factors, e.g. misalignment, wrong initial calibrations and no time of flight correction that worsen the resolution of cosmic muon data compared to simulated or proton-proton collision data. To account for all these factors, the errors of the MDT hits are initially enlarged to 2 mm to prevent to miss hits and segments;
- **Trigger acceptance:** Only events that are accepted by the trigger are recorded. For the RPC stream, the trigger is provided by the middle RPC layer. This has a large impact on the event type, which are considerably more pointing to the IP compared to simulation. Due to the low number of trigger towers that are read out (only sector 7 and 8), the direction of the cosmic muons is constrained;

Recently, cosmic muon MDT segment reconstruction has been performed using a so-called t_0*-fit* [85–88]. This method leaves the time as a free parameter in the segment fit. However, this method has not been deployed here, since not all systematics have been understood yet, and the amount of fake segments and segments from non-triggered, out-of-time muons are increased.

6.3 MDT calibration

To achieve optimal results, the detectors, and in particular the MDT chambers, need to be calibrated. As was explained in section 2.3.2, the MDT drift radius is obtained in two steps: first the drift time, t_{drift}, is calculated from the measured TDC time t_{TDC}:

$$t_{drift} = t_{TDC} - t_{tof} - t_{prop} - t_0 \tag{6.1}$$

where t_{tof} is the time of flight of the muon from the known absolute trigger time to the tube. For collision events this is just the distance of the tube to the IP divided by the velocity of the particle, the speed of light; as mentioned earlier this quantity is not corrected for in the reconstruction; t_{prop} is the propagation delay along the tube, i.e. the time the signal pulse propagates through the wire to the readout; and t_0 is a constant, that contains all additional cable and electronics delays. From the drift time, the drift radius is calculated using the rt-relation. For this calculation both t_0 and the rt-relation need to be calibrated.

6.3.1 Hit spectra

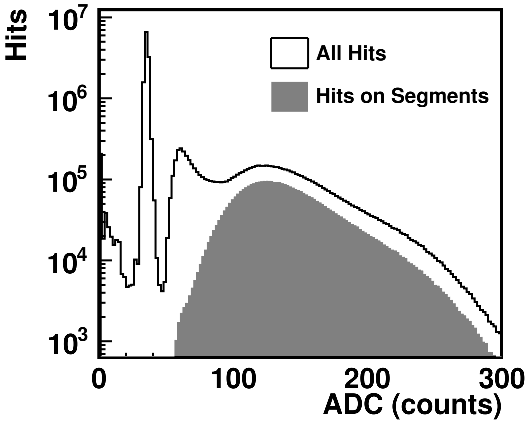

Figure 6.3: *Wilkinson ADC spectrum of all raw hits and hits on segments (dark area). The Wilkinson ADC value provides the measurement of the leading edge charge deposited on the MDT wire.*

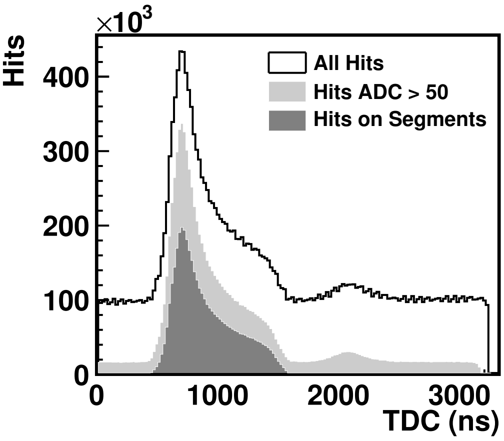

Figure 6.4: *TDC spectrum of raw hits (black line), after removal of hits with a Wilkinson ADC value smaller than 50 (shaded area) and of hits on segments (dark area).*

Figure 6.3 shows the raw hit Wilkinson ADC count value of all hits, it provides the measurement of the leading edge charge deposited on the MDT wire. The large peak at 40 ADC counts consists of noise hits and these hits are ignored in the reconstruction in which a cut on 50 ADC counts is applied. The broader peak are the hits caused by traversing particles. In the TDC spectrum, figure 6.4, the noise can be observed as a flat distribution in addition to the drift time spectrum of the physical hits. The cut on the ADC value strongly reduces the noise contribution. For calibrating the MDT chambers, only hits from reconstructed segments are considered. Their ADC and TDC value is also shown in the figures (dark area).

6.3.2 MDT resolution

The MDT calibration software [28], [89], [90] determines the t_0 and t_{max} values by fitting the TDC spectrum. In principle each tube is calibrated individually, however when the number of events per tube is insufficient for calibration, e.g. in regions with a lower trigger acceptance, tubes are grouped together. The rt-relation is obtained by iteratively refitting the reconstructed segments using the already determined t_0 and minimising the residuals [30], [91]. The MDT calibration is done on dedicated computer farms, the so-called *Tier2* centers [92].

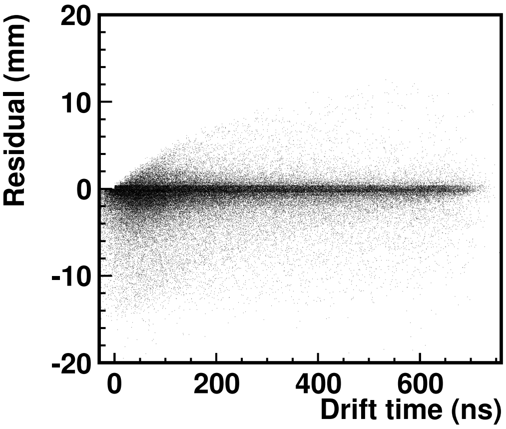

Figure 6.5: *Residuals as a function of the drift time for all hits on a segment.*

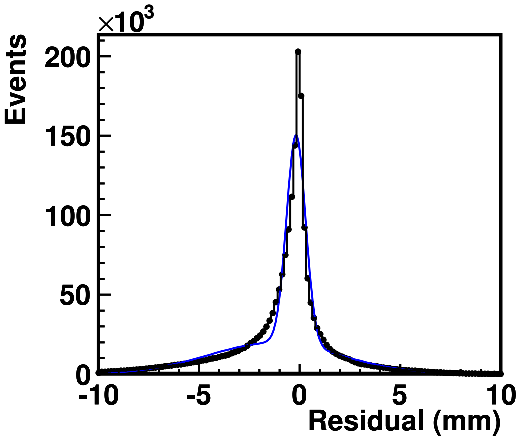

Figure 6.6: *Distribution of the segment hit residuals leaving out the hit concerned from the segment fit. A double Gaussian fit to the distribution is drawn. A sigma of 0.5 mm in the residual is obtained.*

In figure 6.5 the residual of the hits on a segment is shown as a function of the radius after calibration. The residual of a hit is calculated by leaving out the hit from the segment fit. The rt-relation describes the data reasonably well, except for the hits close to the wire. By fitting the distribution with two Gauss distributions, a sigma of 0.5 mm in the residual is obtained. The fit is shown in figure 6.6.

The dominant contribution to the time resolution is the uncertainty on the RPC trigger time, which is shown in figure 6.7. The uncertainty is mainly caused by the desynchronisation between the different trigger towers with a smaller contribution from the RPC trigger time window, which is set to 25 ns. Since for LHC collisions the trigger time will be synchronised with the (precise) LHC clock, these uncertainties will not be present in collision data.

6.4 Performance

Although the nominal MDT tube resolution is not achieved (as explained in section 6.3.2), it is expected that the efficiency of the segment finding is not affected. Due to the rather loose resolution of 2 mm, additional fake segments will be reconstructed:

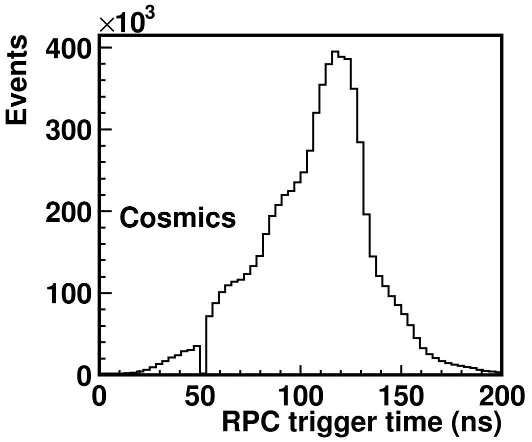

Figure 6.7: *RPC trigger time in ns. The uncertainty is mainly caused by the desynchronisation between the different trigger towers with a smaller contribution from the RPC trigger time window, which is set to 25 ns. These uncertainties will not be present in collision data.*

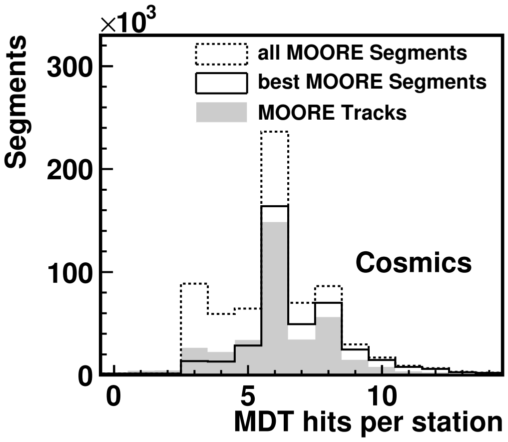

Figure 6.8: *Number of MDT hits on segments per station. The solid line shows all segments; the dashed line shows the number of MDT hits for the best segment per station (with most hits). The shaded area shows the number of MDT hits per station for segments associated to tracks.*

e.g. more segments are made out of a pattern. This can be seen in figure 6.8, where the number of hits per segment is shown. As can be seen a considerable number of segments with three and four hits are present (dashed line). To reduce the number of fake segments, the distribution of the number of hits per best segment (with most number of hits) on a station is shown as well (solid line). Also shown, by the shaded area, are the number of hits per station for segments associated to a track. The shape of the distribution is similar to the one for the $Z^0 \rightarrow \mu\mu$ sample, figure 4.11, which indicates that the data and the segment reconstruction are in good shape.

6.4.1 Multilayer efficiency

If a segment has only hits in one of the multilayers, this might point to a problem in either the detector or the reconstruction, e.g. dead channels, broken electronics or wrong timing. Figure 6.9 shows found (left plots) and missed (right plots) MDT multilayers, when there is a hit on a track in the other corresponding multilayer. As there is no geometric check, muons that only traverse one multilayer of a station are counted as missed in the other multilayer. To be certain that a cosmic muon has traversed, only segments associated to tracks are considered. The integer numbering in ϕ and η follows the ATLAS ϕ and η conventions [93], $\phi = 1 \ldots 16$ and $\eta = \pm 1 \ldots 6$. In the plots η is shifted by 0.5 for the outer multilayer.

These plots give, independent of the logbooks, a quick overview of which chambers

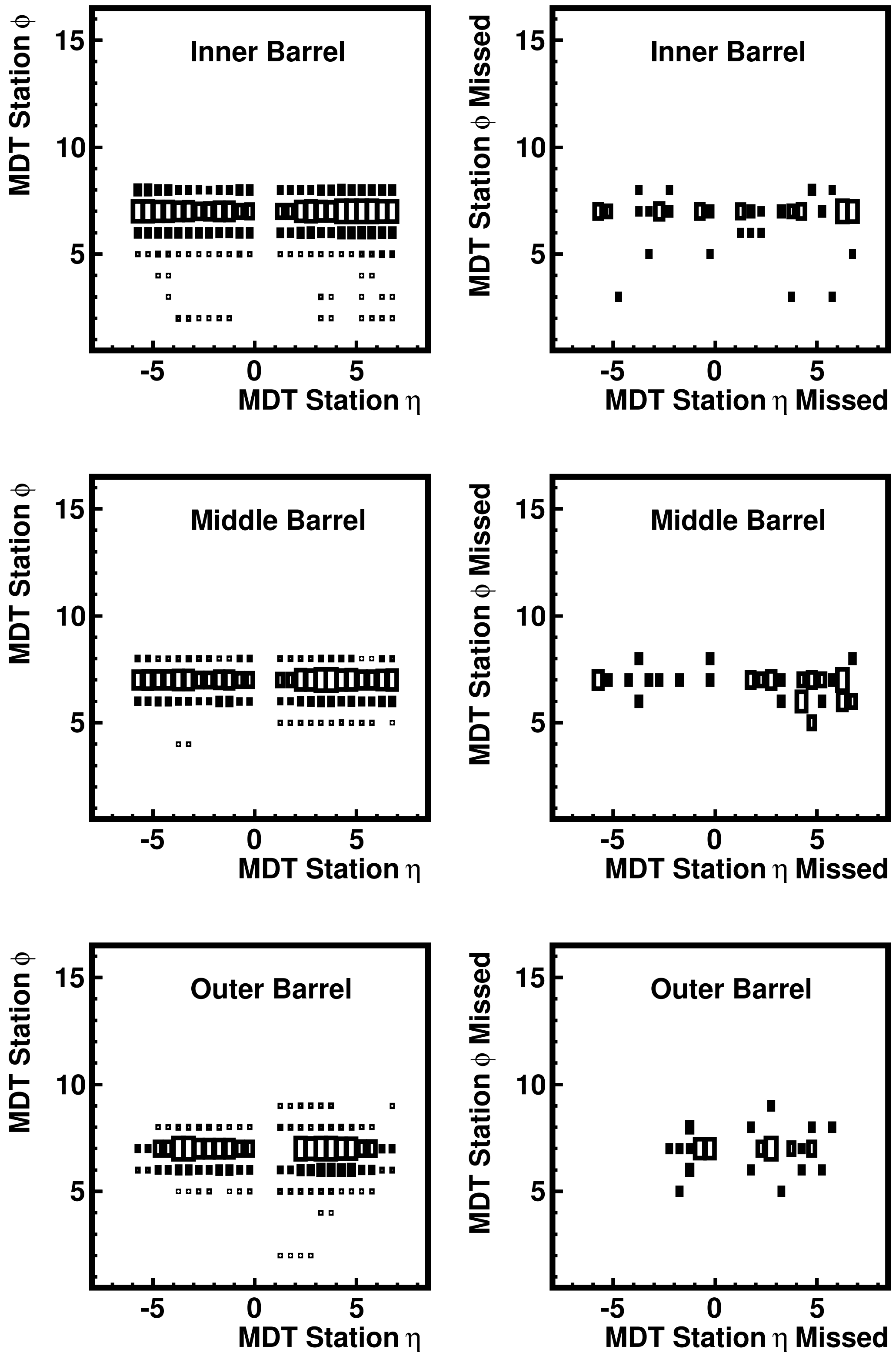

Figure 6.9: *Segments counted per multilayer (left plot) and missed segments (right) per multilayer for inner (upper), middle (middle) and outer (lower) barrel chambers. The ATLAS numbering scheme is followed. Block sizes are on a relative scale. For a more detailed explanation, see the text.*

have problems. Cabling and decoding problems in the reconstruction can be spotted as well. For example, it turns out that BOL7A01, the outer barrel chamber in ϕ-sector 7, at $\eta = +1$ was not read out, as can be seen by the empty bins in the lower left plot of figure 6.9.

By dividing the number of missed segments by the number of segments, a biased multilayer efficiency can be calculated for each multilayer. It is biased since a segment in the other multilayer is required. The efficiency is 98.5% for the outer, 98.3% for the middle and 98.0% for the inner barrel chambers.

6.4.2 Tracking performance

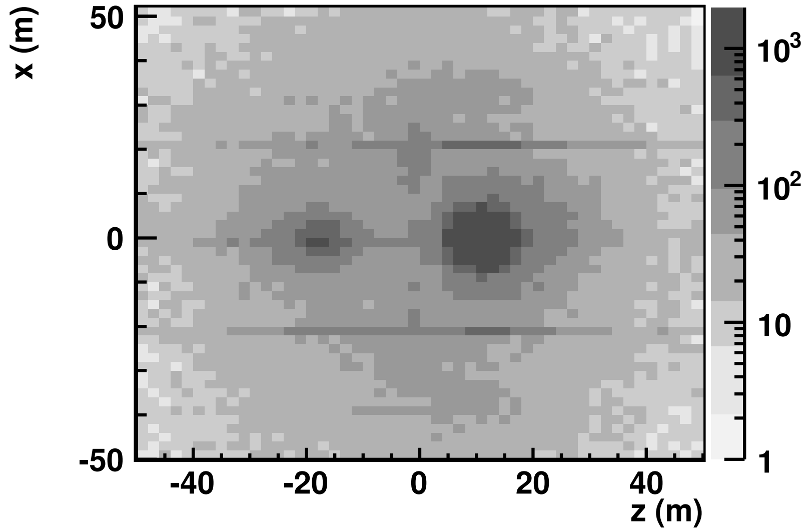

Figure 6.10: *Position of the tracks at $y = 64$ m, halfway between the ATLAS cavern and the ground floor. The two entrance shafts at $x = 1.7$ m, $z = -16.5$ m (small) and $z = 13.5$ m (large) can be recognised. The elevators shafts at $x = \pm 20$ m, $z = 0$ m can also be seen. The lines at $x = \pm 20$ m are caused by tracks without ϕ information.*

As has been explained in chapter 5, the cosmic muons will mostly come from the two entrance shafts above the ATLAS cavern. This can be shown on the data by extrapolating the reconstructed tracks from the cavern to the ground floor. In figure 6.10, the extrapolated position of the reconstructed muon track is shown at $y = 64$ m, halfway between the cavern and the ground level. Both the small and the large shaft at respectively $z = -16.5$ m and $z = 13.5$ m have an increased track density.

In the figures 6.11 and 6.12 the number of MDT segments and RPC ϕ layers per track are shown. On 136,000 events, about 125,000 tracks have been reconstructed. The distributions show that most reconstructed tracks traverse the middle and outer layer. Note that for events with no ϕ hits, tracks can be reconstructed.

Contrary to what was done on simulation, it is obviously not feasible to quantify directly the tracking efficiency when analysing data. And although the simulated cosmic

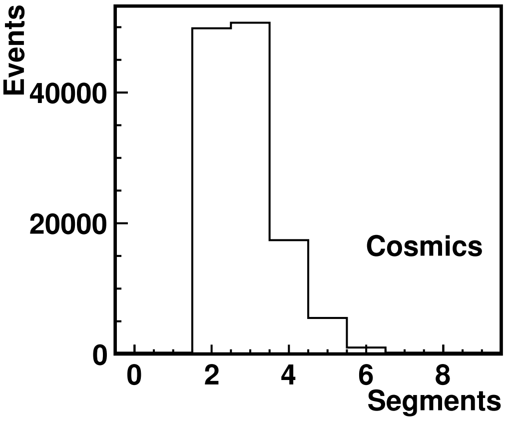

Figure 6.11: *Number of MDT segments assigned to tracks for cosmic muon events.*

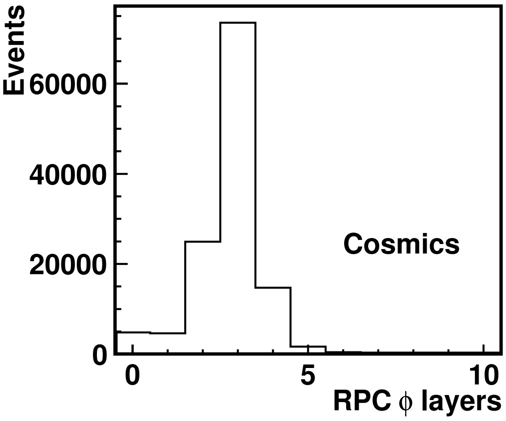

Figure 6.12: *Number of RPC ϕ layers assigned to tracks for cosmic muon events, gas-gaps have been merged.*

muon sample has been extremely useful for understanding the details of cosmic muon track reconstruction, it is not trivial to use the simulation to calculate the tracking performance. Each of the differences between simulation and data mentioned in section 6.2 introduces a bias in the data sample, which should be accounted for. For example, due to the absence of a simulation of the trigger the distribution of the cosmic ray muons is different.

Although all of these differences may in principle be overcome, it is chosen to study the tracking performance using data itself. The segment reconstruction has been proven to be robust and highly efficient both on data and in chapter 5 on simulation. Therefore, based on the reconstructed segments, it is possible to effectively select events for which a track is expected to be found.

As was shown in figure 6.8, there is a substantial number of reconstructed segments with few hits. To reduce the number of selected events without a cosmic muon and as a minimal requirement for the track reconstruction, it is chosen to select events that have a segment with at least two hits in each multilayer in at least two out of the three barrel layers (inner, middle, outer). Such a segment is called a *good segment.* Furthermore, to reduce the number of cosmic shower events, the events with more than 30 segments and more than one reconstructed track (about 5%) are removed from the sample. About 119,000 events have been selected.

For these events, figure 6.13 shows the number of layers that have a good segment and the number of layers that have a good segment associated to a track (shaded area). Note that there are some tracks that have segments in four layers, which accounts for events that also have an endcap segment. The fraction of the selected events with a reconstructed track is 90%. In figure 6.14 the number of ϕ layers are shown for segments and tracks. The distribution of the tracks follows the segment distribution. For the Muonboy reconstruction programme this fraction is 69%. As was discussed previously, the main difference between the two programmes, is that Muonboy is less

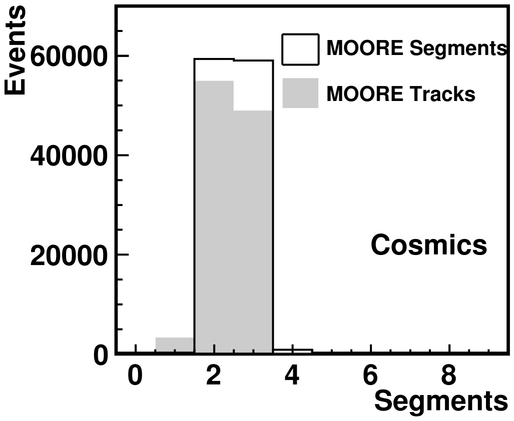

Figure 6.13: *Number of muon spectrometer layers with a good segment. A minimum of two good barrel segments are required.*

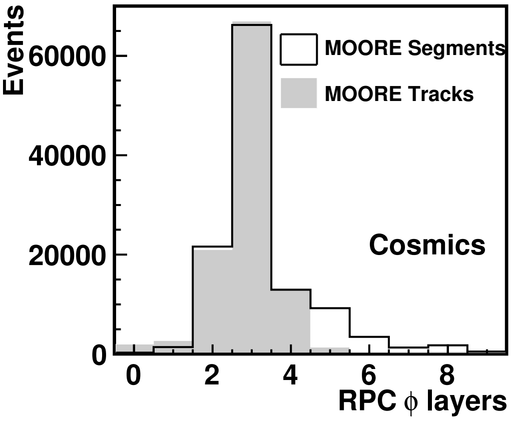

Figure 6.14: *Number of RPC ϕ layers assigned to tracks for cosmic muon events, gas-gaps have been merged. A minimum of two good barrel segments are required.*

efficient for muons with large impact parameters.

It should be noted that for the simulation the same efficiency is 99%. This seemingly large discrepancy with the data can be explained to a large extent by the reduced number of chambers present in the readout and an higher number of non-correlated segments. Applying the additional cut that in the event at least two segments are pointing to each other in the Rz-frame within 75 mm, reduces the number of events by 10%, while the efficiency rises to 95%.

6.4.3 Combined tracking

The milestone runs are a combined effort of all the ATLAS detector groups, which means that calorimeter and inner detector information is recorded in every event as well. Run 43719 was one of the first runs which has reconstructed inner detector tracks on a large scale by reading out TRT detectors and nearly the complete SCT barrel [94]. The inner detector tracking information can be used to determine the muon spectrometer performance as well. When an inner detector track is present in the event, it can be expected that a muon spectrometer track crossed the upper part of the spectrometer. Note that one has to be careful probing the lower part of the muon spectrometer by inner detector tracks, since a fraction of the muons are stopped in the calorimeter. Since in M6 only upper muon spectrometer chambers have been read out, this does not have to be taken into account.

For the event selection, in addition to the above-mentioned segment selection, an inner detector track is required. This category of cosmic muons will be pointing to the IP. Therefore, it is expected that the track reconstruction for this category is as efficient as the track reconstruction in proton-proton collision events.

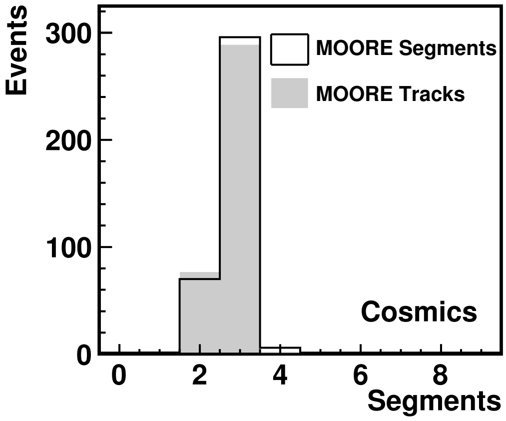

Figure 6.15: *Number of MDT segments assigned to tracks for cosmic muon events with an inner detector track.*

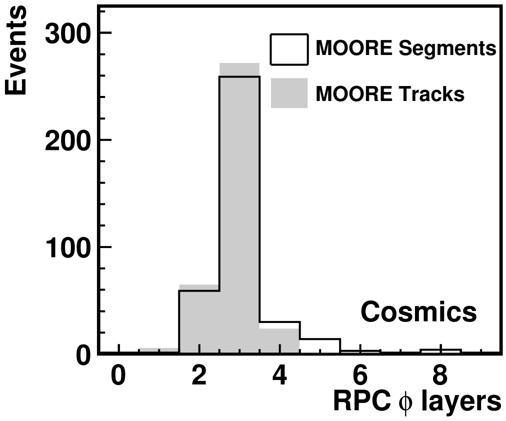

Figure 6.16: *Number of RPC ϕ layers assigned to tracks for cosmic muon events with an inner detector track; gas-gaps have been merged.*

Due to the low acceptance of the inner detector with respect to the muon spectrometer, most of the recorded events with the RPC trigger will not have any inner detector information. About 400 events have been selected. The figures 6.15 and 6.16 show again the number of MDT segments and RPC ϕ layers. Since the tracks are more pointing to the IP, the number of MDT segments and RPC ϕ layers have a more distinct peak at three compared to figures 6.13 and 6.14.

The impact parameters of the tracks are shown for both samples in the figures 6.17 and 6.18. Note that the distribution of R_0 is smaller for data than on simulation due to the RPC trigger acceptance. Requiring an inner detector track, the efficiency for the muon tracks is 99%. Muonboy has a similar track efficiency.

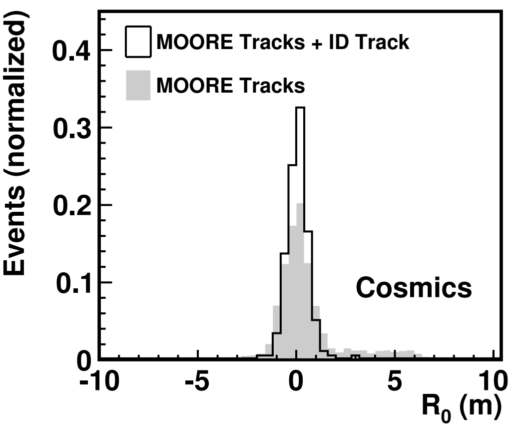

Figure 6.17: *Impact parameter R_0 in the xy-frame per track.*

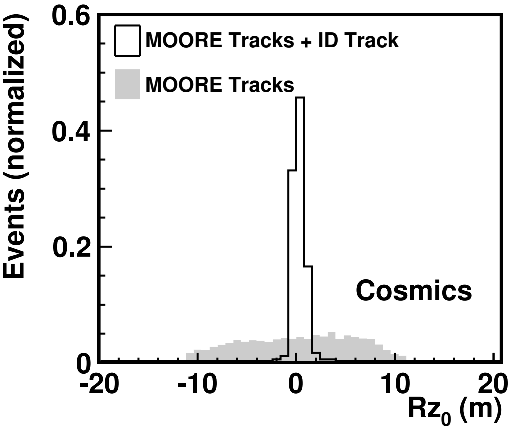

Figure 6.18: *Impact parameter Rz_0 in the Rz-frame per track.*

6.5 Conclusions

In ATLAS several hundreds of million cosmic muon events have been recorded since the end of 2005. In September 2008 all of its detectors were operational and data has been recorded almost continuously since. All of these events have been reconstructed using the dedicated cosmic muon reconstruction algorithms that have been described in the chapters 3 and 4. This chapter has shown a study on one of the cosmic muon data runs. The setup of the M6 data set has been described and the MDT calibration procedure was explained. On this particular run without specific data cuts or t_0-fit, a sigma of 0.5 mm in the MDT hit residual is obtained. This is higher than the nominal MDT tube resolution of 80 μm due to suboptimal calibrations with as main contribution the RPC trigger time uncertainty. By enlarging the MDT hit errors to 2 mm in the segment and track reconstruction, the trigger time uncertainty and the misalignment have been accounted for.

The MDT detector performance and segment reconstruction has been shown to be robust and efficient by calculating the multilayer segment efficiency. By putting cuts on the number of MDT segments, a biased tracking efficiency can be calculated. When asking for 2 good segments in an event, the tracking efficiency of MOORE is shown to be 90%. For Muonboy this efficiency is 69%. Requiring an inner detector track, the tracking efficiency of MOORE and Muonboy is determined to be 99%.

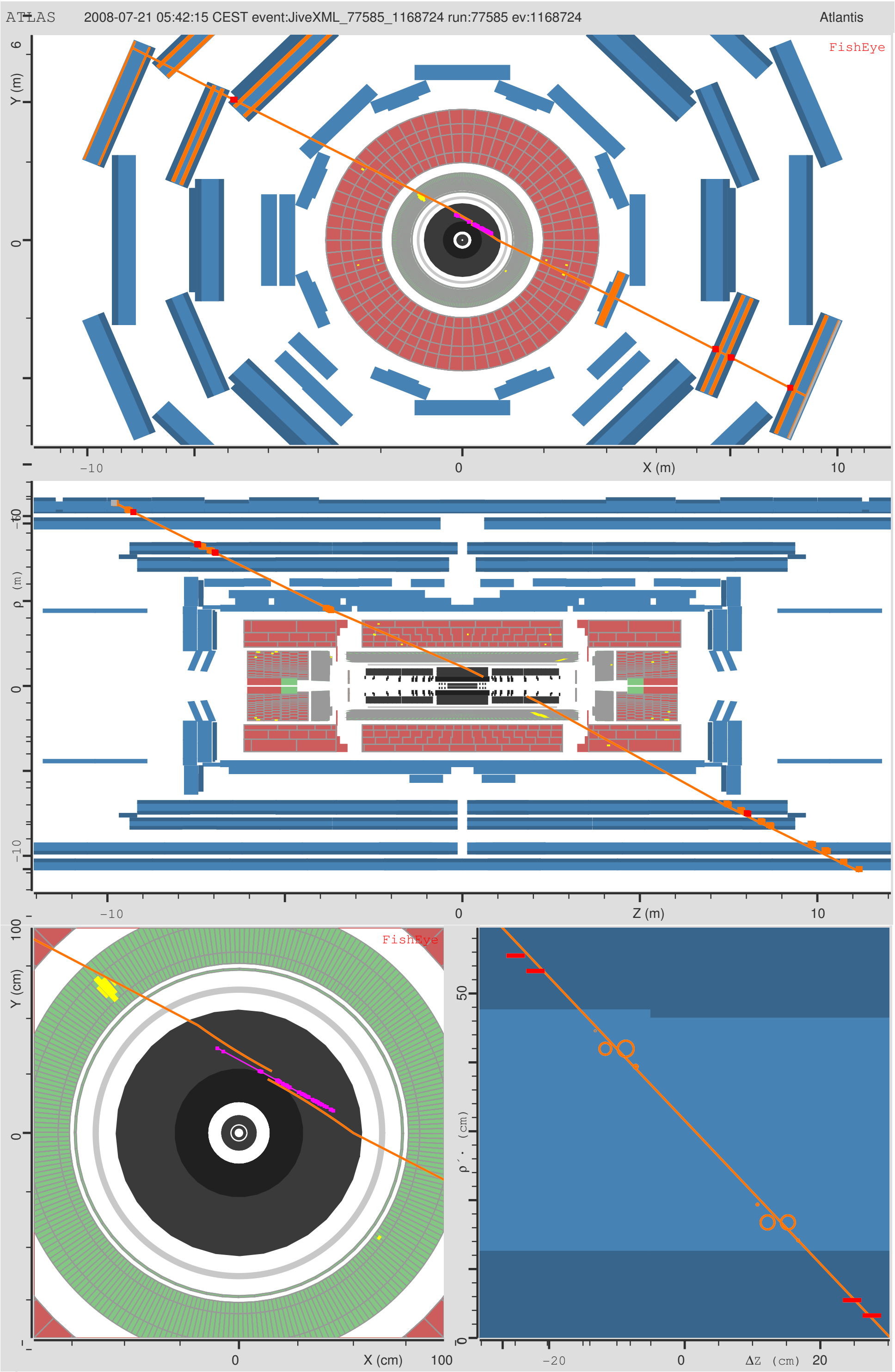

Figure 6.19: *Event display of M8 cosmic muon event taken in July 2008 [95]. Upper and middle: xy-view and Rz-view of the whole ATLAS detector, calorimeter, RPC and MDT hits are seen. Lower left: zoom in to inner detector, TRT and SCT hits are shown. Lower right: zoom in to one of the MDT stations, RPC η hits and MDT driftcircles are seen.*

Summary

The Standard Model is a well established theory for elementary particle physics that describes all known elementary particles and their interactions. Except for gravity all known forces are included: the electromagnetic, weak and strong nuclear force.

ATLAS is one of the two general-purpose experiments at the LHC accelerator at CERN, which is a proton-proton collider with an unprecedented nominal center-of-mass energy of 14 TeV. One of its main goals is to study the Standard Model and look for possible new physics beyond this model. Especially searched for, will be the Higgs particle, the last not-measured particle predicted by the Standard Model. Extensions to the Standard Model will be tested, e.g. supersymmetry and theories with extra dimensions. In many of the searches muons with a high transverse momentum will be crucial due to their clean signature in the detector.

In this thesis the performance of the muon spectrometer of ATLAS has been studied. Four detector technologies are deployed; the Resistive Plate Chambers (RPC) and the Thin Gap Chambers (TGC) provide the trigger in respectively the barrel and the endcap regions; the precision measurements to measure the momentum are performed by three layers of the Monitored Drift Tube (MDT) chambers and for the inner forward regions by the Cathode Strip Chambers (CSC). An eight-fold toroidal superconducting magnet system provides a magnetic field of typically 0.5 T. With these detectors the muon spectrometer will provide a momentum dependent muon trigger and measure the muon momenta with a resolution between 4% for 10 GeV $< p_T <$ 500 GeV and better than 10% for transverse momenta up to 1 TeV.

For each muon traversing the muon spectrometer these detectors will produce a number of position measurements. From this set of measurements, the trajectory can be reconstructed. The reconstruction is performed in several steps, first an initial pattern recognition is performed, after which the measurements in the individual chambers are locally fitted into so-called segments. From these segments track candidates are built, which are then fitted.

For the initial pattern recognition, an algorithm consisting of a family of global pattern searches based on the Hough transform has been developed. All detector technologies provide a precise measurement for two dimensions (xy or Rz), while the position in the other dimension is less precise. Therefore, the algorithm performs a search in each of the two precision planes, xy and Rz. The resulting two-dimensional patterns are then combined into a three-dimensional pattern. For the Rz-hits a transform is used that accounts for the curvature of the tracks.

The algorithm applies several techniques to distinguish patterns in the high background environment of ATLAS. The algorithm assigns a weight to each measurement, depending on the likelihood of it being a noise hit. Depending on the occupancy, special weighting is applied to reduce the cpu usage. It is shown that the algorithm has an excellent efficiency over a wide range of momenta and a low cpu usage in high background.

The pattern recognition algorithm is part of the highly modular and recently revised MOORE reconstruction program, which is, besides Muonboy, one of the two muon standalone reconstruction programs in ATLAS. The whole chain of MOORE modules, including the segment reconstruction, segment combining and tracking has been described in detail. Its performance is demonstrated on simulated dimuon decays of Z^0-bosons and J/ψ mesons. The performance metrics include efficiency, fake rates and momentum resolution. The total track efficiency and momentum resolution are well understood and competitive to the Muonboy programme. Misidentified track rates have been discussed and are shown to be under control.

For the commissioning of the ATLAS detectors, cosmic muons are deployed. To utilise the possibilities of these muons completely, the tracking needs to be changed and optimised. In particular the initial pattern recognition needs to be altered to account for non-pointing tracks. For this, dedicated Hough transforms have been developed. Furthermore, several adaptations have been made to the MOORE reconstruction programme to achieve a similar efficiency as the collision muons. On simulated cosmic muon samples it has been shown that the reconstruction is well understood for different categories of events. For each of these categories, it has been shown that MOORE has a better performance than Muonboy, especially for muons with large impact parameters with respect to the interaction point.

Cosmic muons have been recorded in the cavern since 2005 and the setup has been gradually extended. In 2008 all ATLAS detectors were present in the readout. For the muon spectrometer, differences between simulated and real cosmic ray muon data have been explained, with a focus on the reconstruction strategy. It has been shown that the MDT detector performance and MOORE segment and tracking reconstruction are robust and efficient for real cosmic muon data. Furthermore, it is shown that MOORE is currently the best reconstruction programme for cosmic muon data.

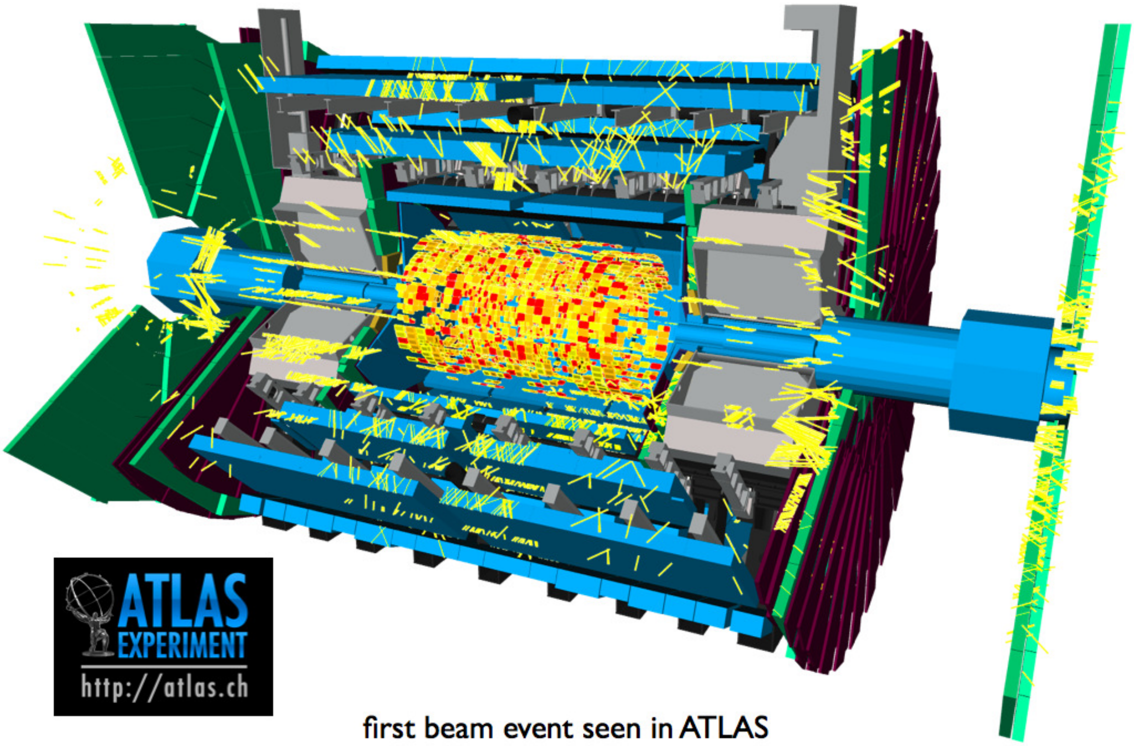

Figure 6.20: *Event display of the first single beam event recorded in ATLAS (September 2008).*

References

[1] L. Lin Y. Shen, J. Kuti, *Upper bound on the Higgs boson mass in the standard model*, Physics Review Letters **61** (1988) 678.

[2] The LEP Collaborations, *Search for the Standard Model Higgs boson at LEP*, Physics Letters **B565** (2003) 61.

[3] Tevatron The LEP and SLD Collaborations, *Precision Electroweak Measurements and Constraints on the Standard Model*, arXiv:hep-ex/08114682v1, 2008.

[4] M. Carena and H.E. Haber, *Higgs Boson Theory and Phenomenology*, Prog. in Part. Nucl. Phys. **50** (2003) 63.

[5] LHC Study Group, *The Large Hadron Collider: Conceptual Design*, CERN-AC-95-5, 1995.

[6] Vol. I LEP Design Report, *The LEP injector chain*, CERN-LEP/TH/83-29, 1983.

[7] ATLAS Collaboration, *ATLAS Technical Proposal for a General-Purpose pp Experiment at the Large Hadron Collider at CERN*, CERN/LHCC/94-43, 1994.

[8] CMS Collaboration, *CMS The Compact Muon Solenoid Technical Proposal*, CERN/LHCC/94-38, 1994.

[9] ALICE Collaboration, *ALICE Technical Proposal for A Large Ion Collider Experiment at the LHC*, CERN/LHCC/95-71, 1995.

[10] LHCb Collaboration, *LHCb Technical Proposal A Large Hadron Collider Beauty Experiment for Precision Measurements of CP Violation and rare Decays*, CERN/LHCC/98-4, 1998.

[11] TOTEM Collaboration, *TOTEM Technical Design Report*, CERN/LHCC/2004-002, 2004.

[12] LHCF Collaboration, *Technical Design Report of the LHCf experiment*, CERN/LHCC/2006-004, 2006.

[13] G. Arnison et al., *Experimental observation of isolated large transverse energy electrons with associated missing energy at* $\sqrt{s} = 540\ GeV$, Physics Letters **B122** (1983) 103.

[14] G. Banner et al., *Observation of single isolated electrons of high transverse momentum in events with missing transverse energy at the CERN anti-p p collider*, Physics Letters **B122** (1983) 476.

[15] http://public.web.cern.ch/press/PressReleases/Releases2009/PR13.09E.html.

[16] G.Aad et al. ATLAS Collaboration, *The ATLAS experiment at the CERN Large Hadron Collider*, 2008.

[17] ATLAS Inner Detector Community, *ATLAS Inner Detector Technical Design Report*, CERN/LHCC/97-16 &17, 1997.

[18] ATLAS Collaboration, *ATLAS Calorimeter Performance Technical Design Report*, CERN/LHCC/96-40, 1997.

[19] ATLAS LARG Unit, *ATLAS Liquid Argon Calorimeter Technical Design Report*, CERN/LHCC/96-41, 1996.

[20] M. Aharrouche et al., *Energy Linearity and Resolution of the ATLAS Electromagnetic Barrel Calorimeter in an Electron Test-Beam*, Nucl. Instrum. Methods Phys. Res. **A568** (2006) 601.

[21] M. Hurwitz, *Module-to-module uniformity at 180 GeV in 2002-2003 tile calorimeter calibration test-beams*, ATL-PUB-TILE-2006-008, 2006.

[22] C. Adorisio et al., *System Test of the ATLAS Muon Spectrometer in the H8 Beam at the CERN SPS*, ATL-MUON-PUB-2007-005, 2007.

[23] C. Adorisio et al., *Study of the ATLAS MDT Spectrometer using High Energy CERN combined Test beam Data*, ATL-MUON-PUB-2008-005, 2008.

[24] ATLAS Collaboration, *ATLAS forward detectors for measurement of elastic scattering and luminosity*, CERN-LHCC-2008-004, http://cdsweb.cern.ch/record/1095847, 2008.

[25] ATLAS Collaboration, *Zero degree calorimeters for ATLAS*, CERN-LHCC-2007-01, http://cdsweb.cern.ch/record/1009649, 2007.

[26] ATLAS Collaboration, *ATLAS forward detectors for luminosity measurement and monitoring*, CERN-LHCC-2004-10, http://cdsweb.cern.ch/record/721908, 2004.

[27] ATLAS Muon Collaboration, *ATLAS Muon Spectrometer Technical Design Report*, CERN/LHCC/97-22, 1997.

[28] N. v. Eldik, *The ATLAS muon spectrometer: calibration and pattern recognition*, Ph.D. thesis, Nikhef, 2007.

[29] G. Avolio et al., *Test of the first BIL tracking chamber for the ATLAS muon spectrometer*, Nucl. Instrum. Methods Phys. Res. **A523** (2004) 309.

[30] M. J. Woudstra, *Precision of the ATLAS muon spectrometer*, Ph.D. thesis, Nikhef, 2002.

[31] H. van der Graaf et al., *RASNIK technical system description for ATLAS*, NIKHEF Note ETR-2000-04, http://cdsweb.cern.ch/record/1073160, 2000.

[32] J.C. Barriere et al., *The alignment system of the barrel part of the ATLAS muon spectrometer*, ATL-MUON-PUB-2008-007, http://cdsweb.cern.ch/record/1081769, 2008.

[33] I. Potrap, *Muon spectrometer alignment with cosmic muons*, ATLAS Week (2009) , http://indico.cern.ch/getFile.py/access?contribId=55&sessionId=12&resId=0&materialId=slides&confId=47254 .

[34] J. Illingworth and J.Kittler, *A survey of the hough transform*, Computer Vision, Graphics and Image Processing **44** (1988) 87.

[35] A.J. Storkey, N.C. Hambley, C.K.I. Williams, and R.G. Mann, *Cleaning sky survey data bases using Hough transform and renewal string approaches*, Monthly Notices of the Royal Astronomical Society **347** (2004) 36.

[36] P.V.C. Hough, *Machine Analysis of Bubble Chamber Pictures*, In *International Conference on High Energy Accelerators and Instrumentation, CERN*, 1959.

[37] P.V.C. Hough, *Methods and means to recognize complex patterns*, 1962, U.S. Patent No. 3069654.

[38] ATLAS Computing Group, *ATLAS Computing Technical Design Report*, 2005.

[39] G. Barrand et al., *GAUDI - A software achitecture and framework for building HEP data processing applications*, Comp. Phys. Comm. **140** (2001) 45.

[40] Robert S. Engelmore and Anthony Morgan, *Blackboard Systems*, Addison-Wesley Publishing Company, New York, 1988.

[41] P.F. Åkesson et al., *ATLAS Tracking Event Data Model*, ATLAS-COM-SOFT-2006-005, 2006.

[42] T. Cornelissen et al., *Updates of the ATLAS Tracking Event Data Model (Release 13)*, ATLAS-COM-SOFT-2007-008, 2007.

[43] http://atlas-computing.web.cern.ch/atlas-computing/links/nightlyDocDirectory/MuonPrepRawData/html/index.html.

[44] http://atlas-computing.web.cern.ch/atlas-computing/links/nightlyDocDirectory/TrkPrepRawData/html/index.html.

[45] http://atlas-computing.web.cern.ch/atlas-computing/links/nightlyDocDirectory/MuonPattern/html/index.html.

[46] http://atlas-computing.web.cern.ch/atlas-computing/links/nightlyDocDirectory/MuonPattern/html/classMuon_1_1MuonPatternChamberIntersect.html.

[47] http://atlas-computing.web.cern.ch/atlas-computing/links/nightlyDocDirectory/TrkMeasurementBase/html/index.html.

[48] http://atlas-computing.web.cern.ch/atlas-computing/links/nightlyDocDirectory/TrkRIO_OnTrack/html/index.html.

[49] http://atlas-computing.web.cern.ch/atlas-computing/links/nightlyDocDirectory/MuonSegment/html/index.html.

[50] http://atlas-computing.web.cern.ch/atlas-computing/links/nightlyDocDirectory/MuonSegment/html/classMuon_1_1MuonSegmentCombination.html.

[51] http://atlas-computing.web.cern.ch/atlas-computing/links/nightlyDocDirectory/TrkTrack/html/index.html.

[52] http://atlas-computing.web.cern.ch/atlas-computing/links/nightlyDocDirectory/TrkTrack/html/classTrk_1_1TrackStateOnSurface.html.

[53] http://atlas-computing.web.cern.ch/atlas-computing/links/nightlyDocDirectory/TrkParameters/html/index.html.

[54] D. Adams et al., *Track reconstruction in the ATLAS Muon Spectrometer with MOORE*, ATL-MUON-2003-012, 2003.

[55] https://twiki.cern.ch/twiki/bin/view/Atlas/CscReconstruction.

[56] W. Park, *CSC reconstruction*, In *US ATLAS Muon Software Meeting*, 2008, http://indico.cern.ch/getFile.py/access?contribId=17&resId=0&materialId=slides&confId=34946.

[57] D. Primor, *MDT Segment Maker in Athena - Status Report*, In *11th ATLAS Muon Week*, 2006.

[58] M. Virchaux, *Muonbox: a full 3D tracking programme for Muon reconstruction in the ATLAS Spectrometer*, ATL-MUON-1997-198, 1997.

[59] N. van Eldik, *private communication.*

[60] http://atlas-computing.web.cern.ch/atlas-computing/links/nightlyDocDirectory/MuonCurvedSegmentCombiner/html/index.html.

[61] http://atlas-computing.web.cern.ch/atlas-computing/links/nightlyDocDirectory/MuonSegmentCombinationCleaner/html/classMuon_1_1MuonSegmentCombinationCleaner.html.

[62] A. Salzburger et al., *Concepts, Design and Implementation of the ATLAS New Tracking (NEWT)*, ATL-SOFT-PUB-2007-007, 2007.

[63] T.G. Cornelissen, *Track Fitting in the ATLAS Experiment*, Ph.D. thesis, Nikhef, 2006.

[64] I. Gavrilenko, *Description of global pattern recognition program (xkalman)*, ATL-INDET-97-165, 1997.

[65] R. Clifft and A. Poppleton, *IPATREC: inner detector pattern-recognition and track-fitting*, ATL-SOFT-94-009, 1994.

[66] A. Salzburger, S. Todorova, and M. Wolter, *The ATLAS Tracking Geometry Description*, ATL-SOFT-PUB-2007-004, 2007.

[67] A. Salzburger, *The ATLAS Track Extrapolation Package*, ATL-SOFT-PUB-2007-005, 2007.

[68] ATLAS Collaboration, *Muon Combined Performance CSC Chapter*, ATL-COM-PHYS-2008-055, 2008.

[69] T. Sjöstrand, S. Mrenna, and P. Skands, *Pythia 6.4 Physics and Manual*, Journal of High Energy Physics **5** (2006) 26.

[70] S. Frixione and B.R. Webber, *Matching NLO QCD computations and parton shower simulations*, Journal of High Energy Physics **6** (2002) 29.

[71] S. Frixione and B.R. Webber, *Matching NLO QCD and parton showers in heavy flavour production*, Journal of High Energy Physics **8** (2003) 7.

[72] G. Corcella et al., *HERWIG 6.5*, Journal of High Energy Physics **01** (2001) 10.

[73] A. Vaniachine, *Data challenges in ATLAS computing*, Nucl. Instrum. Methods Phys. Res. **A502** (2003) 446.

[74] S. Agostinelli et al., *GEANT4 - A Simulation Toolkit*, Nucl. Instrum. Methods Phys. Res. **A506** (2003) 250.

[75] D. Costanzo et al., *ATLAS detector simulation : status and outlook*, ATL-SOFT-PUB-2005-004, 2005.

[76] C. Amsler et al., *The Review of Particle Physics*, Physics Letters **B667** (2008) 1.

[77] E. Solfaroli, *The ATLAS muon trigger detector in the barrel: performance simulation and cosmic ray tests*, Ph.D. thesis, Roma 'Tor Vergata', 2006.

[78] A. Aloisio et al., *The RPC Level-1 Muon Trigger of the ATLAS Experiment at the LHC*, ATL-COM-DAQ-2006-011, 2006.

[79] F. Anulli et al., *The Level-1 Trigger Barrel System of the ATLAS Experiment at CERN*, ATL-DAQ-PUB-2009-001, 2009.

[80] E. Lancon, https://twiki.cern.ch/twiki/bin/view/Atlas/TrackingOverviewRecoMuonboy.

[81] Z. Maxa et al., *Event Visualisation for the ATLAS Experiment - The Technologies Involved*, In *15th International Conference on Computing In High Energy and Nuclear Physics*, pages 167–169, 2006.

[82] F. Cerutti and L. Pontecorvo, *Cosmic ray runs acquired with ATLAS muon stations*, ATL-ENEWS-2006-010, 2006.

[83] https://twiki.cern.ch/twiki/bin/view/Atlas/InterestingRuns#Run_statistics.

[84] http://atlas-service-runinformation.web.cern.ch/atlas-service-runinformation.

[85] A. Belloni et al., *In-situ t_0 calibration for MDT segments*, ATL-COM-MUON-2009-006, 2009.

[86] J. Snuverink, *T0Fit on Sector 13 Cosmics*, In *ATLAS Muon Software Workshop*, 2006, http://indico.cern.ch/materialDisplay.py?contribId=s8t11&sessionId=s8&materialId=0&confId=a061124.

[87] P. Kluit, *MDT resolution and T0 fitter*, In *ATLAS Muon Week*, 2009, http://indico.cern.ch/contributionDisplay.py?contribId=16&confId=52347.

[88] A. Belloni et al., *Muon segments studies: calibration and resolution*, ATLAS-COM-MUON-2009-019, 2009.

[89] The ATLAS MDT calibration group, *A summary of the ATLAS MDT calibration model*, ATLAS-COM-MUON-2005-014, 2005.

[90] P. Bagnaia et al., *Calibration model for the MDT chambers of the ATLAS Muon Spectrometer*, ATLAS-COM-MUON-2008-006, 2008.

[91] M. Deile, *Optimization and Calibration of the drift-tube Chamber for the ATLAS Muon Spectrometer*, Ph.D. thesis, LMU, 2000.

[92] E. Pasqualucci et al., *Muon detector calibration in the ATLAS experiment : data extraction and distribution*, In *15th International Conference on Computing In High Energy and Nuclear Physics*, pages 134–137, 2006.

[93] K. Assamagan et al., *A Hierarchical Software Identifier Scheme for the ATLAS Muon Spectrometer*, ATL-MUON-2004-003, 2004.

[94] C. Magrath, *The Heart of ATLAS: Commissioning and Performance of the ATLAS Silicon Tracker*, Ph.D. thesis, Nikhef, 2009.

[95] https://twiki.cern.ch/twiki/bin/view/Atlas/ApprovedPlotsED.

Samenvatting

Het Standaardmodel is de gevestigde theorie voor de elementaire deeltjesfysica. Het beschrijft alle bekende elementaire deeltjes en hun interacties. Op de zwaartekracht na, worden alle bekende krachten beschreven: de elektromagnetische, de zwakke en de sterke kernkracht.

ATLAS is één van de zes experimenten die uitgevoerd worden aan de LHC versneller op CERN. De LHC is een proton-proton botser met een ongeëvenaarde nominale massamiddelpuntenergie van 14 TeV. Eén van de hoofddoelen van ATLAS is om het Standaardmodel te bestuderen en te zoeken naar mogelijke nieuwe fysica buiten dit model. In het bijzonder zal er gezocht worden naar het Higgs-deeltje, het laatste nog niet gemeten deeltje dat voorspeld wordt door het Standaardmodel. Extensies van het Standaardmodel, bijvoorbeeld supersymmetrie en theorieën met extra ruimtelijke dimensies, zullen in diverse studies worden getest. In veel van deze studies zijn muonen met een hoge transversale impuls cruciaal vanwege hun karakteristieke schone resultaat in de detector.

In dit proefschrift zijn de prestaties van de muonspectrometer van ATLAS bestudeerd. Daarbij zijn vier detectietechnieken toegepast; RPCs en TGCs leveren de trigger in respectievelijk het centrale en het voorwaartse deel, terwijl gemonitorde driftbuizen (MDT) en CSCs de precisiemetingen leveren voor het meten van de impuls. De achtvoudige supergeleidende toroïdemagneet levert het magnetisch veld met een typische sterkte van 0.5 T. Met deze detectoren levert de muonspectrometer een impulsafhankelijke muonentrigger en meet de impuls van de muonen met een 4% nauwkeurigheid voor transversale impulsen tussen de 10 en 500 GeV en beter dan 10% voor transversale impulsen tot 1 TeV.

Voor elk muon dat de muonspectrometer doorkruist, produceren de muondetectoren een aantal positiemetingen. Met deze metingen kan het spoor van het muon worden gereconstrueerd. De reconstructie wordt uitgevoerd in verschillende stappen. Als eerste wordt een patroonherkenningsalgoritme uitgevoerd. Vervolgens worden de metingen in de individuele detectiekamers lokaal gefit tot zogenoemde segmenten. Van deze segmenten worden spoorkandidaten gebouwd en vervolgens gefit.

Voor de initiële patroonherkenning is er een algoritme ontwikkeld bestaande uit een familie van globale zoekstrategieën die gebaseerd zijn op de Hough-transformatie. Alle detectortechnieken verstrekken een precieze meting in twee dimensies (xy of Rz), terwijl de posite in de derde dimensie minder precies is. Daarom zoekt het algoritme in elk van de twee precisievlakken, xy en Rz. De resulterende tweedimensionale patronen worden vervolgens gecombineerd in een driedimensionaal patroon. Voor het Rz-vlak is een transformatie gebruikt die rekening houdt met de kromming van de sporen.

Het algoritme past verschillende technieken toe om de patronen te kunnen onderscheiden in de hoge achtergrondomgeving van ATLAS. Het algoritme kent aan elke meting een gewicht toe, afhankelijk van de waarschijnlijkheid dat het een ruismeting is. Afhankelijk van de bezettingsgraad van de muonspectrometer wordt een speciale weging toegepast om het cpu-gebruik te verminderen. Het is aangetoond dat het algoritme een excellente efficiëntie heeft over een groot impulsbereik en een laag cpu-gebruik bij een hoge achtergrond.

Het patroonherkenningsalgoritme maakt deel uit van het modulaire en onlangs herziene MOORE reconstructieprogramma dat, naast Muonboy, één van de twee 'zelfstandige' muonreconstructieprogramma's van ATLAS is. De hele keten van MOORE modules, inclusief de segmentreconstructie, het combineren van segmenten en de spoorreconstructie is in detail beschreven. De prestaties van MOORE zijn aangetoond op gesimuleerde dubbele muonvervallen van Z^0-bosonen en J/ψ-mesonen. Er is gekeken naar efficiëntie, 'fake'-ratio en impulsnauwkeurigheid. De totale spoorefficiëntie en impulsnauwkeurigheid zijn goed begrepen en competitief vergeleken met het Muonboy programma. Foutief geïdentificeerde sporen zijn besproken en zijn beheersbaar.

Voor het installeren en testen van de ATLAS detectoren worden kosmische muonen gebruikt. Om de mogelijkheden van deze muonen geheel te benutten, moet de reconstructie worden aangepast en geoptimaliseerd. Vooral de initiële patroonherkenning moet worden veranderd om 'niet-wijzende' sporen te kunnen vinden. Hiervoor, zijn speciale Hough transformaties ontwikkeld. Tevens is het MOORE reconstructieprogramma op verschillende punten aangepast om een vergelijkbare efficiëntie te bereiken als voor muonen uit LHC-botsingen. Het is aangetoond dat de reconstructie van gesimuleerde kosmische muonen goed is begrepen voor verschillende categorieën sporen. Voor elk van deze categorieën is het aangetoond dat MOORE een betere prestatie levert dan Muonboy, vooral voor kosmische muonen met grote impactparameters ten opzichte van het interactiepunt.

Sinds 2005 zijn kosmische muonen geregistreerd in de ATLAS-detector en de setup is langzamerhand uitgebreid. In 2008 werden alle detectoren aangesloten op de readout. Voor de muonspectrometer zijn verschillen tussen simulatie en echte kosmische muonen uitgelegd, met een focus op de reconstructiestrategie. Het is aangetoond dat de MDT detectorprestaties en de MOORE segment- en spoorreconstructie robuust en efficiënt zijn voor echte kosmische data. Tevens is het aangetoond dat MOORE momenteel het beste reconstructieprogramma is voor kosmische muondata.